creative commons

COMMONS DEED

저작자표시-비영리-변경금지 2.0 대한민국

이용자는 아래의 조건을 따르는 경우에 한하여 자유롭게

- 이 저작물을 복제, 배포, 전송, 전시, 공연 및 방송할 수 있습니다.

다음과 같은 조건을 따라야 합니다:

저작자표시. 귀하는 원저작자를 표시하여야 합니다.

비영리. 귀하는 이 저작물을 영리 목적으로 이용할 수 없습니다.

변경금지. 귀하는 이 저작물을 개작, 변형 또는 가공할 수 없습니다.

- 귀하는, 이 저작물의 재이용이나 배포의 경우, 이 저작물에 적용된 이용허락조건을 명확하게 나타내어야 합니다.
- 저작권자로부터 별도의 허가를 받으면 이러한 조건들은 적용되지 않습니다.

저작권법에 따른 이용자의 권리는 위의 내용에 의하여 영향을 받지 않습니다.

이것은 이용허락규약(Legal Code)을 이해하기 쉽게 요약한 것입니다.

Disclaimer

dCollection

공학박사학위논문

유기냉매 랭킨사이클과 결합된 고분자 전해질막 연료전지 시스템의 성능에 관한 연구

Studies on the performance for a hybrid system composed of a polymer electrolyte membrane coupled with organic Rankine cycle

2016 년 8 월

서울대학교 대학원

기계항공공학부

김 동 규

Studies on the performance for a hybrid system composed of a polymer electrolyte membrane fuel cell coupled with organic Rankine cycle

A DISSERTATION SUBMITTED TO THE SCHOOL OF MECHANICAL AND AEROSPACE ENGINEERING OF SEOUL NATIONAL UNIVERSITY IN PARTIAL FULFILLMENT OF THE REQUIREMENTS FOR THE DEGREE OF DOCTOR OF PHILOSOPHY

By

Dong Kyu Kim

August 2016

Abstract

Studies on the performance for a hybrid system composed of a polymer electrolyte membrane fuel cell coupled with organic Rankine cycle

Dong Kyu Kim
School of Mechanical and Aerospace Engineering
The Graduate School
Seoul National University

In recent years, interest for polymer electrolyte membrane (PEM) fuel cells has grown for their relative low operating temperature, zero-emission, and higher system efficiency. However, irreversibility associated with the system can reduce its performance and efficiency. Therefore, there is still necessity for examining effects of operating parameters on the performance of fuel cell system.

In PEM fuel cell system, controlling operating pressure and temperature is significant factor for generating power. Considering operating characteristics of polymer electrolyte membrane for temperature, desirable operating

temperature is around 80°C. However, it is still debating for desirable operating pressure for PEM fuel cell system. Moreover, effect of pressure should be analyzed by considering effect of balance of plants consisting fuel cell system. That is why analysis of operating pressure is different among research groups. Some researchers insisted that higher operating pressure is promising due to its higher power generation from stack, easier water management and lower volume of stack. Others claimed that lower operating pressure can reduce power consumption from blower, and lower noise. Therefore, the effect of pressure on the system performance should be analyzed once more. Unfortunately, explanation for mass transport across the membrane according to pressure is insufficient. Previous studies have tried to explain mass transport through the membrane using diffusion, however, it hardly explain the effect of pressure on mass transport through the membrane. Therefore, we should elucidate the mechanism of waster transport through Nafion 117 which is used for membrane humidifier and stack. The first objective of this study is to examine the mechanism of mass transport through Nafion 117 and to analyze operating characteristics of fuel cell system.

Due to its lower operating temperature, most of researchers have tried to discharge waste heat from the fuel cell, and it consumes enormous power from thermal management system. Therefore, the system efficiency can be increased

by adapting technology of waste heat recovery; by recovering waste heat from PEM fuel cell, the system can generate more power, and the amount of power consumption from thermal management system can be decreased. Heat recovery can be achieved by combining organic Rankine cycle (ORC). Organic Rankine cycle is the same cycle compared with classic Rankine cycle except working fluid which is organic fluid. Although target of temperature of previous studies is around 200 ^{o}C, we tried to adapt ORC for low grade heat whose temperature of heat source is below 100 ^{o}C. The second objective of this study is to examine the performance of ORC system for low grade waste heat. We conducted parametric study to know the optimal operating condition. By examining the types of expander, power generation device for ORC, we tried to raise efficiency of ORC applied for low grade waste heat, as well. Lastly, we conduct system modeling for cogeneration system which is consisted of PEM fuel cell system coupled with ORC system to know the effect of pressure on the system performance. Through the system model, we examine the optimal operating condition for cogeneration system.

In this study, effect of pressure on cogeneration system which is consisted of PEM fuel cell system coupled with ORC system is examined to improve the system performance. Firstly, we conducted analysis to explain the effect of pressure on mass transport through Nafion 117. By considering water sorption

characteristics, we can explain the water transport mechanism through the membrane. Secondly, we analyzed operating characteristics of fuel cell system to examine the interaction between components consisting the system. Through the analysis, relationship between power consumption from auxiliaries and power generation from stack according to pressure is supported. Additionally, the feasibility of organic Rankine cycle for low grade waste heat is conducted. To increase system performance, we have applied several types of expander, such as rotary vane, rotary engine, and scroll type expander. Lastly, we conducted system model for combined heat and power system which is consisted of PEM fuel cell and ORC system to find optimal operating condition. By combining ORC with PEM fuel cell system, system performance is increased because it can generate power from waste heat and reduce the amount of waste heat and temperature of waste heat.

Keywords: Polymer electrolyte membrane fuel cell, organic Rankine cycle, hybrid system, Nafion 117, expander design

***Identification Number*: 2011-20687**

Contents

Abstract ..... **iii**

Contents ..... **vii**

List of Figures ..... **x**

List of Tables ..... **xiv**

Nomenclature ..... **xv**

Chapter 1. Introduction **19**

1.1 Background of the study **19**

1.2 Literature survey **24**

1.3 Objectives and scopes **30**

Chapter 2. Novel model for mass tranport through the Nafion® 117 ..... **33**

2.1 Introduction **33**

2.2 Numerical analysis for water transport mechanism across the Nafion ® 117 ..... **34**

2.3 Experimental set up **45**

2.4 Effect of relative humidity **50**

2.5 Effect of pressure **55**

2.6 Effect of mass flow rate **62**

2.7 Effect of temperature **68**

2.8 Summary 72

Chapter 3. Performance analysis for a 80 kW class fuel cell system 74

3.1 Introduction 74

3.2 Methodology 75

3.3 Parametric study for fuel cell car 107

3.3.1 Operating conditions depending on blower and BCV 107

3.3.2 System performance 112

3.4 Performance curve for PEMFC vehicle 121

3.5 Summary 125

Chapter 4. Performance analysis for organic Rankine cycle to recover low grade waste heat 127

4.1 Introduction 127

4.2 Methodology 127

4.3 Operating characteristics at a given tempearture range.....136

4.4 Effect of heat sink tempearture.....144

4.5 Performance map of organic Rankine cycle opeartion.....146

4.6 Summary 151

Chapter 5. Optimization for cogeneration system.....153

5.1 Introduction 153

5.2 Methodology 153

5.3 Effect of operating pressure on system performance **158**

5.4 Effect of current density on system performance **161**

5.5 Optimization for cogeneration system.....**167**

5.6 Summary **170**

Chapter 6. Concluding remarks.....**171**

References **174**

Abstract (in Korean) **181**

List of Figures

Figure 1.1 A clower lood at a renewable ydrogen society 19

Figure 1.2 Concept of cogeneration sysetm recovering waste heat..... 20

Figure 1.3 Schematic diagram of fuel cell system..... 25

Figure 1.4 T-s diagram of organic fluids compated to water..... 28

Figure 2.1 Schematic diagram of microstructure of Nafion® 117 and diffusion process of water molecules for different activities 35

Figure 2.2 Image of test chanber 48

Figure 2.3 Schematic diagram of the system..... 49

Figure 2.4 Comparison of relative humidity at the dry and wet side outlets for various inlet relative humidity..... 53

Figure 2.5 Mass flow rate of water molecules depending on several driving forces for various inlet relative hudmitt 55

Figure 2.6 Comparison of relative humidity at the dry and wet side outlets for various inlet pressure..... 59

Figure 2.7 Mass flow rate of water molecules depending on several driving forces for various inlet pressure 62

Figure 2.8 Comparison of relative humidity at the dry and wet side outlets for various inlet mass flow rates 66

Figure 2.9 Mass flow rate of water molevules depending on several driving forces for various inlet mass flow rates..... 68

Figure 2.10 Comparison of relative humidity at the dry and wet side outlets for various inelt temperature 72

Figure 2.11 Mass flow rate of water molecules depending on several driving forces for various inlet temperature 73
Figure 3.1 Schematic diagram of fuel cell vehicle 86
Figure 3.2 Flow chart for PEM fuel cell system..... 100
Figure 3.3 Flow chart for thermal management system 104
Figure 3.4 Voltage changes in steady state opeartion at different pressure 107
Figure 3.5 Changes in oxygen concentration near membrane determied by model..... 109
Figure 3.6 Changes in saturation factor at different pressure determined by model.....110
Figure 3.7 Validation for devices in each sub parts.....111
Figure 3.8 Mafor parameters which are affected at variable pressure system 113
Figure 3.9 The variation of stoichiometric number depending on load conditions.....115
Figure 3.10 The variation of relative humidity depending on load conditions 117
Figure 3.11 The variation of power generation from stack depending on load conditions..... 120
Figure 3.12 The variation of power consumption from auxiliries depending on load conditions 122
Figure 3.13 The variation of system power depending on load conditions 123

Figure 3.14 the variation of efficiency depending on load conditions 125
Figure 3.15 Performance curve of PEMFC vehicle at 60 km/h 128
Figure 3.16 Performance curve of PEMFC vehicle at 100 km/h 129
Figure 3.17 Performance curve of PEMFC vehicle at 140 km/h 130
Figure 4.1 Schematic diagram of organic Rankine cycle system..... 135
Figure 4.2 Scroll expander using for small-scale organic Rankine cycle system 139
Figure 4.3 Model validation 141
Figure 4.4 Changes of opeating conditions according to different evaporating pressure 144
Figure 4.5 Changes of system output according to different evaporating pressure 145
Figure 4.6 Chagnes of opearting conditions according to mass flow rate 147
Figure 4.7 Chagnes of system output aaccording to different mass flow rate 149
Figure 4.8 Operating characteristics of system according to tempearture at heat sink 151
Figure 4.9 T-s diagram of small-scale organic Rankine cycle system..... 154
Figure 4.10 Performance curve for small-scale organic Rankine cycle system 155
Figure 5.1 Schematic diagram of cogeneration system which is consisted of PEM fuel cell coupled with ORC system 162
Figure 5.2 Flow chart for the cogeneration system 163

Figure 5.3 Flow chart for genetic algorithm..... 165
Figure 5.4 Variation of power generation according to pressure..... 167
Figure 5.5 Variation of system efficiency according to pressure..... 168
Figure 5.6 Variation of power in the cogeneration system according to pressure 170
Figure 5.7 Variation of power geneartion according to current density ... 172
Figure 5.8 Variation of power generation according to current density ... 173
Figure 5.9 Variation of power in the cogeneration system according to current density..... 175
Figure 5.10 Optimal power generation of cogeneration system at different current density..... 178

List of Tables

Table 1.1: The list of heat source temperature of renewable energy..... 22

Table 1.2: Properties of organic fluids 27

Table 2.1: Parameter values employed in model for Nafion® 117 membrane 47

Table 2.2: Operating conditions for the effects of difference of relative humidity 52

Table 2.3: Operating conditiosn for the effects of difference of pressure .. 58

Table 2.4: Operating conditions for the effects of difference of mass flow rate 65

Table 2.5: Operating conditions for the effects of difference of inlet tempeature 71

Table 3.1: An example of features of some literature for blower models in the literatures 87

Table 3.2: An example of features of some literature for membrane humidifier models in the literatures 90

Table 3.3: An example of features of some literature for ejector models in the literatures 93

Table 3.4: An example of features of some literature for heat excanger models in the literatures 96

Table 3.5: An example of features of some literature for air providing system models in the literatures 101

Table 3.6: An example of features of some literature for fuel rercirculation

system models in the literatures 103

Table 4.1: Optimal opearting conditions of ORC according to increase of heat source tempeature..... 153

Table 5.1: Opeating condition for cogeneration system 166

Nomenclature

A	area [m^2]
a_w	water activity
c	concentration [mol m^{-3}]
d	diameter [m]
D	diffusivity [m^2 s^{-1}]
E	open circuit voltage [V]
EM	membrane dry equivalent weight [kg $kmol^{-1}$]
f	frequency [Hz]
ΔG	change of Gibbs energy [kJ mol^{-1}]
ΔH	Enthalpy change [kJ mol^{-1}]
i	current density [A cm^{-2}]
i_o	exchange current density [A cm^{-2}]
I	electrical current [A]
L	length [m]
n	number of participating electrons
n_{drag}	electroosmotic-drag coefficient [mol H_2O/mol H^+]
N	molar flux [mol s^{-1} m^{-2}]
P	pressure [bar]
R_{evap}	evaporation rate [mol s^{-1} m^{-3}]
R	universal gas constant [8.314 kJ $kmol^{-1}$ K^{-1}]
s	fraction of liquid water volume
t	time [s]
T	temperature [K]
u	velocity [m s^{-1}]
V	voltage potential [V]

W	molar flow rate [mol s^{-1}]

Greek symbols

ρ	density [kg m^{-3}]
ε	gas diffusion layer's porosity
λ	membrane water content [mol H_2O/mol SO_3^-]
ϕ	relative humidity [-]
δ	thickness [m]
σ	electronic conductivity [S m^{-1}]

Subscript

act	activation voltage loss
cl	catalyst later
ch	channel
conc	concentration voltage loss
fc	fuel cell
gdl	gas diffusion layer
in	into control volume
l	liquid
mea	membrane electrolyte assembly
ohmic	ohmic voltage loss
out	out of control volume
sat	saturation

v	vapor
w	both water vapor and liquid water

Chapter 1. Introduction

1.1 Background of the study

The most important issues for development of energy source are realization of hydrogen society and increase of power density. Emergence of hydrogen energy is originated from oil shortage and necessity for energy independence. Hydrogen is abundant element spread in all over the universe, and is environmentally friendly energy source. Moreover, hydrogen can produce more power than traditional energy source per pound. Closer look for hydrogen society is presented in Fig. 1.1 [1]. Through its benefits, there are some difficulties for using hydrogen as energy source. The process for manufacturing pure hydrogen is expensive and time consuming. Storage of hydrogen is another obstruction on the realization of hydrogen society. It means that we still have some issues to resolve to realize the hydrogen society.

Another big issue for problem of energy is to raise power density of system. System efficiency is connected with energy issue indirectly, because the efficiency determines the amount of energy usage. The efficiency of system can be increased by adapting the technology of waste heat which is shown as Fig. 1.2. The efficiency can affect the condition of waste heat; when some amount of waste heat is recovered, the amount of waste heat is reduced, and its temperature is also decreased. This change can affect positive aspect for environment. Waste heat recovery is achieved by applying Rankine cycle, and working fluid is water.

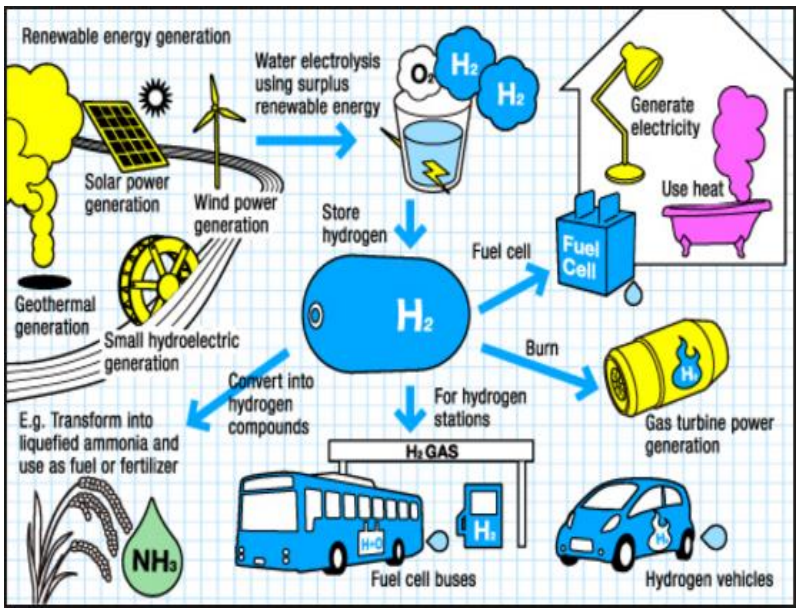

Fig. 1.1 A closer look at a renewable hydrogen society, 2010 [1]

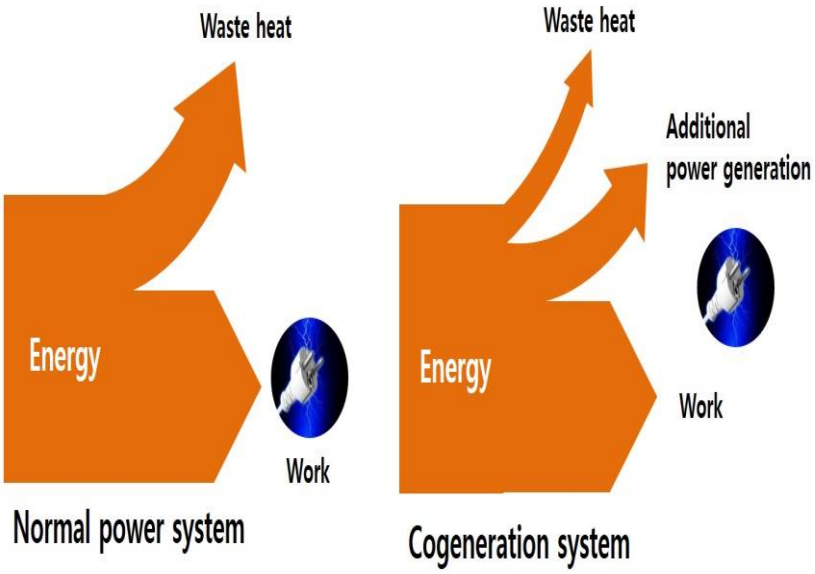

Fig. 1.2 Concept of cogeneration system recovering waste heat.

Until now, waste heat recovery has been applied to energy source which has higher temperature, such as power plant. General temperature of heat source is above 500 ^{o}C, however, it is better to decrease the temperature of heat source to raise system efficiency. These days, researchers have tried to recover low grade waste heat, the temperature is below 300 ^{o}C, to raise efficiency of alternative energy source. The temperatures of waste heat of alternative energy sources are presented in table 1.1 [2]. For recovering low grade heat, organic Rankine cycle is applied which has the same process with Rankine cycle, but it uses organic fluid as working fluid whose slope of curve of saturated liquid is positive. Thus, it can generate power at a lower temperature range. If the technology of ORC is applied to recover waste heat from the system using hydrogen as energy source, the realization of hydrogen society can be advanced.

To sum up, in this study, cogeneration system which is consisted of polymer electrolyte membrane fuel cell system coupled with organic Rankine cycle is investigated to raise system efficiency. By examining the operating characteristics of the fuel cell system which use hydrogen as energy source, this paper conducted parametric study for the system. We focused on the effect of pressure on the performance of the fuel cell system, especially, because operating strategy using pressure is different from each research groups. To elucidate the mechanism through the membrane, we tried to explain the mass transport of water by adapting water sorption characteristics of the membrane. Based on the understanding behavior of reactants according to the pressure, we showed interaction among devices consisting fuel cell system.

Table 1.1 The list of heat source temperature of renewable energy source [2].

Types of alternative energy	Heat source temperature (°C)
Biomass	250 ~ 350
Geothermal	90 ~ 140
Heat recovery	220 ~ 280
Solar thermal	270
Remote power	330 ~ 370

Using outlet temperature of coolant, we tried to combine organic Rankine cycle to fuel cell system to recover waste heat. To increase the system efficiency, we examined the optimal operating condition for ORC and several types of expander which can generate maximum power at given temperature range.

Considering operating characteristics of both systems, this paper conducted parametric study for the cogeneration system, and suggested optimal operating condition. Here, the main parameters that affect the system performance are current density, operating pressure, and evaporating pressure at expander inlet. This cogeneration system can generate more power than fuel cell system, alone.

1.2 Literature survey

There have been a few researches to study the interaction among components in fuel cell system. Considering importance of water distribution in stack, the researches for PEM fuel cell are focused on water management problem. Some studies tried to solve this problem by improving humidifying techniques and thermal management [3-5]. Issues associated with hydrogen as fuel is another serious problem for PEM fuel cell. Researchers tried to increase system efficiency by adapting recirculation system, and furl reformer [6-8]. In system scale, interaction between stack and blower is one significant problem related with system efficiency, because power consumption of blower take most part among power consumption in balance of plant [9-11]. However, these studies scarcely conduct validation about their paper, so they could not guarantee the same results for applying actual system. Moreover, previous studies conducted

their studies for sub-system for fuel cell, so their studies cannot explain behavior of whole system. Therefore, we need to examine system characteristics of whole fuel cell system which is shown in Fig. 1.3. Fuel cell system consists of four main parts; stack, fuel providing system, air providing system, and thermal management system. Stack can generate power using air and hydrogen as reactants, so air and hydrogen are provided by other sub parts. Air is provided by using blower, and hydrogen is provided by recirculation system. Additionally, membrane humidifier is applied to maintain proper humidity when air is entering the stack. Thermal management system manages the operating temperature of stack by using three way valve and radiator. Unfortunately, the study considering whole parts consisting fuel cell system is hardly conducted, so it is necessary to acknowledge the interaction among sub parts in the fuel cell system.

Since 1970's, the research for organic Rankine cycle has lively been conducted by many research groups. Some tried to find optimum working fluid for recovering low grade heat [12-14]. They conducted parametric study to compare the first law efficiencies for different working fluids; the promising working fluids are R245fa, R245ca, R123, and R141b. Properties of organic fluids and their T-s diagram are shown in table 1.2 and Fig. 1.4 [13]. The range of temperature of heat source is from 70 ^{o}C to 300 ^{o}C, and that of condenser is ranged from 35 ^{o}C to 60 ^{o}C. Others conducted optimization of the system with internal heat exchanger. Using several optimization tools, they tried to raise the thermos-dynamic efficiency of organic Rankine cycle [15-16]. Another effort to increase the system efficiency is conducted by designing expander [17-18].

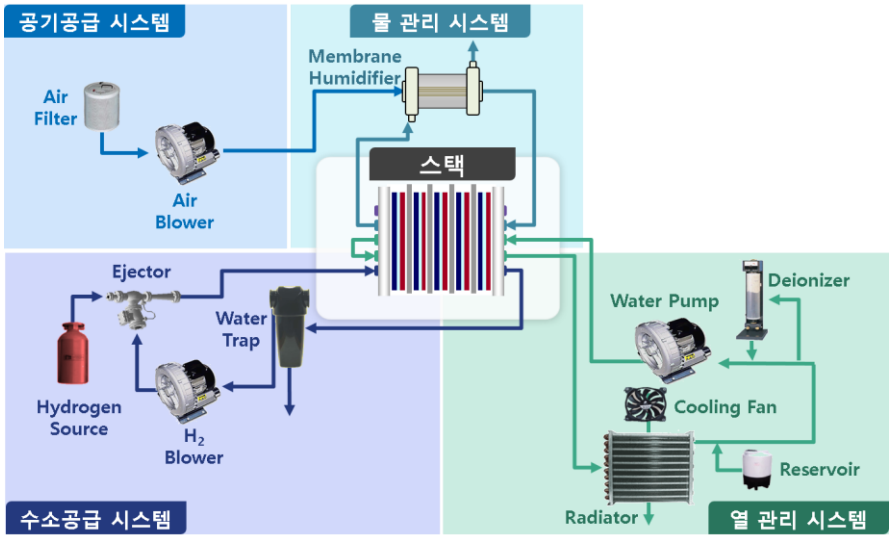

Fig. 1.3 Schematic diagram of fuel cell system.

Table 1.2 Properties of organic fluids [13]

Substance	Molecular mass (kg/kmol)	P_c (MPa)	T_c (ºC)	T_{bp} (ºC)
Water	18.02	22.06	373.95	99.974
R245fa	134.05	3.64	154.05	14.90
R245ca	134.05	3.93	174.42	25.13
R123	152.93	3.662	183.68	27.82
R141b	116.95	4.25	204.50	32.05

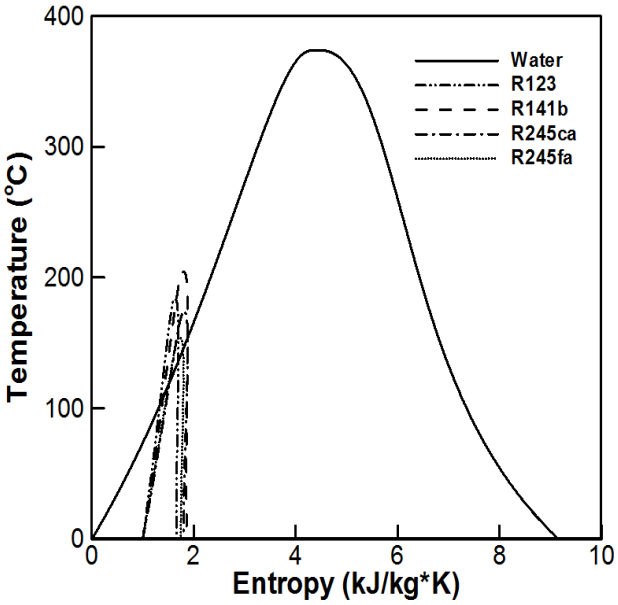

Fig. 1.4 T-s diagram of organic fluids compared to water [13].

Various types of expander, such as single-stage axial turbine, hermetic scroll expander and radial expander, are used to analyze the efficiency of the cycle. However, most studies were conducted by numerical study, so we can just predict the results. There is hardly heat transfer coefficient for R245fa, and the function of power consumption of pump is different from previous one, because viscosity of organic fluids are different from traditional working fluids. Therefore, experimental study to support the ideas associated with previous numerical studies is necessary. Studies for combined heat and power plant using organic Rankine cycle are lively conducted; generally, the cycle is coupled with geo-thermal and bio-mass, however, attempts to apply to lower heat sources have been conducted in these days. Several companies already success to apply organic Rankine cycle to recover waste heat from alternative energy sources [19]. However, application to low grade heat, especially below 100 ^{o}C is rarely found. Few studies for application of organic Rankine cycle using waste heat from PEM fuel cell system is conducted; they prepare cogeneration system using fuel cell system and organic Rankine cycle to find optimal working fluid [20]. Changing operating pressure and mass flow rate, they tried to find optimal operating condition. Although it handles the hybrid system for PEM fuel cell and organic Rankine cycle, they cannot consider important parts consisting fuel cell and the cycle, and the accuracy of their model is poor, because they did not validate their model. Therefore, experimental study for convincing the model is still needed to support the idea for cogeneration system which is consisted of PEM fuel cell system coupled with organic Rankine cycle.

1.3 Objectives and scopes

This study conduct numerical and experimental study to analyze the performance of cogeneration system which is consisted with PEM fuel cell coupled with organic Rankine cycle. In numerical study, complicated system model is conducted which include dynamic modeling for stack, and steady state model for stack, semi-empirical model for blower and other parts related with fuel cell system. These components are comprised to build system model for fuel cell. Additionally, iterative logic to represent operating characteristics of fuel cell system is carried out. For organic Rankine cycle model, each models is conducted and convinced through experiment, and we find heat transfer coefficient for heat exchanger using R245fa, and build semi empirical model for expander. In case of experimental study, we set up fuel cell system to know the dynamic response of fuel cell, and we conducted the experiment to elucidate the water transport mechanism through the Nafion 117 which is used for membrane humidifier and stack. For organic Rankine cycle, the cycle is prepared to propose several coefficients related with R245fa. Based on the results, we can convince heat exchanger, and expander model. Through the experimental set up, we can know the operating characteristics of organic Rankine cycle to recover low grade heat in a laboratory scale.

In chapter two, we examine transient response of stack according to pressure; and the pressure is controlled by interaction between blower and back pressure valve. Because we can know the real driving condition, we can develop proper driving strategy. At first, we develop model to analyze the

behavior of stack at dynamic condition to know the effect of pressure. The model is conducted using SIMULINK to show dynamic behavior of stack easily. This model is convinced by experiment which is carried by our experimental set up. By analyzing dynamic responses for different operating conditions, the study can develop operating strategy which can suggest stable driving by reducing the size of peaks.

In chapter three, the study suggest novel relationship to explain mechanism of water transport through Nafion 117. By considering the structural characteristics of Nafion, we suggest novel relationship to explain the water transport mechanism across the membrane. We assume the structure of Nafion as parallel-pore, and assume four different transport mechanism depending on relative humidity near each side of membrane. This idea is supported by experiment, and we analyze the mass transport by driving force to find important parameter that affect mass transport of water. By using novel equation, we can build more accurate stack model.

In chapter four, system model for fuel cell vehicle is carried out to analyze the performance of system according to operating pressure. We develop model for whole components consisting fuel cell car, and validate each model through experimental data which is supported by Hyundai Motor Corporation. The system model is utilized to predict the performance of fuel cell car, and develop performance curve depending on different velocity and load conditions. Moreover, we can know the effect of pressure on operating temperature and the amount of waste heat from fuel cell.

In chapter five, we conduct model for organic Rankine cycle to predict

performance of the cycle for low grade heat. Through the numerical analysis, we can select proper working fluid and type of expander. Experimental study can support the accuracy of the component model of the cycle, and show the real performance of organic Rankine cycle in a laboratory scale. Moreover, through the experimental results, we can understand effect of evaporating pressure, mass flow rate, and temperature of heat source and sink.

In chapter six, we can examine the operating characteristics of cogeneration system which is developed using previous studies. By using system model, we can conduct parametric study for the hybrid system. By changing pressure and temperature of each system, we can find optimal operating condition to maximize performance of cogeneration system.

Finally, the summary and conclusion are given with some suggestions for advanced research.

Chapter 2. Novel model to explain mass transport across the Nafion® 117

2.1 Introduction

In this chapter, a novel model explaining the water transport mechanism through Nafion® 117 is developed to understand the effects of parameters such as phase difference, pressure, mass flow rate, and temperature for applying polymer electrolyte membrane (PEM) fuel cell application. The model considers water uptake characteristics based on the polymer membrane structure and adopts four different processes to explain water permeability considering interfacial transport across the boundary. To understand the effect of phase difference, we change the relative humidity at each inlet of the experimental apparatus from 10% to 100%. The results suggest that capillary pressure is the most dominant factor in water transport across the membrane. When we change the pressure at each side of the apparatus from 1 to 3 bar, the water transport amount is maximized at 1 bar for each inlet. The mass flow rate varies from 1 to 5 Lpm. Moreover, the temperature effects on the water transport amount is analyzed. The above results are verified using measured data and compared with calculated results obtained by a conventional method. In the end, this study developed the empirical equation which can be used in the fuel cell model.

2.2 Numerical analysis for water transport mechanism across the Nafion® 117

A perfluorosulfonic acid polymer such as Nafion® 117 consists of a hydrophobic perfluoronated backbone and hydrophilic sulfonic acid functional groups. Two kinds of domains result from these structural characteristic. A hydrophobic perfluoronated backbone acts as the polymer matrix. It supports structure. Meanwhile, the other builds the water channel network in the hydrated condition. Based on the characteristics of the membrane, we suggest that Nafion® 117 has a parallel-pore structure, as shown in Fig. 2.1 (a). The ionic phase forms a 4-nm-diameter cylindrical cluster, and each cylinder is 1 nm away from each other [21]. This cylindrical cluster is hydrophilic and plays the role of a channel for liquid water, *i.e.*, hydraulic permeation. The remainder of the membrane is hydrophobic and acts as a channel for water vapor, *i.e.*, vapor permeation. Based on the characteristics of pervaporation which is derived from permeation and evaporation, we will treat this process as combination of above two processes. Because they have the same driving force and carriers. [22-23]

Since the mechanism of water transport through Nafion® 117 is closely related to water uptake in the membrane, we examine the characteristics of water sorption in the membrane. In this study, the water uptake processes in the membrane are divided into two steps based on the interpretation of the isopiestic sorption curve: relative humidity 0–75%, and over 75% [24]. Each former step stands for the case of vapor permeation and pervaporation, and

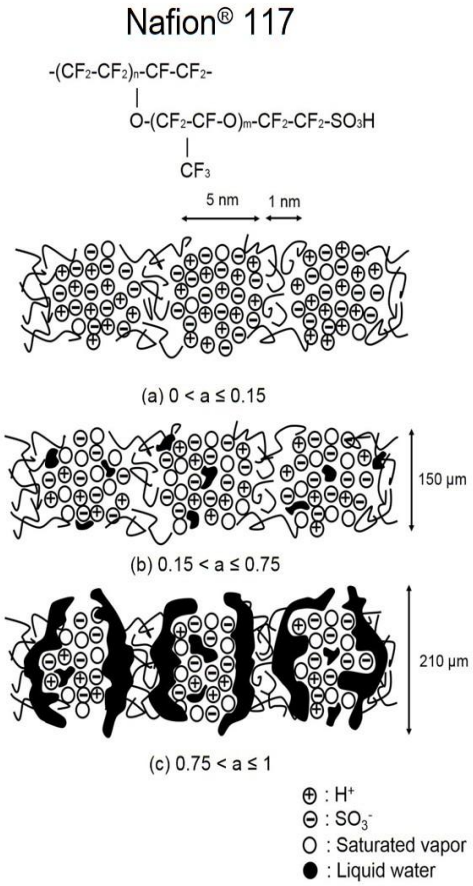

Fig.1 Schematic diagram of microstructures of Nafion® 117 and diffusion process of water molecules for different activities

Fig. 2.1 Schematic diagram of microstructures of Nafion® 117 and diffusion process of water molecules for different activities.

such as vapor or air might be transferred through the hydrophobic domain of Nafion® 117. And the membrane begins to absorb liquid water by increasing the amount of moisture. In this region, the dissociation of the protons from the acidic sites occurs and they develop hydronium ions with the absorbed water. The absorbed water is chemically bonded to ionic clusters. Therefore, we assume that liquid water exists as hydronium ions in the membrane (the concept of the existence of these ions is the same as the concept of water content employed in other studies) and that water molecules move across the membrane in the form of hydronium ions. These solvated hydronium ions hardly contribute to membrane swelling, and they only form a cylindrical ionic cluster with a charged site, as shown in Fig. 2.1 (b). This is why a relatively flat region is observed in the isopiestic sorption curve in this range [25-27]. And the thickness of the membrane in the region is not swell; approximately 150 μm. [28] After hydronium ions piled up at one side, flux of proton begins to move. We included this phenomenon as back diffusion. Considering above processes, equilibrium of mass transfer through the membrane is achieved.

When the relative humidity is higher than 75%, the charged site reaches saturation, so liquid water begins to condense near the cylindrical ionic cluster. By increasing the relative humidity, the amount of liquid water condensation also increases, which contributes to membrane swelling around the cylindrical cluster. Because of swelling, the thickness of the membrane around charged sites increases by 210 μm, as shown in Fig. 2.1 (c). Here, the thickness of swollen membrane is deduced by the ratio of Bragg space between dry and wet

state. [21] We assume that the thickness is linearly proportional to water content, and it is proportional to the third power of relative humidity resulted from the relationship between activity and water contents. [24, 29] Water uptake in this region is similar to physisorption; therefore, liquid water can move through extended volume of the membrane.

In all region, water vapor is one of the carriers that move through the hydrophobic domain of the membrane (*i.e.*, vapor permeation). Two forces drive the water vapor: diffusion caused by the difference in concentration at the upper and lower surfaces of the membrane, and convection caused by the difference in hydrostatic pressure in the chambers of the donor and receiver sides. We adopt Chapman and Enskog's method to estimate gaseous diffusion [30-31]. By introducing binary diffusion coefficient, we tried to consider the effects on other gases on diffusion of water. Here, the diffusion coefficient is expressed as shown below:

$$D_{ij} = \frac{0.00266 \cdot T_{mem}^{1.5}}{P \cdot 2(\frac{1}{M_i} + \frac{1}{M_j})^{0.5} \cdot \tau_{ij}^2 \cdot \Omega_D} \tag{2.1}$$

where T_{mem} is the temperature of the membrane, P is the pressure of the membrane, and M is the relative molecular weight. Here, *i* and *j* represent species associated with the diffusion of water vapor and air. τ_{ij} is the collision diameter determined as the arithmetic average for two species [32]:

$$\tau_{ij} = \frac{1}{2}(\tau_i + \tau_j) \tag{2.2}$$

Ω_D is the Brokaw relation for polar molecules [30]:

$$\Omega_D = \frac{A}{(T^*)^B} + \frac{C}{\exp(D \cdot T^*)} + \frac{E}{\exp(F \cdot T^*)} + \frac{G}{\exp(H \cdot T^*)} + \frac{0.19 \cdot \delta_{water}}{T^*} \tag{2.3}$$

Here, δ_{water} is expressed as follows [33]:

$$\delta_{water} = \frac{1.94 \times 10^{-3} \cdot \mu^2}{V_b \cdot T_b} \tag{2.4}$$

where μ is the dipole moment, V_b is the liquid molar volume at the normal boiling point, and T_b is the normal boiling point. Based on the relation given by Neufiuld *et al.*, the following constants are determined for water and air [32]: A = 1.06036, B = 0.1561, C = 0.193, D = 0.47635, E = 1.03587, F = 1.52996, G = 1.76474, and H = 3.89411. T^* is expressed as follows [32]:

$$T^* = \frac{k \cdot T_{mem}}{\varepsilon_A} \tag{2.5}$$

$\frac{\varepsilon_A}{k}$ is the geometric average between the water and air molecules. Here, the value of T^* is 1.18 [34]. Additionally, we consider the characteristics of the porous medium that would enable the membrane to obtain effective diffusivity, which is expressed as follows:

$$D_{eff} = \varepsilon \frac{D_{ij}}{\tau} \tag{2.6}$$

Here, ε is the porosity and τ is the tortuosity of Nafion® 117. Tortuosity is introduced for considering the behavior of longer distance in the pore. And tortuosity factor is assumed as the value for uniform pore case. [30, 35-36]

The mass flow rate can be calculated using the diffusivity; however, we have to reconsider the difference in concentration at the membrane surfaces between the donor and receiver sides. Due to interfacial mass transport, we

cannot obtain the concentration at the upper and lower surfaces of the membrane because the concentrations at the surfaces of the membrane and bulk are different depending on their characteristics. If the membrane is a hydrophobic material, the concentration at the membrane surface is lower than that in the chamber. Otherwise, if the membrane is a hydrophilic material, the inverse holds true. Some researches handled this situation by multiplying the concentration with a partial factor; however, we treat interfacial mass transport by introducing the concept of a chemical potential gradient [37]. We assume that diffusion flux is proportional to chemical potential as shown as follow.

$$-j_{diff,i} = \frac{D_0 c_i}{k_B T} \nabla \mu_i \tag{2.7}$$

Here, k_B is Boltzmann constant. And chemical potential per molecule is expressed as below.

$$\mu_i = \mu_i^0 + k_B T \ln \gamma_i c_i \tag{2.8}$$

Then, we can see follow.

$$-j_{diff,i} = [\frac{D_0 c_i}{k_B T}(\frac{\partial \mu_i}{\partial c_i})]\nabla c_i = [D_0(1+\frac{\partial \ln \gamma_i}{\partial \ln c_i})]\nabla c_i \tag{2.9}$$

Finally, we can obtain the interfacial mass transport shown as bellow.

$$\dot{m}_{tr,vap,diff} = -[D_{eff}(1+\frac{\partial \ln \gamma}{\partial \ln x})]\nabla C \cdot \frac{M_{vap} \cdot A_{hydrophobic}}{t_{mem,dry}} \tag{2.10}$$

Here, the diffusion coefficient is expressed as the value in square brackets. By introducing effective diffusivity, we can properly express the diffusion in porous media, Nafion membrane. [37] C is the molar concentration in the bulk, M_{vap} is the molecular weight of vapor, $A_{hydrophobic}$ is the area covered by the

hydrophobic domain of the membrane, $t_{mem,dry}$ is the thickness of the dry membrane, and x is the concentration ratio, which is expressed as follows:

$$x_i = \frac{C_i}{C} \tag{2.11}$$

The ratio of the molar concentration to the activity, γ, is defined as follows [37]:

$$\gamma = \frac{a}{C} \tag{2.12}$$

This term is introduced to consider the chemical potential per molecule. For calculating the gas flux driven by convection, we adopt Darcy's law derived from the Navier–Stokes equation, as expressed below [38]:

$$\dot{m}_{tr,vap,conv} = -\frac{k_p \cdot A_{hydrophobic} \cdot \rho_{vapor}}{v_{water}} \cdot \frac{\nabla p}{t_{mem,dry}} \tag{2.13}$$

where k_p is the permeability of Nafion® 117, and to consider the effect of temperature, k_p is express as follow. [39]

$$k_p = 6\times10^{-14}T - 1.4\times10^{-11} \tag{2.14}$$

v_{water} is the viscosity of water vapor, and ρ_{vapor} is the density of water vapor. These two transport mechanisms are only associated with the transport of water vapor, and these mechanisms act in every step of the water transport process.

When the water molecules are started to stay near the surface of membrane, the flow of hydronium ions begins inside the membrane (*i.e.*, pervaporation). And we expect that pervaporation is combination of vapor permeation and diffusion of hydronium ions. Hydronium ions move through the hydrophilic domain of the membrane driven by the difference in the water content, as defined by Springer *et al.* [24]. In this case, liquid water diffusion is expressed as follows:

$$\dot{m}_{tr,ion,diff} = D_w \frac{C_{donor} - C_{receiver}}{t_{mem,dry}} M_{vap} A_{hydrophilic} \tag{2.15}$$

where $A_{hydrophilic}$ is the area covered by the hydrophobic domain of the membrane and D_w is the diffusivity of a water molecule, which is expressed as follows [40]:

$$D_w = D_\lambda e^{2416(\frac{1}{303} - \frac{1}{T_m})} \tag{2.16}$$

where D_λ is the diffusivity of the water content in Nafion® 117. C is defined as follows:

$$C = \frac{\rho_{mem,dry}}{M_{mem}} \lambda \tag{2.17}$$

where $\rho_{mem,dry}$ is the density of dry Nafion® 117 and M_{mem} is the molecular weight of the membrane. λ is the water content, which is expressed as

$$\lambda = 0.0043 + 17.81a - 39.85a^2 + 36.0a^3 \tag{2.18}$$

where a is the activity, which is the same as the relative humidity.

Due to the behavior of hydronium ion, H+ ions also move, and it produces gradient of proton inversely proportional to the gradient of concentration of water. Along with the direction of flux of proton, water could be dragged and water drag coefficient is 2.5 ± 0.2 for fully hydrated membrane. [41] Based on this study, we assume that back diffusion is occurred when relative humidity is over 75 %. We followed the expression of back diffusion suggested by Springer *et al.* [24]

$$\dot{m}_{back,diff} = -\frac{\rho_{dry}}{M_m} D_\lambda \frac{d\lambda}{dt_{mem,wet}} \cdot \frac{A_{swelling} M_{water}}{t_{mem,wet}} \tag{2.19}$$

Intradiffusion coefficient of water, D_λ, is defined as follow.

$$D_\lambda = 10^{-6}\exp[2416(\frac{1}{303}-\frac{1}{273+T_{cell}})](2.563-0.33\lambda+0.0264\lambda^2-0.000671\lambda^3) \quad (2.20)$$

When the relative humidity is higher than 75% (*i.e.*, hydraulic permeation), the dissociation of the acid group in water ends. Liquid water begins to condense around the cylindrical cluster of the acid group, and the membrane starts to swell. Moreover, interfacial resistance can be negligible when the membrane is exposed to liquid [42-43]. In the extended volume, transport of liquid water occurs because of capillary pressure. In this case, transport of water vapor and diffusion of liquid water are still in progress. In the porous membranes, the different pressures are in equilibrium: pressure of liquid, p^l, that of gas, p^g, and capillary pressure due to the curvature of the liquid meniscus, p^c.

$$p^c = p^g - p^l \quad (2.21)$$

The capillary pressure in porous media is inversely proportional to the characteristic size of pore, which is shown as follow [44].

$$p^c \approx \frac{A\sigma\cos\theta_c}{df} \quad (2.22)$$

Here, σ is the interfacial tension between water and the membrane. And we express interfacial tension as function of temperature based on previous studies [45-46].

$$\sigma = 0.0276 - 2.456\times10^{-5}T \quad (2.23)$$

θ_c is the contact angle: 109.2° [47]. But we may put $\theta_c = 0$ when the membrane is completely wet. And df is the pore size of the membrane: 500nm [48]. For a cylindrical shape of pore, A is 2 [44]. Liquid water flux by capillary pressure is defined as follow.

$$j_{cap} = \frac{s^3}{v_{water}} k_p [\nabla p_c + (\rho_l - \rho_g) g] \tag{2.24}$$

s is the saturation factor, which is the ratio of the volume of liquid water to the void volume of porous media. s is proportional to the activity, as shown below.

$$s = 0.0219 \times a - 0.0037 \qquad \text{(if a > 0.75)}$$

$$s = 0 \qquad \text{(if a < 0.75)} \tag{2.25}$$

This linear relationship between saturation factor and activity is obtained by our modeling of stack conducted at former numerical study. [40] The saturation factor of the dry side is calculated by the above equations; however, that of the wet side does not follow the same pattern. It assumes that the case of condensation of liquid water in the polymer membrane is similar to the case of liquid water contacting with the membrane surface. Therefore, we assume that the values of θ_c and s at the wet side are 0 and 1, respectively, when liquid water starts to condense. The transport of liquid water because of capillary pressure is expressed as follows [44]:

$$\dot{m}_{tr,liq,cap} = -\frac{2\sigma \cos\theta_c}{v_{water}} \cdot \frac{k_p s^3}{df} \cdot \frac{A_{swelling} \cdot M_{water}}{t_{mem,wet}} \tag{2.26}$$

here, $t_{mem,wet}$ is the thickness of the wet membrane. And $A_{swelling}$ is the additional area formed by swelling. We assume that membrane swelling is observed around the cylindrical functional group and that liquid water overflows to the hydrophobic domain. Therefore, the hydrophilic area and some part of the hydrophobic area near the cluster extend their volume. This volume is proportional to the saturation factor, as shown below:

$$A_{swelling} = A_{hydrophilic} \frac{1nm}{(1+4)nm} \cdot \frac{150\mu m}{210\mu m} \times s \tag{2.27}$$

For the simplicity, we assume that the water content in membrane is linearly distributed. For the case of mass transport of liquid water, the effect of air is neglected. Due to the low solubility of air in water it hardly effects on the flux of water transport [49].

The total mass flow rate across the membrane is calculated considering all the processes, namely, the mass transport of vapor by diffusion and convection, mass transport of water hydronium ions by diffusion, and mass transport of liquid water by capillary pressure.

$$\dot{m}_{tr,tot} = \dot{m}_{tr,vap,diff} + \dot{m}_{tr,vap,conv} + \dot{m}_{tr,ion,diff} + \dot{m}_{tr,liq,cap} - \dot{m}_{back,diff} \tag{2.28}$$

The mass flow rate of water at each outlet is calculated as follows:

$$\dot{m}_{dry,out} = \dot{m}_{dry,in} + \dot{m}_{tr,tot} \tag{2.29}$$

$$\dot{m}_{wet,out} = \dot{m}_{wet,in} - \dot{m}_{tr,tot} \tag{2.30}$$

where $\dot{m}_{dry,in}$ is the mass flow rate at the inlet of the dry side, $\dot{m}_{dry,out}$ is that at the outlet of the dry side, $\dot{m}_{wet,in}$ is that at the inlet of the wet side, and $\dot{m}_{wet,out}$ is that at the outlet of the wet side.

The temperature at each outlet is calculated according to the law of energy conservation as shown below:

$$\sum \frac{dm_{d,out}}{dt} h_{out} = \sum \frac{dm_{d,in}}{dt} h_{in} + \frac{dm_{tr}}{dt} h_{tr} \tag{2.31}$$

Here, h is the enthalpy. Because the chamber is insulated, as is the experimental setup, heat loss to the environment is neglected. The relative

humidity at each outlet is obtained as follows:

$$RH_{out} = x_{H_2O} \frac{p}{p_{sat}} \tag{2.32}$$

Here, x_{H_2O} represents the mole fraction and is expressed as follows:

$$x_{H_2O} = \frac{n_{H_2O}}{n_{H_2O} + n_{O_2} + n_{N_2}} \tag{2.33}$$

The relative humidity terms at the inlets are input variables; therefore, we just need to calculate the relative humidity at the outlet.

In the case of model using Fick's law, we just follow a method suggested by Springer *et al.* that is widely used in numerical researches. They considered that transport of water molecules is resulted from gradient of water content. [50] It is the same way for explaining the flux of hydronium ions in this paper. And all parameters used in the model using Fick's law are the same as that in process of vapor diffusion of our model. Both are lumped model, and we are not consider concentration variations, flow direction or related parameters.

2.3 Experimental set up

The properties of Nafion® 117, which was used to examine the behavior of water molecules across the membrane, are summarized in Table 2.1. A chamber was designed to determine the amount of water transport through the membrane by measuring the relative humidity at each chamber outlet. The chamber consisted of two channels and two plates having 2 × 2 cm holes at their center, as shown in Fig. 2.2. Two single channels with dimensions of 2 × 2 × 2 cm were made using stainless steel panels and assembled together with two plates which are designed to fix the membrane. To control the temperature

around the membrane, a heating pipe was installed in the plates. Nafion® 117, which acted as the mass transport medium, was placed between two plates and fixed with a rubber gasket. In order to minimize the external disturbance from the ambient temperature, the chamber was insulated.

The experimental apparatus is shown in Fig. 2.3. Each sides of gas stream was regulated by a mass flow rate controller (Bronkhorst Corp.) and passed through a bubbler to gain desired moisture. Then, entering gas was gradually heated using a heating tape until they reach desired temperature at the inlet port of channel. The relative humidity at the inlet was controlled by the inlet and bubbler temperatures. A humidity sensor was placed outside of the outlet port to monitor the dew point temperature, and a dew point transmitter (Vaisala HMT337, measurement accuracy: 1°C) was used for measuring the dew point temperature. To control the pressure, a backpressure control valve (Tescom ER3000) was installed at the exit. The relative humidity was calculated as the ratio of the saturated water vapor pressure at a given temperature to that at the dew point temperature. The saturated water vapor pressure was calculated by the Goff–Gratch equation, which gives a method to estimate the saturation water vapor pressure at a given temperature [57]. And the same as other studies, we also cannot measure the mass flow rate at each outlet, because we can calculate the amount of mass transport of water molecules by using inlet mass flow rate and relative humidity at each inlet and outlet [25]. The experiments were conducted to examine the effects of differences in phase, pressure, mass flow rate, and temperature. We obtained the relative humidity values at each outlet and monitored the changes of the moisture between inlet and outlet.

Table 2.1 Parameter values employed in model for Nafion® 117 membrane.

Parameters	**Values**
Areas of membrane	4×10^{-4} m^2
Thickness of dry/wet membrane	150 μm / 210 μm [51]
Pore size of the membrane	12 Å [52]
Diameter of ionic channel	5 nm [53]
Distance between ionic channel	1 nm [53]
Equivalent weight of the membrane	1.1 kg/mol [21]
Density of dry membrane	2.075×10^{3} kg/m^3 [21]
Thermal conductivity of membrane	4.55×10^{-4} kW/mK [54]
Porosity of membrane	0.28 [55]
Tortuosity	6 [56]
Contact angle	150°
Kinematic viscosity of liquid water	0.475×10^{-6} m^2/s
Kozeny constant	6 [56]

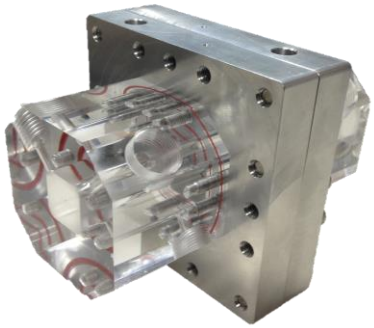

(a) External image of test chamber

(b) Inner view of stainless steel plate

Fig. 2.2 Image of test chamber.

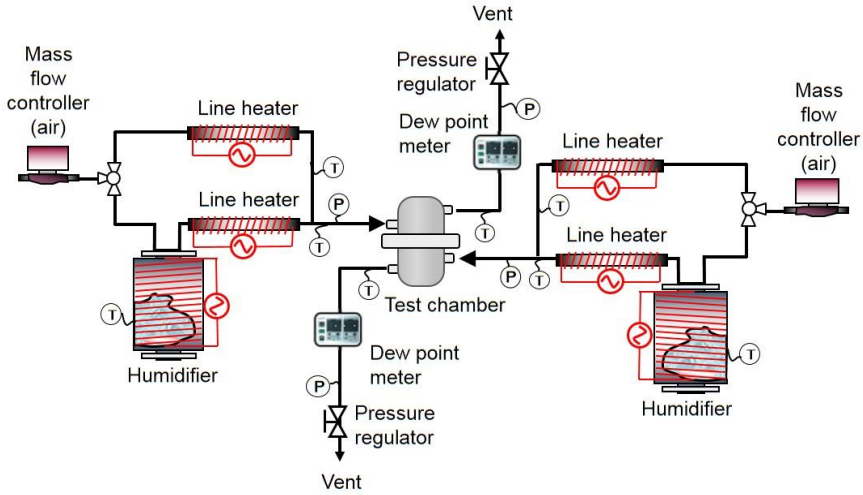

Fig. 2.3 Schematic diagram of the system.

2.4 Effect of relative humidity

The purpose of this section is to discuss the accuracy of the proposed model and to identify the contribution of each mechanism to the amount of water transport through Nafion® 117. Every result is verified using experimentally measured data to validate our model, and our results are compared with those obtained using a conventional model based on linear permeation equation (*i.e.*, Fick's law) suggested by other studies [58-59] to illustrate the advantages of our model. Lastly, we suggest empirical equation to calculate water transfer across the membrane.

To analyze the effect of phase differences on water transport, we change the relative humidity from 10% to 100% maintaining other variables constant; temperature is 65 ^{o}C, pressure is 1 bar, and mass flow rate is 5 lpm at both sides. The relative humidity at the inlet of the wet (donor) side is adjusted to 10%, 25%, 50%, and 100%. Water transport in the vapor phase through the hydrophobic domain is studied at the case of the relative humidity of 10%. Whereas, by analyzing the cases of the relative humidity of 25% and 50%, we can understand the behavior of hydronium ions in charged sites. Lastly, the water transport in the liquid phase of the hydrophilic domain is studied in the cases of the relative humidity of 100%. The relative humidity at the dry (receiver) side is also varied to show the effect of the difference in relative humidity between the two sides.

The results of our model agree well with the experimental results, as shown in Fig. 2.4. The results of the model based on Fick's law have the same

Table 2.2 Operating conditions for the effects of difference of relative humidity

Parameters	cases	Values	
		Dry inlet	Wet inlet
Temperature (ºC)		65	65
Pressure (Bar)		1	1
Mass flow rate (lpm)		5	5
Relative humidity (%)	#1	10	10
	#2	10	25
	#3	25	25
	#4	10	50
	#5	25	50
	#6	50	50
	#7	10	75
	#8	25	75
	#9	50	75
	#10	75	75
	#11	10	100
	#12	25	100
	#13	50	100
	#14	75	100
	#15	100	100

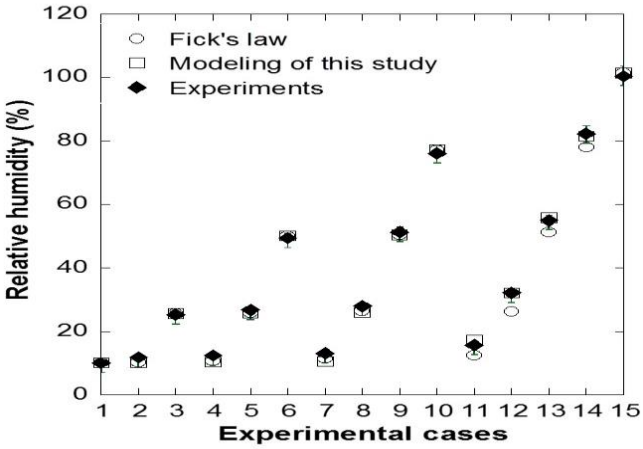

(a) Relative humidity at dry side outlet

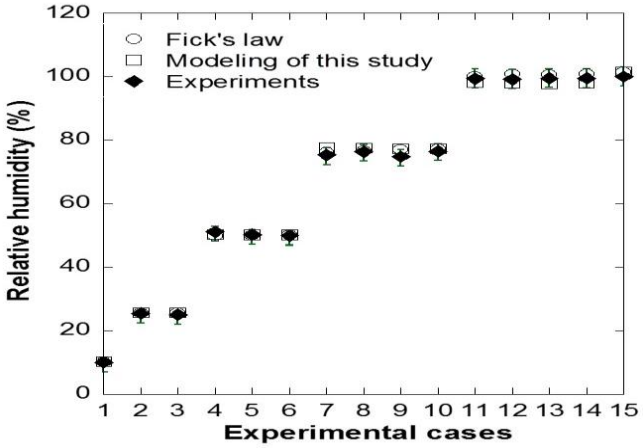

(b) Relative humidity at wet side outlet

Fig. 2.4 Comparison of relative humidity at the dry and wet side outlets for various inlet relative humidity.

trend with the experimental results, except the higher relative humidity region, which represent the regions where the liquid phase begins to form. Because two-phase flow is not considered in the conventional model, some inaccuracies are found in these regions. As a result, average error of relative humidity at dry side outlet is 7.1 % for model using Fick's law, and 5.3 % for our model. For average error of relative humidity at wet side outlet is around 1 % for both models.

The relative humidity at the dry side outlet rises as the relative humidity at the wet side inlet is increased. And we can find that the increase of relative humidity at dry outlet is larger in higher relative humidity region. It means that liquid water have significant effects on transport of water molecules. Based on these results, it seems that the amount of water transport is maximized when the relative humidity is kept at 100% at the wet side inlet and when the difference in relative humidity between the two sides is the largest (Fig. 2.5). The amount of vapor diffusion seems linearly proportional to the difference in the relative humidity between the dry and wet side inlets, as shown in Fig. 2.5 (a). The mass transport of hydronium ions by diffusion is also proportional to this difference. However, it shows nonlinear behavior, as shown in Fig. 2.5 (b). Because water content in the membrane is a main factor governing the mass transport, the results are related to the water content and not to the relative humidity. In addition, because there is no difference in hydrostatic pressure, no flux is generated by convection. When water flux is driven by capillary pressure, no remarkable difference exists under relative humidity of around 70 %, which are the regions before condensation to liquid water occurs. When the relative

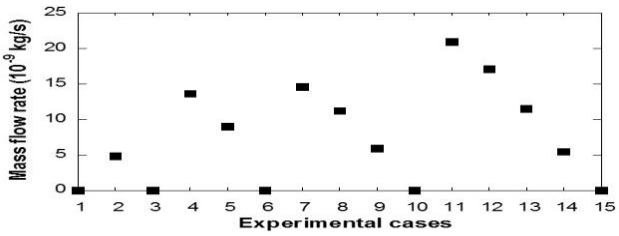

(a) Mass flow rate of vapor by diffusion

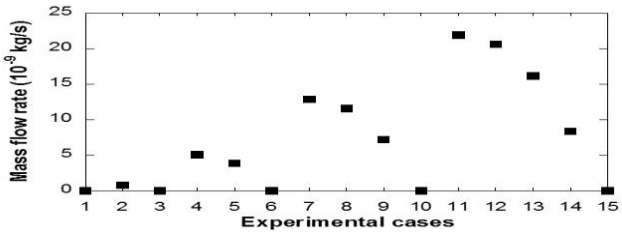

(b) Mass flow rate of hydronium ions by diffusion

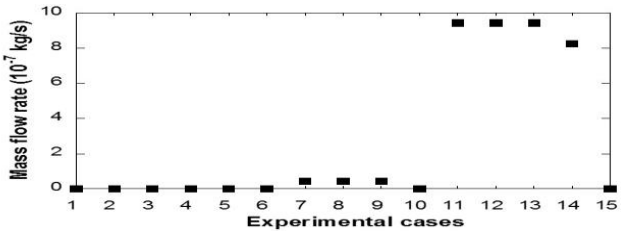

(c) Mass flow rate of liquid water by capillary pressure

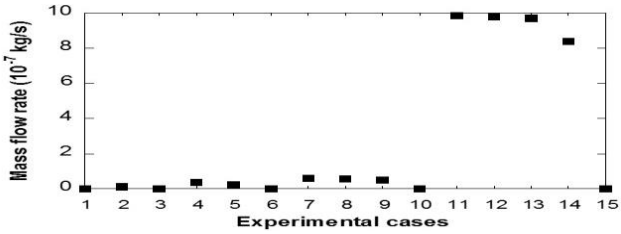

(d) Total mass flow rate of water molecules

Fig. 2.5 Mass flow rate of water molecules depending on several driving forces for various inlet relative humidity.

humidity is 100% at the wet side inlet, i.e., when liquid water begins to condense, the amount of water transport increases greatly, as shown in Fig. 2.5 (c). This shows that the liquid phase is more favorable to the movement of water molecules across the membrane, especially those driven by capillary pressure.

However, the amount of mass transport calculated by the first two processes are several orders smaller than that calculated by capillary pressure. Therefore, the tendency of the total water transport is similar to that of liquid water driven by capillary pressure, as shown in Fig. 2.5 (d).

2.5 Effect of pressure

Pressure can easily be changed depending on types of auxiliaries, mass flow rates, target stoichiometric number, or other operating conditions. Therefore, knowing the pressure effects on the membrane is important even very small deviation. However, previous studies are insufficient to explain the effect of pressure. Because the change in pressure is expressed only in the molar concentration in conventional theory [43].

The experimental conditions for analyzing the effect of pressure on water flux through Nafion® 117 are the same as that in above cases except pressure. In this case, we keep the relative humidity to be 100% at the wet side and 50% at the dry side because it is important to consider water transport of liquid and vapor phases both. Pressure is varied from 1 to 3 bar at each side.

The results predicted using our model match the measured data more precisely than the results obtained by the model using Fick's law. The amount of water transport calculated by Fick's law is much smaller than the measured

value, which means that using only Fick's law is insufficient to explain the effect of pressure on the water flux. The average error for model by Fick's law shows 7% for relative humidity at dry side outlet and our model shows 2 %. And average error of conventional model shows 3.5 % and that of new model shows 1 % at wet side outlet. The relative humidities at the wet side outlet are shown in Fig. 2.6 (b). The mass flow rate for the water transport to the dry side is 1.95×10^{-7} kg s^{-1}; and, the amount of temperature decreases are negligible, under 1 K.

Table 2.3 Operating conditions for the effects of difference of pressure

Parameters	Experimental cases	Values	
		Inlet at dry side	Inlet at wet side
Temperature (ºC)		65	65
Pressure (Bar)	#1	1	1
	#2	2	1
	#3	3	1
	#4	1	2
	#5	2	2
	#6	3	2
	#7	1	3
	#8	2	3
	#9	3	3
Mass flow rate (lpm)		5	5
Relative humidity (%)		50	100

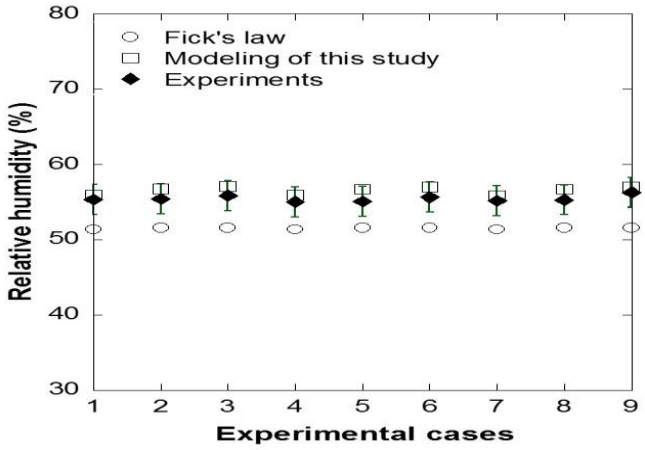

(a) Relative humidity at dry side outlet

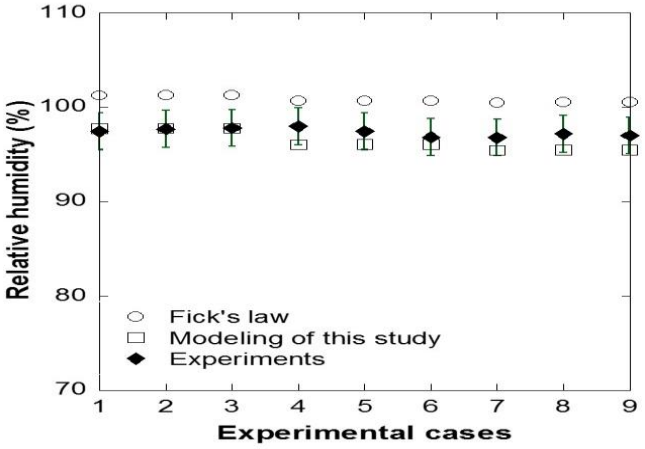

(b) Relative humidity at wet side outlet

Fig. 2.6 Comparison of relative humidity at the dry and wet side outlets for various inlet pressure (see table. 3.3).

The amount of water flux through the membrane increases with an increase in pressure at the dry side, and the effect of pressure at the wet side is almost negligible. This means that changes in the pressure gradient are not important to the mass transport of water. We can explain this phenomenon by analyzing different processes. For water vapor diffusion, vapor transport is inversely proportional to pressure; especially, the pressure at the wet side is more effective than that at the dry side, as shown in Fig. 2.7 (a). As the pressure increases, the absolute humidity decreases and the mass flow rate of vapor also decreases. This decrease is more significant at the wet side; hence, the pressure at the wet side is more important to the transport of water vapor through the membrane. The amount of the variation is 7.04×10^{-9} kg s^{-1}. In the case of convection driven by a difference in the hydrostatic pressure, the mass transport is proportional to the pressure gradient, as shown in Fig. 2.7 (b). Flux is generated in the forward and backward directions depending on the pressure gradient; however, the mass flow rate generated by convection is several orders smaller than that generated by other processes. The diffusion of hydronium ions (in the form of water vapor) is inversely proportional to the pressure at the wet side; however, the tendency of the ions transfer by the pressure at the dry side is the opposite. And the pressure at wet side is dominant for mass flow rate across the membrane. This is resulted from the relationship between pressure difference and gradient of water content at each interface. An increasing pressure difference leads to a steeper gradient of the water content in the membrane, therefore, the hydronium ions transported by diffusion is maximized at high pressure at dry side and low pressure at wet side, as shown

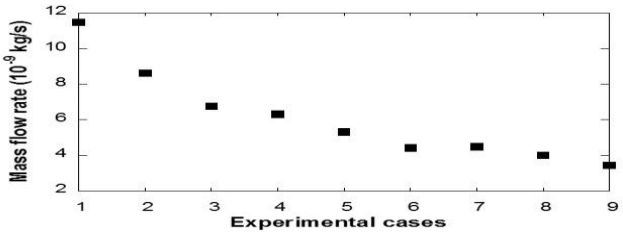

(a) Mass flow rate of vapor by diffusion

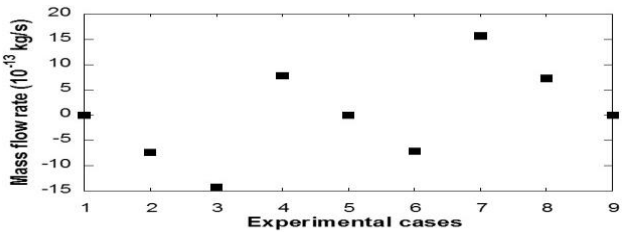

(b) Mass flow rate of vapor by convection

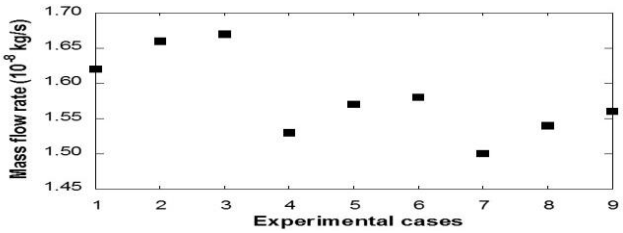

(c) Mass flow rate of hydronium ions by diffusion

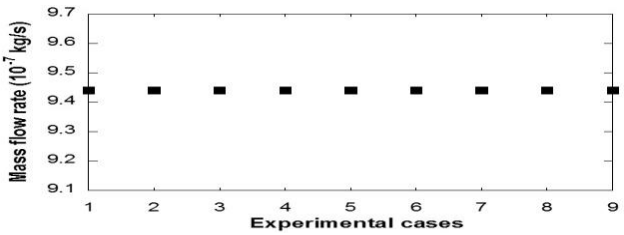

(d) Mass flow rate of liquid water by capillary pressure

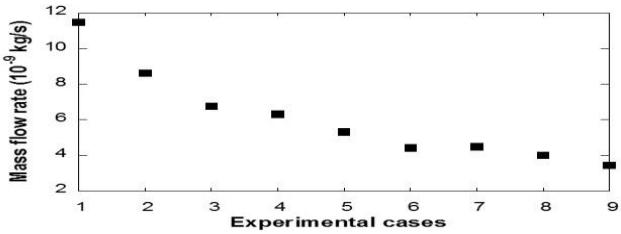

(e) Total mass flow rate of water molecules

Fig. 2.7 Mass flow rate of water molecules depending on several driving forces for various inlet pressure.

in Fig. 2.7 (c). In contrast, there is no variation in the liquid water transport driven by capillary pressure, and its value is 9.44×10^{-7} kg s^{-1}. Because the surface tension is mainly influenced not by pressure but by temperature, there is almost no change in the liquid water transport by capillary pressure. The total mass transport of water is shown in Fig. 2.7 (d). The main parameter that determines the total mass transport is the diffusion of vapor during pressure changes.

2.6 Effect of mass flow rate

The flow conditions on both sides of the membrane change in various ways. In membrane humidifier, the mass flow rate of the dry side often is nearly twice more than that of the wet side. [45-46] On the other hand, large amount of humid air and relatively small amount of dry hydrogen place near the membrane in the stack. Therefore, understanding of the effect of mass flow rate for water transport is important. The experimental cases used for analyzing the effect of the mass flow rate on the water transport across the membrane are the same as previous sections. But, the mass flow rates are varied from 1 to 5 Lpm.

It is found that the model using Fick's law cannot reflect the experimental results well, on the other hand, the proposed model is more accurate. Although the differences are greater when the mass flow rate is large, most results are within acceptable error margins. The average error is 13 % for model using Fick's law and 4.6 % for our model at dry side outlet. And the average error at wet side outlet is 3.2 % for model by Fick's law, 1.6 % for our model.

Relative humidity at dry side outlet decrease at higher flow rate at dry

side as shown in Fig. 2.8. There are two main reason for this result: shorter residence time and relative larger pressure drop. Due to higher flow rate, the residence time near the membrane is short, and the membrane hardly hold the moisture at the interface. Second, larger pressure drops at higher flow rate. It leads to lower partial pressure of vapor at dry side, and it lower the relative humidity at dry outlet. On the other hand, the tendency of the mass flow rate of wet side for the relative humidity is different from that of dry side; relative humidity at dry side outlet increase at higher mass flow rate of wet side. If flow rate of wet side increase, water molar flow rate also increase at wet side, and concentration of wet side become higher. Though presence of water molecules transferred across the membrane, it does not increase at the same rate as the increase of flow rate of water entering the chamber. Therefore, difference of concentration between two interfaces increase at high flow rate, and relative humidity of dry side outlet increase at high flow rate. Comparing the results between Fig. 2.8 and 2.9, we can find interesting phenomena about the relationship relative humidity and the water flux. The direction of relative humidity and water flux is opposite according to increase of flow rate of dry side. The water transport across the membrane increases at higher flow rates. Although the relative humidity decrease at higher flow rate, it increase the concentration difference between the interfaces. And it increase the water transport across the membrane. As a result, we can observe that relative humidity decrease but water flow rate increase at higher flow rate region.

Table 2.4 Operating conditions for the effects of difference of mass flow rate

Parameters	Values	
	Inlet at dry side	Inlet at wet side
Temperature (ºC)	65	65
Pressure (Bar)	1	1
Mass flow rate (lpm)	1	1
	3	1
	5	1
	1	3
	3	3
	5	3
	1	5
	3	5
	5	5
Relative humidity (%)	50	100

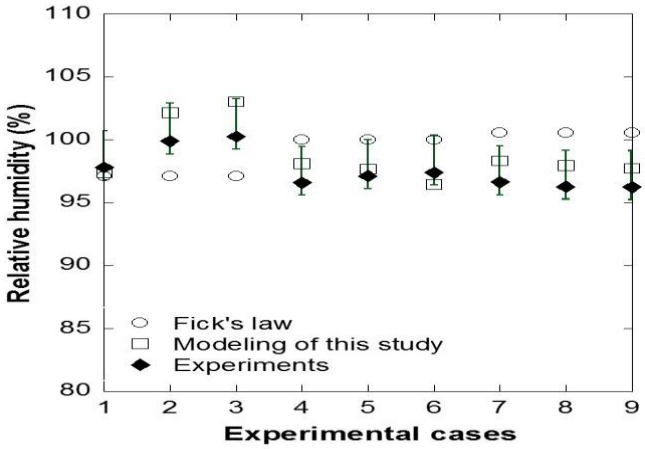

(a) Relative humidity at dry side outlet

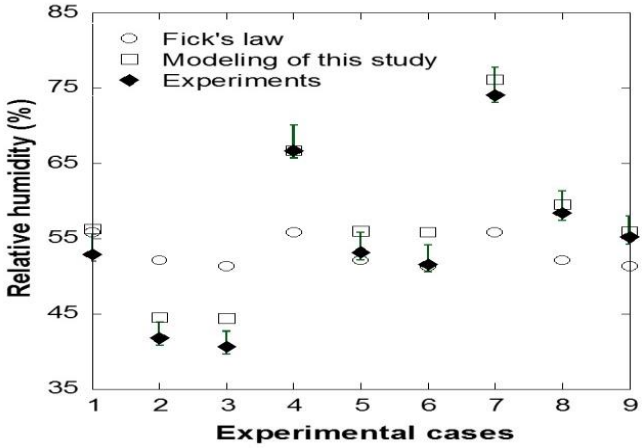

(b) Relative humidity at wet side outlet

Fig. 2.8 Comparison of relative humidity at the dry and wet side outlets for various inlet mass flow rate (see table. 3.4).

In the case of hydronium ion transport, the driving force is the gradient of the water content, which is a function of the activity. The activity is proportional to the number of moles of water, which means that the activity is also proportional to the concentration at each side. Therefore, the mass flow rate of liquid water across the membrane reduces with an decreasing mass flow rate at the dry side, as shown in Fig. 2.9 (b). The same inference can be drawn from Fig. 2.9 (c). However, the water flux at higher mass flow rate remain almost unchanged. It seems that when fully humidified gas is sufficiently supplied to the chamber, the interface of membrane is also fully wet, so the amount of water flux across the membrane is almost constant regardless of the concentration at dry side.

The total mass transport of water is shown in Fig. 2.9 (d). The most important process influencing the total amount of water transport is the liquid water driven by capillary pressure. In general, water flux increase at lower flow rate region generally. However, constant amount of water can be delivered when a sufficient amount of water is supplied.

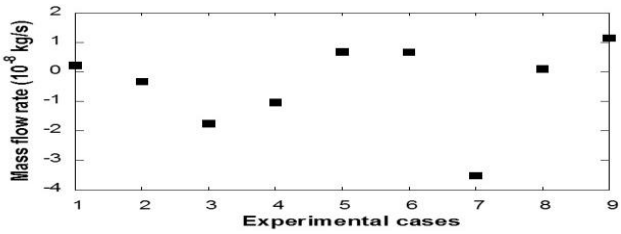

(a) Mass flow rate of vapor by diffusion

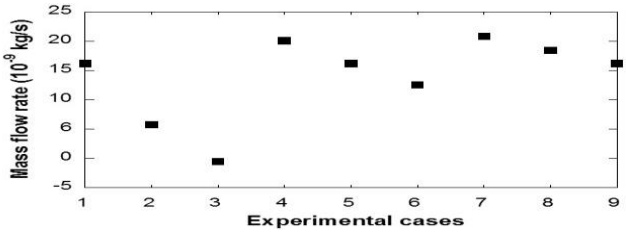

(b) Mass flow rate of hydronium ions by diffusion

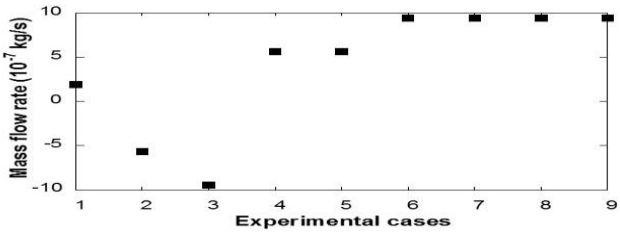

(c) Mass flow rate of liquid water by capillary pressure

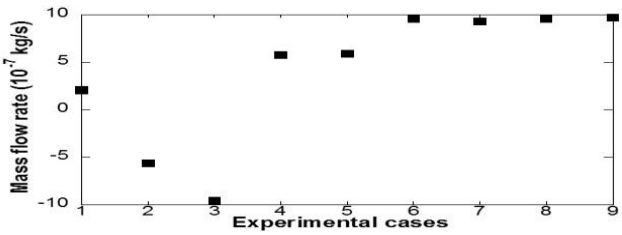

(d) Total mass flow rate of water molecules

Fig. 2.9 Mass flow rate of water molecules depending on several driving forces for various inlet mass flow rates.

2.7 Effect of temperature

To understand the effect of temperature on the water transport across the membrane, we perform nine experiments; temperature is varied from 35°C to 65°C, and the other parameters remain steady. To eliminate disturbance from other heat sources, the chamber is covered with an insulator.

The experimental data in this case have a relatively large scope for error. The average errors at dry side outlet is 30.2 % for conventional model and 14.5 % for new model. And the error for wet side outlet is 5.6 % for model using Fick's law and 4.4 % for our model. Neither the results of proposed model nor those of model using Fick's law match well with the experimental results. The empirical relationship associated with temperature may be the cause of these differences. However, the tendencies shown by the measured data and our model are similar, and thus, the temperature phenomenon is worth analyzing using our model.

The relative humidity at the dry side outlet generally increases with an increase of temperature at the dry side inlet. On the other hand, when the temperature at wet side is hotter than that of dry side, the relative humidity at the dry side outlet can be decreased below that of inlet as shown in Fig. 2.10 (a). To explain this results, we have to understand the amount of water transport of each process. For the flux of water vapor, the amount of mass transport increases with higher temperature. The same trend is observed during hydronium ion transport driven by diffusion as shown in Fig. 2.11 (a), and (b). Increase of diffusivity is the factor that results in this trends; the diffusivity is

Table 2.5 Operating conditions for the effects of difference of inlet temperature

Parameters	Values	
	Inlet at dry side	Inlet at wet side
Temperature (ºC)	35	35
	50	35
	65	35
	35	50
	50	50
	65	50
	35	65
	50	65
	65	65
Pressure (Bar)	1	1
Mass flow rate (lpm)	5	5
Relative humidity (%)	50	100

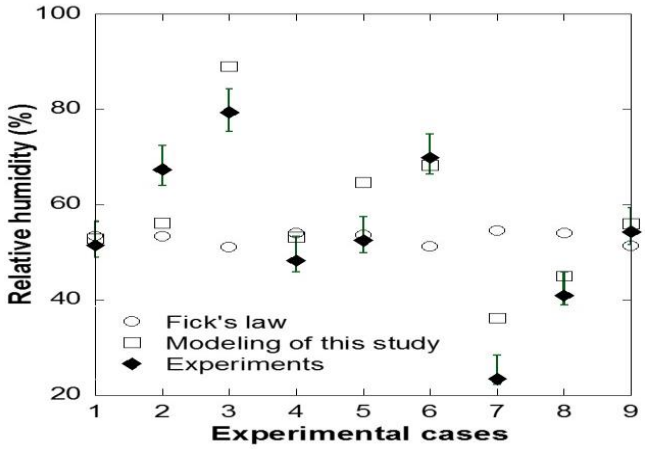

(a) Relative humidity at dry side outlet

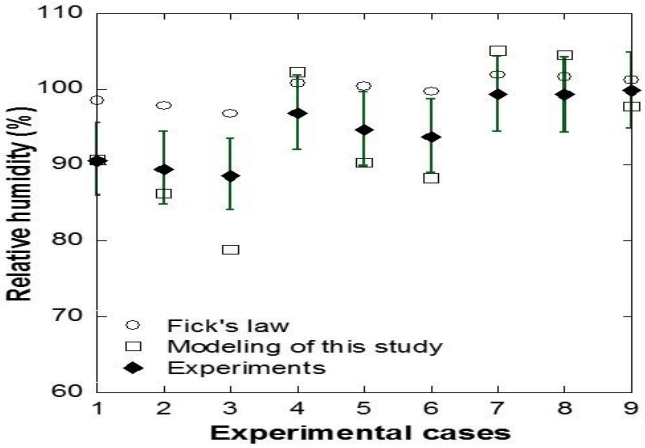

(b) Relative humidity at wet side outlet

Fig. 2.10 Comparison of relative humidity at the dry and wet side outlets for various inlet temperarture (see table. 3.5).

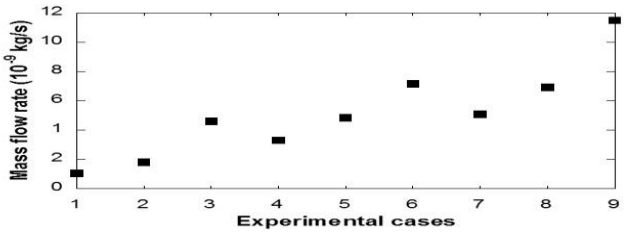

(a) Mass flow rate of vapor by diffusion

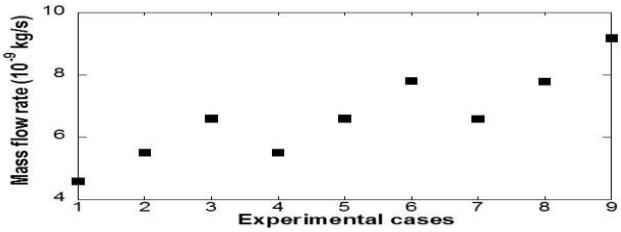

(b) Mass flow rate of hydronium ions by diffusion

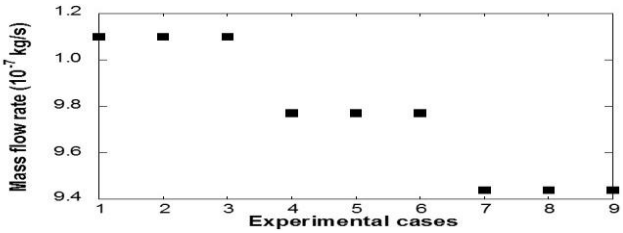

(c) Mass flow rate of liquid water by capillary pressure

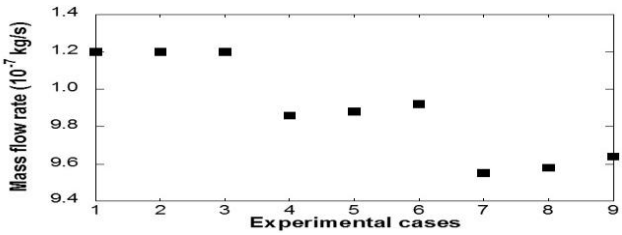

(d) Total mass flow rate of water molecules

Fig. 2.11 Mass flow rate of water molecules depending on several driving forces for various inlet temperature.

proportional to the cube of the square root of temperature. Although the gradient of chemical potential is changed depending on temperature, it hardly affect trend of mass transport. In the case of liquid water transport driven by capillary pressure, the surface tension is inversely proportional to the temperature. Especially, the temperature at the wet side is more important for surface tension because liquid water is in contact with the surface at the wet side. Therefore, the surface tension reduces with a decreasing temperature at the dry side, as shown in Fig. 2.11 (c). The most important process influencing the total amount of water transport is capillary pressure because the values are several orders higher than that obtained by other processes. Though consideration of flow rate of vapor and hydronium ions, the amount of water flow can be diminished at higher temperature region. Including reduced amount of water transport and temperature increase at outlet, relative humidity at dry side outlet can be decreased.

Based on the above analysis, it seems that the water transport through the membrane is mainly delivered in the form of liquid water. Therefore, water can flow from a low relative humidity region to a high relative humidity region.

2.8 Summary

In this study, a novel model that explains the mechanisms of mass transport through Nafion® 117 is developed to understand the water permeability considering interfacial transport across the boundary. Through this model, we can explain the effects of operating parameters such as differences in phase, pressure, mass flow rate, and temperature on water sorption and mass transport

in Nafion® 117. Additionally, the advantages of the proposed model compared with a conventional method based on linear permeation equation are presented. On the basis of experiments performed by changing the relative humidity at each inlet, we infer that the liquid water transport driven by capillary pressure is the most dominant process determining the total mass flow rate across the membrane. The water transport by this process occupies more than 96% of the total mass transport. The water transport is maximum when the relative humidity of 10% at the dry side inlet and 100% at the wet side inlet. Furthermore, to study the migration of water, the pressure is changed at each side. The mass flow rate is maximized when the pressure at the dry and wet side inlets is 1 bar. In this case, the water vapor transport driven by diffusion is the most important process. When the mass flow rates are changed at each inlet, the maximum value of water transport is observed at a mass flow rate of 5 Lpm at both the inlets. Because of capillary pressure, liquid water plays a great role in transferring water across the membrane. While diffusion is proportional to the temperature, the total amount of water transport is inversely proportional to the temperature because of surface tension. The characteristics of surface tension are opposite to those of diffusivity, and the effect of surface tension is more significant. Therefore, the amount of water transport decreases with an increasing temperature at the wet side inlet, and it increases with an increasing temperature at the dry side inlet. In addition, we proposed a new equation explaining transferring of water molecules through the membrane that can be used in every numerical models using Nafion® 117. In summary, using the proposed model, we can understand transport phenomena across the membrane.

Chapter 3. Performance analysis of fuel cell car

3.1 Introduction

Numerical study on the performance of the polymer electrolyte membrane fuel cell vehicle was conducted to investigate the effect of blower and backpressure control valve. We conducted system level modeling for PEM fuel cell vehicle to predict its performance, especially, the model is conducted based on fuel cell car which is manufactured by Hyundai-Kia Motors and we can obtain its reliability through the verification of the driving data. Firstly, we considered most parts of PEM fuel cell vehicle. Models of sub systems were developed based on one dimensional model, but they contained important phenomena occurring in each devices. Then, we developed the system model which reflects configuration of PEM fuel cell vehicle; we prepared blower, membrane humidifier, and backpressure control valve at cathode, hydrogen recirculation system using ejector at anode, and the system for refrigeration and air conditioning. Among the components of system, we focused on the effect of blower and backpressure control valve in cathode side, because they have great influence on the operating characteristics of cathode and performance of vehicle. As RPM of blower increases, stoichiometric number becomes higher and relative humidity becomes lower. The variation of stoichiometric number and relative humidity reduces system output at higher RPM, although power generation of stack is generally higher at higher RPM of blower. In case of backpressure control valve, the stoichiometric number is higher, and relative

humidity is lower at larger angle of backpressure control valve. Therefore, the system power begins to reduce as the angle increases. In the end, we developed the performance curve depending on the blower RPM, and valve angle at different vehicle speed. Through the performance curve, we can predict every system output for fuel cell vehicle.

3.2 Methodology

System model developers should consider important feature of system as well as computational cost, therefore, many researchers have one dimensional model to conduct system modeling which can express physical phenomena in devices and reduce cost for analysis. Thus, we decide to develop our system model using simplified one-dimensional.

PEM fuel cell vehicle consists of three subsystems; air providing system, fuel providing system, and thermal management system, which are expressed in Fig. 3.1. Despite plenty of devices to consider, in this paper, we focus on identifying system configuration, so we just follow previous studies for modeling for sub device. However, we suggest PEMFC system model close to actual operation which is validated with driving data provided Hyundai-Kia Motors. The proposed modeling approach is implemented in Matlab environment and all properties used in the model are acquired by REFPROP 8.0.

Stack

Transient phenomena occurring in the fuel cells are explained by using an

in-house, theoretical model, in order to fully analyze the interactions between parameters. The stack and manifolds at every inlet and outlet of the fuel cell were taken into consideration in the dynamic model. We divided the fuel cell system into five sections, namely, the anode and cathode channels, anode and cathode GDLs, and MEA. The reactant gases entered the fuel cell through the inlet manifold and flowed through the channels and GDLs before reaching the membrane [60]. After reaction, the products were emitted through the GDLs, channels, and outlet manifold [61]. All of these phenomena were modeled in in-house dynamic model, which was developed by using the Mathworks MATLAB/Simulink and REFPROP 8.0. The latter is a program providing the thermodynamic properties of the fluids developed by National Institute of Standards and Technology (NIST). It is noted that all the geometrical details or other thermodynamic and materials' properties used for the modeling were the same as those of the experiment. There are some other modeling parameters borrowed from the references [60], which are mentioned accordingly in the following paragraphs.

The mass conservation of hydrogen, water vapor, and liquid water in the cell is as follows:

$$\frac{dm_{ch}}{dt} = \dot{m}_{gas.ch.in} - \dot{m}_{gas.ch.out} - \dot{m}_{gas.GDL2ch} \tag{3.1}$$

$$\frac{dm_{V.ch}}{dt} = \dot{m}_{V.ch.in} - \dot{m}_{V.ch.out} + \dot{m}_{V.GDL2ch} + \dot{m}_{evap.ch} \tag{3.2}$$

$$\frac{dm_{l.ch}}{dt} = \dot{m}_{l.ch.in} - \dot{m}_{l.ch.out} + \dot{m}_{l.GDL2ch} - \dot{m}_{evap.ch} \tag{3.3}$$

where $\dot{m}_{gas.ch.in}$ and $\dot{m}_{gas.ch.out}$ are respectively the mass flow rates of the

gases entering and exiting the channels, and $\dot{m}_{gas.GDL2ch}$ is the mass flow rate of the gases across the interface between the GDLs and the channels; $\dot{m}_{V.ch.in}$, $\dot{m}_{V.ch.out}$, $\dot{m}_{V.GDL2ch}$, $\dot{m}_{l.ch.in}$, $\dot{m}_{l.ch.out}$, and $\dot{m}_{l.GDL2ch}$ are the corresponding values for the water vapor and liquid water; and $\dot{m}_{evap.ch}$ is the evaporation mass flow rate in the channels. The change in the mass flow rate due to evaporation in the channels is calculated from the amount of liquid water that enters the channels and the amount of vapor generated in the channels. That is,

$$\min\left(A_{fc} \cdot \left(P_{sat}\left(T_{st}\right) - P_{V.ch} \right) \cdot \sqrt{\frac{M_V}{2\pi R \cdot T_{st}}}, \dot{m}_{l.GDL2ch} \right) = \dot{m}_{evap.ch} \tag{3.4}$$

where A_{fc} is the area of the fuel cell, $P_{sat}\left(T_{st}\right)$ is the saturation pressure at the operating temperature, and $P_{V.cach}$ is the partial pressure of the vapor in the channel. The outlet mass flow rate is determined by the pressure difference between the inlet and outlet, and is calculated as follows:

$$K_{ch.out} \cdot \Delta P = \dot{m}_{gas.ch.out} \tag{3.5}$$

$$\frac{R \cdot T_{st}}{M_V \cdot V_{ch}} \cdot m_{V.ch} = P_{V.ch} \tag{3.6}$$

where $K_{ch.out}$ is a characteristic constant of 0.01, which is used to calculate the outlet mass flow rate based on ΔP, or the pressure difference between the inlet and outlet.

Because the fluid movement in the GDLs is very complicated, the GDL model was divided into gas transport and liquid transport for simplicity. In the case of the gas phase, the mass flow rate into the GDLs is determined by the rate of vapor production. Although the consumption of the fuel occurs instantly near the membrane, time is required for the fuel supply to reach the membrane. The following equations are relevant:

$$\frac{I_{st}}{4F \cdot A_{fc}} = N_{gas.react} \tag{3.7}$$

$$A_{fc} \cdot M_{gas} \cdot N_{gas.react} = \dot{m}_{gas.GDL2ch} \tag{3.8}$$

where I_{st} is the current, F is the Faraday number, and $N_{gas.react}$ is the mole flux required for the reaction.

Regarding the GDLs on the cathode side, the concentration of each reactant and water vapor near the membrane is given by the following:

$$\frac{P_{gas.GDL}}{R \cdot T_{st}} = c_{gas.GDL} \tag{3.9}$$

where $c_{gas.GDL}$ is the concentration of the particular gaseous component in the GDLs.

We introduced the concept of the saturation factor S_{GDL} to consider the liquid water content and its effect on gas transportation. Here, the saturation factor is defined as the ratio of the volume of the liquid water to the volume of the GDLs.

$$S_{GDL} = \frac{V_{l.GDL}}{V_{GDL}} \tag{3.10}$$

where $V_{l.GDL}$ is the volume of the liquid water in the GDLs, and V_{GDL} is the volume of the GDLs. The saturation factor affects the diffusion coefficient of the gases.

$$D_V \cdot \varepsilon \cdot \left(\frac{\varepsilon - 0.11}{1 - 0.11}\right)^{0.785} (1 - S_{GDL}) = \langle D_{V.GDL} \rangle \tag{3.11}$$

where D_V is the intrinsic diffusivity of the water vapor, ε is the porosity of 0.3, and $D_{V.GDL}$ is the effective diffusivity, 34.5×10^{-6} m^2/s, of the water vapor in the GDLs. The partial pressure of the vapor in the GDLs is calculated by

considering the balance among the amount of vapor generated inside the GDLs, the amount that entered them, and the amount that exited them.

$$\frac{d}{dt}P_{V.GDL} = R \cdot T_{st}\left(\frac{N_{V.gen} + N_{V.memb} - N_{V.GDL}}{\delta_{GDL}} + R_{evap.GDL}\right) \tag{3.12}$$

where $N_{V.gen}$, $N_{V.memb}$, and $N_{V.GDL}$ are respectively the mole fluxes of the vapor produced by the reactants, the vapor across the membrane, and the vapor transferred between the channels and the GDLs; and $R_{evap.ca}$ is the evaporation mass flow rate in the GDLs. δ_{GDL} is thickness of GDL.

$$r\frac{P_{sat}(T_{st}) - P_{V.GDL}}{R \cdot T_{st}} = R_{evap.GDL} \tag{3.13}$$

The mass transport in the anode GDLs is similar to that in the cathode GDLs, with the exception that there is no nitrogen in the former.

Regarding the mass transport of liquid water in the GDLs, the mass flow rate of water from the GDLs to the channel is given by the following:

$$\rho\frac{A_{fc} \cdot \mu \cdot \mu_{rl}}{\eta_l}\left|\frac{d\rho_c}{ds}\right| \cdot \frac{S_{GDL}}{\delta_{GDL}} = \dot{m}_{l.GDL2ch} \tag{3.14}$$

where μ is the intrinsic permeability of the liquid water; $\mu_{rl.ca}$ is the relative permeability, which is proportional to the cube of the saturation factor [31]; η_l is the viscosity of the liquid water; δ_{GDL} is the thickness of the GDLs; and ρ_c is the capillary pressure, which is calculated by the Leverette *J* function. The volume change of the liquid water in the GDLs is given by the following equation:

$$\rho_l\frac{d}{dt}V_{l.GDL} = -\dot{m}_{l.GDL2ch} - R_{evap.GDL} \cdot M_V \cdot \varepsilon \cdot V_{GDL} \tag{3.15}$$

All the governing equations of the anode GDLs regarding the liquid water are

the same as those of the cathode GDLs.

The major function in the MEA is the movement of protons through the membrane, which is mostly affected by the amount of liquid water and the concentration of reactant near the membrane. In modeling an MEA, most of previous studies adopted simplified electrochemical equation with limited number of parameters. Especially, the simplified equations regarding activation loss are widely used, where a semi-empirical formula is developed to express activation loss as a function of current density and concentration of reactants. Others applied even simpler empirical equations or adopted equivalent circuit sub-model by using the concept of the limit current density. [62] However, these simplified expressions are inappropriate for us to predict the accurate transient behavior, and thus, we decide to introduce kinetic equation at the electrode with minimum simplification to fully understand the behavior of fuel cell.

We used the same equations of the water content, diffusion coefficient, and conductivity presented in the reference. [24] The reversible voltage of the fuel cell was eventually obtained as

$$E_{nernst} = 1.229 - 0.85\times10^{-3}\left(T_{fc} - 298.15\right) + 2.1542\times10^{-5}\cdot T_{fc}\left(2\ln P_{H_2} + 0.5\ln P_{O_2}\right) \tag{3.16}$$

The ohmic resistance and activation loss are respectively given by [33]

$$R_{ohm} = \frac{\delta_{MEA}}{\sigma_m} \tag{3.17}$$

and

$$V_{act} = \frac{R \cdot T_{fc}}{\alpha_c \cdot F} \cdot \ln\left[\frac{j \cdot c_{ref}^{O_2}}{(1-s_{ca}) a_{i_0}^{ref}} \cdot \frac{1}{c_{ch}^{O_2} - \frac{j}{4F}\left(\frac{\delta_{GDL}}{D^{O_2}\left[\varepsilon(1-s_{ca})\right]^{1.5}} + \frac{1}{h_m} \right)} \right] \tag{3.18}$$

where α_c is the transfer coefficient of the electrode, $c_{ref}^{O_2}$ is the reference molar concentration of oxygen, $a_{i_0}^{ref}$ is the product of the transfer current density and the active area, and h_m is the mass transfer coefficient in the GDLs. By summing up all the factors, the output voltage of the fuel cell is obtained as

$$V_{cell} = E_{nernst} - V_{act} - V_{ohm} \tag{3.19}$$

We inputted the same initial condition for all the operation modes to maintain a low current density of 0.2 A/cm^2. Only after the steady state condition was achieved, we experimented various operation modes as mentioned above.

Air providing system

Air providing system (APS) consists of blower, membrane humidifier, and back pressure control valve. Through the system, we can supply humid air to stack. The trend of research for blower is presented in Table 3.1 [63-65]. Most of blower models use empirical relations to show its performance based on experimental data. Thus, we decide to conduct blower model using curve fitting method suggested by Jensen and Kristensen which is the most accurate method to show relationship between mass flow rate and pressure ratio according to RPM [63]. The model uses the dimensionless head parameter, Ψ, to find pressure ratio shown as follow.

$$\Psi = C_p T_{in} [(\frac{P_{out}}{P_{in}})^{\frac{\gamma-1}{\gamma}} - 1] / (\frac{U_b^2}{2}) \tag{3.20}$$

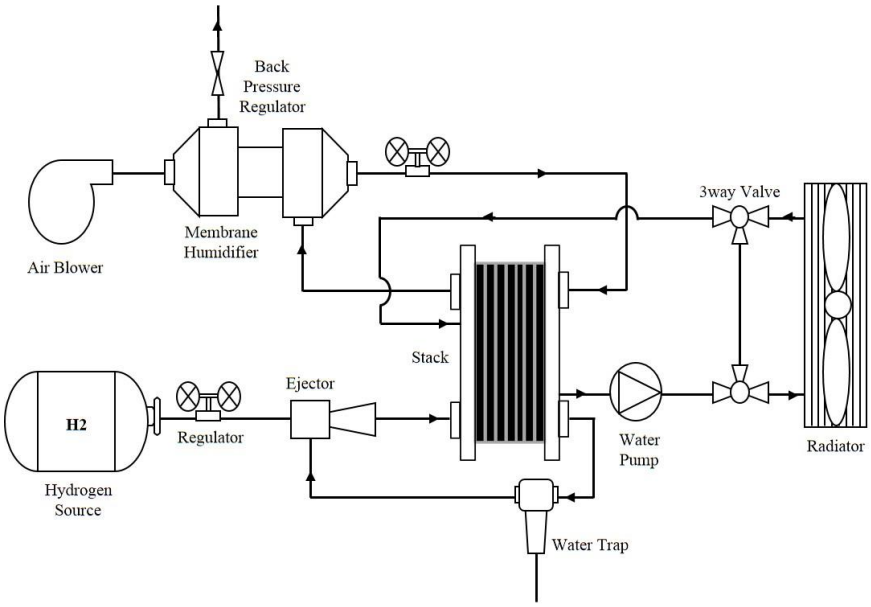

Fig. 3.1 Schematic diagram of fuel cell vehicle.

Table 3.1 An example of features of some literature for blower models in the literatures

Models	Years	Method
Semi-empirical approach		
Paul Moraal et al.	1999	Jensen and Kristensen with curve fitting method
R. Cabello et al.	2005	Physical equation with empirical correlation
E. Navarro et al.	2007	Monte Carlo method by statistical procedure
R. Tirnovan et al.	2008	Moving least square algorithm
Liang Yang et al.	2009	Neural network loss-efficiency model
R. Damle et al.	2011	Modular numerical simulation
Wenhua Li	2012	Thermodynamic principle with semi-empirical method
Jian Hu et al.	2014	Conservative equation with network model

Here, C_p is specific heat of air, γ is specific heat ratio, and U_b is blade tip speed. T_{in} is inlet temperature of blower, and P_{in}, P_{out} is inlet and outlet pressure of blower, respectively. U_b is expressed as function of d_b and N_s, which are diameter of blower and rotational speed, respectively.

$$U_b = \frac{\pi}{60} d_b N_s \tag{3.21}$$

Mass flow rate of blower is determined using normalized blower flow rate shown as follow.

$$\phi = \frac{W_b}{\rho_a \frac{\pi}{4} d_b^2 U_b} \tag{3.22}$$

Here, W_b is output power of blower, and ρ_a is density of gas. There is a relation between Ψ and ϕ expressed as below.

$$\psi = \frac{k_1 + k_2 \phi}{k_3 - \phi} \tag{3.23}$$

$$k_i = k_{i1} + k_{i2} M, \qquad i = 1, 2, 3 \tag{3.24}$$

Here, a coefficient k is obtained through a least square fit on experimental data, and M is inlet Mach number introduced by

$$M = \frac{U_b}{\sqrt{\gamma R T_{in}}} \tag{3.25}$$

Trends for model of membrane humidifier are arranged in Table 3.2 [66-68]. They mainly studied on heat and mass transport through Nafion and explained the mechanism using general conservation equations. Therefore, we just develop our model by examining previous that study on the same type of membrane humidifier. In this paper, we select cylindrical type membrane

Table 3.2 An example of features of some literature for membrane humidifier models in the literatures

Models	Years	Method
Theoretical approach		
Dongmei Chen et al.	2005	Thermodynamic equation with dynamic control
P. Cave et al.	2008	Simple approximation form with straight single channel
M. Sabharwal et al.	2012	Conservative equation in two dimension
D. Bhatia et al.	2013	Conservative equation for shell-and-tube type
Semi-empirical approach		
S. Park et al.	2009	Thermodynamic equation with empirical correlation
S. Yu et al.	2011	Thermodynamic equation with statistical model

humidifier for the system which is the same as PEM fuel cell vehicle. In the membrane humidifier, gas is the only phase that can transfer through the membrane, and we prepared liquid-water separator before the membrane humidifier to meet this assumption. General conservation law for mass transfer is shown as bellow.

$$\sum_i \frac{dm_{i,out}}{dt} h_{i,out} = \frac{dQ}{dt} + \sum_i \frac{dm_{i,in}}{dt} h_{i,in} + \frac{dm_{tr}}{dt} h_{tr} \tag{3.26}$$

Here, Q is heat transfer across the membrane, h is enthalpy in each side; subscript i means each side of membrane, 1 is dry side, and 2 is wet side. in and out means inlet and outlet of the device, and tr means transfer through the membrane. The amount of mass transport is expressed as follow.

$$\frac{dm_{tr}}{dt} = D_w \frac{C_2 - C_1}{t_m} M_v A_{memb} \tag{3.27}$$

D_w is a diffusion coefficient of water in membrane, C is concentration at each side, M_v is molecular weight of vapor and A_{memb} is effective area for mass transport. The amount of heat transfer is shown as follow.

$$\frac{dQ}{dt} = UA_{memb} \Delta T_{lm} \tag{3.28}$$

Here, U is total heat transfer coefficient, and ΔT_{lm} is log mean temperature difference between wet and dry side.

Another device we have to consider in the APS system is valve which regulates mass flow rate and pressure ratio by changing throttle area. As same as internal combustion engine car, we choose butterfly type for PEMFC car. Considering the role of the valve, main parameters are inlet and outlet pressure

and mass flow rate. Therefore, we developed our model by adjusting the mass flow rate for a lumped system, and calculated pressure ratio using throttle area, mass flow rate, and temperature [44]. The model assumed isentropic flow in valve, and out flow of BCV is introduced as follow.

$$m_{BCV} = \frac{C_d A_{th} P_{out}}{\sqrt{RT_{out}}} \left(\frac{P_{in}}{P_{out}}\right)^{1/\gamma} \left\{ \frac{2\gamma}{\gamma - 1} \left[1 - \left(\frac{P_{in}}{P_{out}} \right)^{\frac{(\gamma-1)}{\gamma}} \right] \right\}^{1/2} \tag{3.29}$$

Here, C_d is discharge coefficient to fit to measured data, and A_{th} is throttle area shown as follow.

$$A_{th} = \frac{\pi D_{th}^{2}}{4} \{ (1 - \frac{\cos\alpha}{\cos\alpha_o}) + \frac{2}{\pi} [\frac{b}{\cos\alpha} (\cos^2\alpha - b^2\cos^2\alpha_o)^{1/2} + \frac{\cos\alpha}{\cos\alpha_o} \sin^{-1}(\frac{b\cos\alpha_o}{\cos\alpha}) - b(1-b^2)^{1/2} - \sin^{-1} b] \} \tag{3.30}$$

Here, D_{th} is diameter of channel of valve, and b is shaft diameter for butterfly type throttle valve. α_o is initial angle of throttle plate and α is actual throttle plate angle.

Fuel providing system

Hydrogen in high pressure tank is supplied to stack anode side using regulator, and unreacted hydrogen of anode outlet flow is recirculated by ejector, so the most critical device that we need to mainly deal with in fuel providing system (FPS) is ejector. Development of modeling for ejector is listed in Table 3.3 [69-71]. Each methodology of ejector modeling is different according to the purpose of each study. Some developed one dimensional models using numerical calculation or empirical relation to investigate the overall characteristics and behavior of ejector. Others use CFD tools to analyze the local flows inside the ejector and get more detailed understanding of ejector

Table 3.3 An example of features of some literature for ejector models in the literatures

Models	Years	Method
Theoretical approach		
E. Middleton et al.	1968	Theoretical model of ejector based on characteristics of compressible fluids with experimental validation
B. J. Huang et al.	1998	1-D theoretical model for ejector at critical mode operation is conducted with validation
D. Sun	1998	Theoretical model for ejector refrigeration cycle is developed
E. Ruslya et al.	2005	CFD work for ejector using finite volume techniques
A. Hemidi et al.	2008	CFD model is developed for a supersonic ejector
A. Khalil et al.	2010	1-D model for ejector using R 14a is developed for various operating conditions
Semi-empirical approach		
P. Rudolf von Rohr et al.	1985	Technical data for the proper design of gas ejectors for applications with helium based on experiment and semi-empirical model
B. J. Huang et al.	1998	Empirical correlations of critical variables for ejector is conducted based on many types of ejectors

behavior. In this study, we decide to use theoretical approach based on one dimensional model validated with empirical data, because the purpose of ejector model is to make up hydrogen recirculation system, so our interest is focused on entrance ratio, temperature, and pressure at ejector outlet with given primary mass flow rate, pressure, and temperature [69-71]. Relation among inlet stagnant pressure, P_p temperature, T_p and the mass flow rate through inlet is expressed as follow.

$$\dot{m}_p = \frac{P_p A_t}{\sqrt{T_p}} \times \sqrt{\frac{\gamma}{R}\left(\frac{2}{\gamma+1}\right)^{(\gamma+1)/(\gamma-1)}} \tag{3.31}$$

Here, A_t is cross sectional area at primary inlet. The gas dynamic relations at the nozzle outlet assumed isentropic process.

$$\left(\frac{A_{po}}{A_t}\right) \approx \frac{1}{M_{po}^2}\left[\frac{2}{\gamma+1}\left(1+\frac{(\gamma-1)}{2}M_{po}^2\right)\right]^{(\gamma+1)/(\gamma-1)} \tag{3.32}$$

$$\frac{P_p}{P_{po}} \approx \left(1+\frac{(\gamma-1)}{2}M_{po}^2\right)^{\gamma/(\gamma-1)} \tag{3.33}$$

Here, A_{po} is cross sectional area, and M_{po} is Mach number, and P_{po} is pressure at nozzle outlet. The entrained mass flow rate at entrained flow inlet is calculated as below.

$$\dot{m}_e = \frac{P_e \times A_{em}}{\sqrt{T_e}}\sqrt{\frac{\gamma}{R}\left(\frac{2}{\gamma+1}\right)^{(\gamma+1)/(\gamma-1)}} \quad \text{(for } M_{em} < 1\text{)}$$

$$\dot{m}_e = \frac{P_e \times A_{em}}{\sqrt{T_e}}\sqrt{\frac{2}{R}\cdot\frac{\gamma}{\gamma-1}\left(\frac{P_m}{P_e}\right)^{\frac{2}{\gamma}}\left(1-\frac{P_m}{P_e}\right)^{(\gamma+1)/(\gamma-1)}} \quad \text{(for choking)}$$

(3.34)

P_e and T_e are pressure and temperature at entrained flow inlet, respectively, and P_m is pressure at mixing chamber. A_{em} is cross sectional area for entrained mass flow rate at mixing area. For the calculation of the area of the primary flow at mixing area, A_{pm}, we introduce the isentropic relation including arbitrary coefficient, ϕ_p, which means loss of the primary flow from nozzle outlet to mixing area which is acquired using experimental data.

$$\frac{A_{pm}}{A_{po}} = \frac{(\phi_p / M_{pm})\left[\frac{2}{(\gamma+1)}\left(1+\frac{(\gamma-1)}{2}M_{pm}^2\right)\right]^{\frac{\gamma+1}{2(\gamma-1)}}}{(1/M_{po})\left[\frac{2}{(\gamma+1)}\left(1+\frac{(\gamma-1)}{2}M_{po}^2\right)\right]^{\frac{\gamma+1}{2(\gamma-1)}}} \tag{3.35}$$

Here, M_{pm} is Mach number of primary flow at mixing area. The geometrical cross-sectional area at mixing area, A_m is the sum of the area for primary and entrained flow.

$$A_m = A_{pm} + A_{em} \tag{3.36}$$

Finally, pressure and temperature at diffuser outlet is calculated using isentropic relations for compressible flow.

$$\frac{P_{ej,out}}{P_{diff,in}} = \left(1+\frac{\gamma-1}{2}M_{diff,in}^2\right)^{\gamma/(\gamma-1)} \tag{3.37}$$

Here, $P_{ej,out}$ is pressure at ejector outlet, $P_{diff,in}$ and $M_{diff,in}$ are pressure and Mach number at diffuser inlet.

Thermal management system

It is important to maintain the proper temperature to increase system efficiency, thermal management system (TMS) is the system for managing heat which is composed of heat exchanger, pump, and fan. Development of heat exchanger is listed in Table 3.4 [72-74]. Most studies adapted generalized heat transfer and friction correlation for louver fin geometry, so we also decided to apply former methods. We selected compact-type heat exchanger as condenser, and the amount of heat transfer is calculated using ε-NTU method [74]. Energy equilibrium for stack is expressed as follow.

$$m_{fc} C_{p,fc} \frac{dT_{stack}}{dt} = \Delta \dot{H}_{an} + \Delta \dot{H}_{ca} + \Delta \dot{H}_{chem} - \dot{Q}_{conv} - \dot{Q}_{TMS} - P_{elec} \tag{3.38}$$

Here, m_{fc} is mass of stack, $C_{p,fc}$ is specific heat of stack, and T_{stack} is temperature of stack. $\Delta \dot{H}_{an}$, $\Delta \dot{H}_{ca}$ is changes of energy flow rate at anode and cathode which are calculated by changes of enthalpy shown as below.

$$\Delta \dot{H}_{an} = \Delta \dot{H}_{H_2} + \Delta \dot{H}_{H_2O,an} \tag{3.39}$$

$$\Delta \dot{H}_{ca} = \Delta \dot{H}_{air} + \Delta \dot{H}_{H_2O,ca} \tag{3.40}$$

$\Delta \dot{H}_{H_2}$, and $\Delta \dot{H}_{air}$ are changes of enthalpy of reactants at anode at cathode, respectively. $\Delta \dot{H}_{H_2O,ca}$, and $\Delta \dot{H}_{H_2O,an}$ are enthalpy change due to the generation of water at each side. For each electrode, the enthalpy changes are expressed as follow.

$$\Delta \dot{H}_{H_2} = \dot{m}_{H_2,in} \Delta h_{H_2,in} - \dot{m}_{H_2,out} \Delta h_{H_2,out} \tag{3.41}$$

$$\Delta \dot{H}_{air} = (\dot{m}_{O_2,in} \Delta h_{O_2,in} + \dot{m}_{N_2,in} \Delta h_{N_2,in}) - (\dot{m}_{O_2,out} \Delta h_{O_2,out} + \dot{m}_{N_2,out} \Delta h_{N_2,out}) \tag{3.42}$$

$$\Delta \dot{H}_{H_2O} = \dot{m}_{H_2O,in} \Delta h_{H_2O,in} - \dot{m}_{H_2O,out} \Delta h_{H_2O,out} \tag{3.43}$$

Here, the changes of mass specific enthalpies are calculated with respect to an ambient state, and specific heats are varied according to temperature which are obtained by REFPROP 8.0.

Table 3.4 An example of features of some literature for heat exchanger models in the literatures

Models	Years	Method
Semi-empirical approach		
W. Lee et al.	1999	A generalized heat transfer and friction correlation for louver fin geometry that complied 49 samples of compact louvered fin-and-tube heat exchanger was reported
C. Wang et al.	1999	A heat transfer and friction correlation for fin-and-tube heat exchanger having plain fin geometry that complied 74 samples was reported
W. Li et al.	2010	Heat transfer and pressure drop correlations for compact heat exchanger with multi-region louver fins is developed
C. Hsieh et al.	2012	A 3-D model investigation into the thermal-hydraulic characteristics of a louver finned-tube heat exchanger is presented

Furthermore, additional enthalpy produced by reaction which can be calculated from the difference between enthalpy of the produced water and that of the reactants.

$$\Delta \dot{H}_{chem} = \dot{m}_{H_2,in}\Delta h_{H_2,in} + \dot{m}_{O_2,in}\Delta h_{O_2,in} - \dot{m}_{H_2O}\Delta h_{H_2O} \tag{3.44}$$

The amount of heat emitted to the surrounding by convection is shown as follow.

$$\dot{Q}_{conv} = h_{amb}A_{tot}(T_{stack} - T_{amb}) \tag{3.45}$$

Here, h_{amb} is a convection coefficient of stack, and A_{tot} is surface area of stack. $\dot{Q}_{TMS}$ is the heat energy removed by TMS which is expressed as follow.

$$\dot{Q}_{TMS} = h_{TMS}A_{TMS}(T_{stack} - T_{cool,in}) \tag{3.46}$$

Here, h_{TMS} is forced convective heat transfer coefficient and A_{TMS} is effective surface area of cooling channel which are obtained from experiment. $T_{cool,in}$ is temperature at coolant inlet. Lastly, electric power generated by the stack is expressed as follow.

$$P_{elec} = I \cdot V_{stack} \tag{3.47}$$

Modeling method for fan and pump are the same as that of blower, because the operating mechanism of blower, pump, and fan is similar; we used Jensen and Kristensen method for fan and pump.

To calculate pressure drop of pipe in TMS, the first thing we have to do is acquiring a friction coefficient of pipe. [75] For straight pipe, the friction coefficient for laminar flow and turbulent flow are expressed as below.

$$f = \frac{64}{\mathrm{Re}_D} \quad \text{(for laminar flow)} \tag{3.48}$$

$$\frac{1}{f^{1/2}} = -2.0\log\left(\frac{\varepsilon / d}{3.7} + \frac{2.51}{\mathrm{Re}_D\, f^{1/2}}\right) \quad \text{(for turbulent flow)} \tag{3.49}$$

Here, Re_D is Reynolds number, ε is toughness of pipe, and d is diameter of pipe. Pressure drop at straight pipe is expressed as follow.

$$h_f = f\,\frac{L}{d}\frac{V^2}{2g} \tag{3.50}$$

$$\Delta P = \rho g h_f \tag{3.51}$$

Here, h_f is head loss, L is length of pipe, and V is velocity of fluid. For curved pipe, pressure drop of pipe is obtained using loss coefficient of turbulence. The loss coefficient of pipe bend at right angle is calculated as follow.

$$K \approx 0.388\alpha\left(\frac{R_{pipe}}{d}\right)^{0.84} \mathrm{Re}_D^{-0.17} \tag{3.52}$$

$$\alpha = 0.95 + 4.42\left(\frac{R_{pipe}}{d}\right)^{-1.96} \tag{3.53}$$

Here, R_{pipe} is curvature of pipe, and the loss coefficient of pipe at other angles, θ, are obtained by below.

$$K \approx 0.000384\alpha\theta^{0.84}\,\mathrm{Re}_D^{\beta} \tag{3.54}$$

$$\alpha \approx \frac{0.48R_{pipe}}{d} \tag{3.55}$$

$$\beta = 10^{-10}\theta^4 - 6^{-8}\theta^3 + 1^{-5}\theta^2 - 1.1^{-3}\theta + 0.2696 \tag{3.56}$$

The pressure drop of curved pipe is calculated as follows.

$$h_f = K\frac{V^2}{2g} \tag{3.57}$$

$$\Delta P = \rho g h_f \tag{3.58}$$

System modeling

The system of PEM fuel cell vehicle consists of four subsystems which is expressed in Fig. 3.2: air providing system, fuel providing system, thermal management system, and stack. Since this study focus on analysis of the system configuration of PEMFC vehicle, it is important for developing model to include above sub systems. Trends of models for air providing system are arranged in Table 3.5 [76-77]. Since they have mainly focused on optimization or control to enhance system performance, expressions of system configuration are cursory. On the contrary, we need to express characteristics of air providing system faithfully, because devices in cathode side have great influence on the system performance. The first thing we have to consider is blower which regulates stoichiometric number and pressure; we can calculate mass flow rate and outlet pressure from the blower model. Then, we analyze relationship between membrane humidifier and stack. Since humidity at stack inlet can be calculated based on the humidity of exhaust gas of stack, the sequence of stack and membrane humidifier remain unclear. We decide to apply iterative method to show interaction between these two devices, so each model calculated at least twice to calculate inlet humidity of stack. Lastly, interaction between blower and BCV is included to convince system pressure in cathode. We can obtain the proper pressure distribution at cathode by comparing pressure at blower outlet, pressure drop in membrane humidifier and stack, and inlet pressure at BCV.

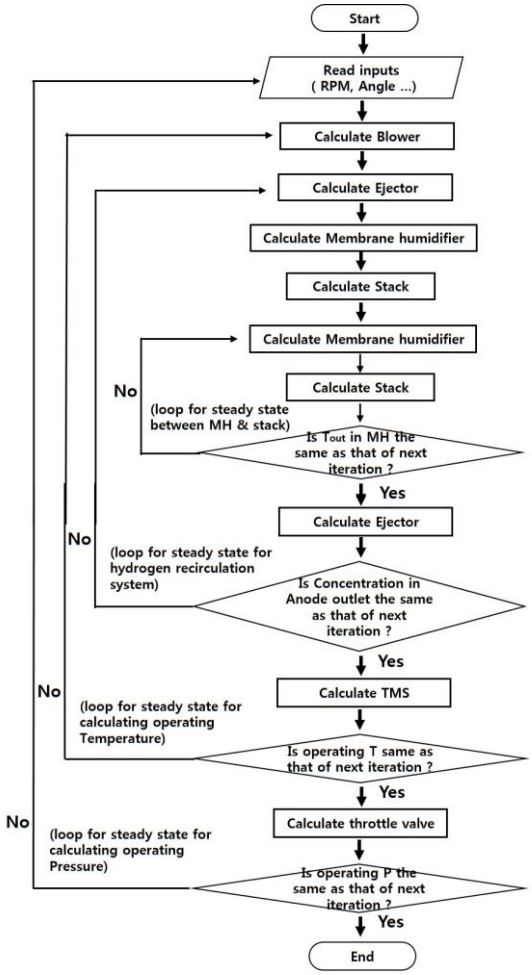

Fig. 3.2 Flow chart for PEM fuel cell system.

Table 3.5 An example of features of some literature for Air providing System models in the literatures

Models	Years	Method
Theoretical approach		
X. Li et al.	2006	Non-linear predictive control algorithm based on least square support vector machine model
C. Li et al.	2008	Hammerstein model with simple and linear point
Semi-empirical approach		
K. Chang et al.	2009	Taguchi method and a generic numerical model
A. W. Dabbagh et al.	2010	Adopted mathematical model with empirical equations
C. Dai et al.	2011	Seeker optimization algorithm using empirical gradient
R. Tirnovan et al.	2012	Mixed method based on moving least squares technique and a semi-empirical analytical model
A. Askarzadeh	2013	Bird matching optimizer algorithm with empirical values
W. Gong et al.	2014	RANK-made approach for optimization

Fuel providing system models have been developed for analyzing or validating performance of PEM fuel cell system which are listed in Table 3.6 [78-79]. In anode side, the most significant feature to consider is hydrogen recirculation. By calculating ejector model twice in front of and behind the stack model, stoichiometric number and pressure at anode are determined.

The models of TMS have developed for various purpose, which are listed in Table 3.7; some developed model for TMS to analyze performance of system, others used the model to know heat and mass transport in the system, and the others conducted control-oriented-model to know efficient driving [80-81]. In the case of TMS for vehicle, we should take into account distribution of mass flow rate for engine cooling and air conditioning, and we can achieve proper control by using fan and three way valve (3WV). Considering above factors, flow chart of TMS is expressed in Fig. 3.3; we can obtain proper results comparing with pressure drop at each devices.

Validation

The validations of devices consisting the PEMFC vehicle are necessary to convince their reliability so, we validated important devices, such as blower, BCV, ejector, and pump which are shown in Fig. 3.4; blower and BCV regulates mass flow rate and pressure at cathode, ejector play an important role in recirculating hydrogen, and pump controls mass flow rate of coolant in TMS. The range of error of blower is 0.1% ~ 2.9%, and that of BCV show constant error of around 7.8%. And the error of ejector is below 4.3 % and that of pump is around 2.7%. Through the model validation, we can convince the accuracy of each device consisting fuel cell system.

Table 3.6 An example of features of some literature for fuel recirculation system models in the literatures

Models	Years	Method
Theoretical approach		
F. Marsano et al.	2003	Theoretical model for SOFC anodic recirculation system is developed to evaluate design and off-design performance based on conservation laws
Y. Zhua et al.	2008	1-D theoretical model for monitoring performance and fault detection of the hybrid SOFC system using ejector
Semi-empirical approach		
C. Baoa et al.	2006	Control-oriented dynamic model of air stream, hydrogen recirculation in a PEM fuel cell system is built based on semi-empirical correlation
F. Barbiri et al.	2006	Empirical correlations for fuel cell stack to validate electrochemical hydrogen pump for recirculation of hydrogen
M. Badami et al.	2009	A theoretical model of a regenerative blower used for the hydrogen recirculation of a PEM fuel cell
M. Uno et al.	2010	A model for the pressure swing recirculation system using two check valves is developed with experimental validation

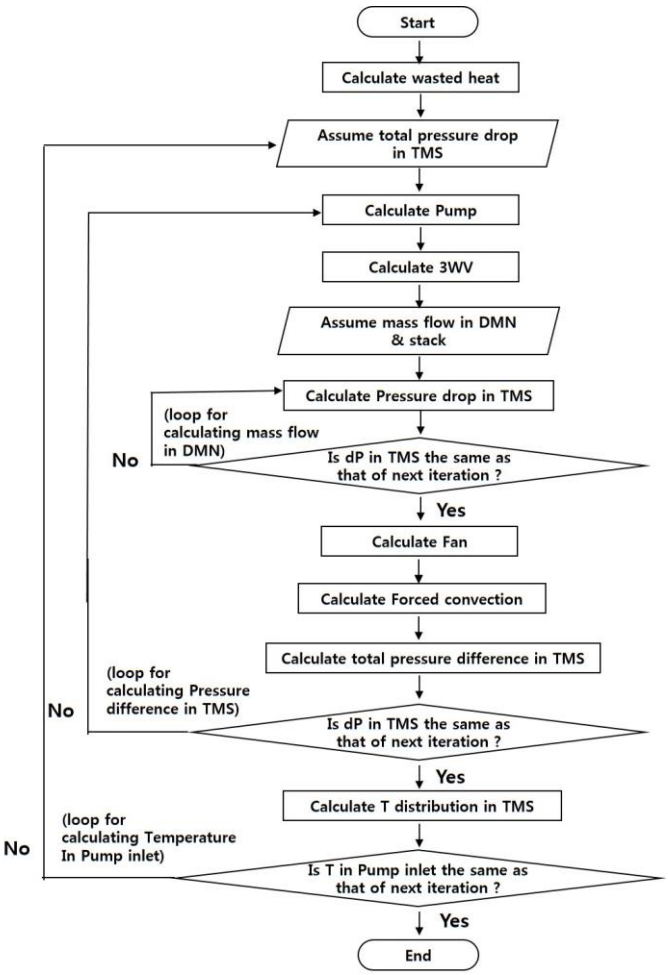

Fig. 3.3 Flow chart for thermal management system.

The main purpose of the analysis on the steady state operation is to understand the performance differences in the low and high current density regions for different operating pressures. Figs. 3.5 (a) and (b) show the difference between the output voltages for several pressures determined by experiment and simulation. It can be observed that the voltages for various pressures are similar in the low current density region, on the other hand, higher voltage differences are generated at higher pressures in the high current density. It is therefore only meaningful to increase the operating pressure in the high current density region to achieve higher output voltage.

Figs. 3.6 and 3.7 show the variations of the oxygen concentration near the membrane and saturation factor in the cathode side, respectively, as calculated in the dynamic model. These were the two major parameters that led to the difference between the performances in the low and high current density regions. Here, the saturation factor is defined as the ratio of the volume of the liquid water in the voids of the GDLs to the volume of the GDLs, which represents the amount of liquid water remaining in the GDL. In the low current density region, the concentration of oxygen and the saturation factor remain nearly constant with increasing pressure, but increase in the high current density region. In the case of the oxygen concentration, the partial pressure of the gas increases with operating pressures, and thus the oxygen concentration near the membrane also increases, resulting in lower activation loss from the fuel cell. It is noted that the oxygen concentrations at 1.0 and 1.3 bar remain relatively low in the high current density region, resulting in reduced performance of the cell.

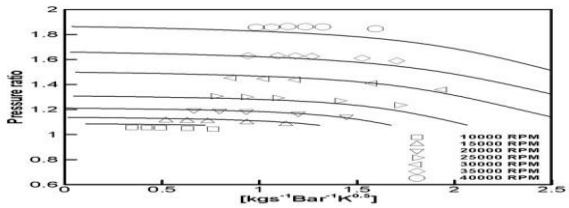

(a) Validation for blower

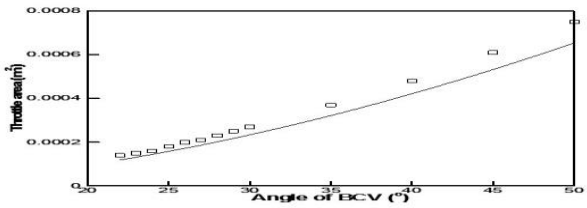

(b) Validation for backpressure control valve

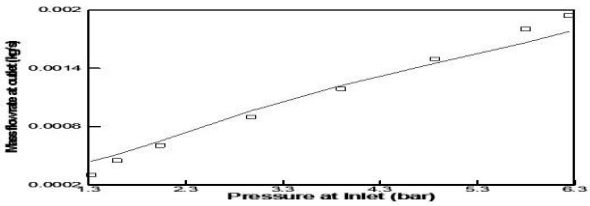

(c) Validation for ejector

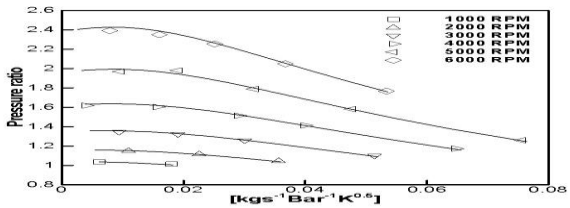

(d) Validation for pump

Fig. 3.4 Validation for devices in each sub parts.

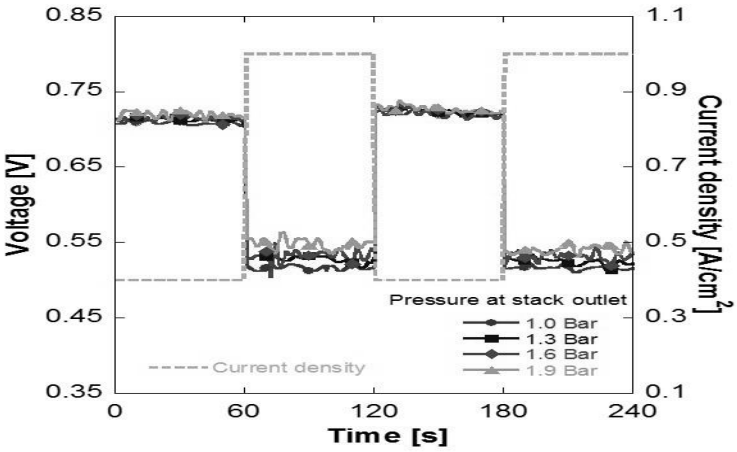

(a) Experiment

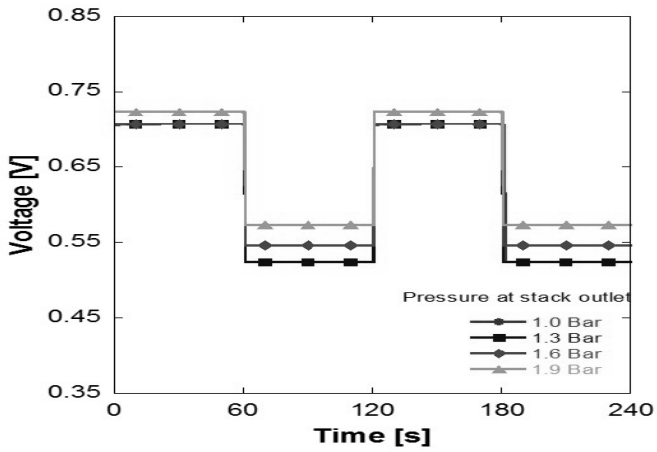

(b) Model

Fig. 3.5 Voltage changes in steady state operation at different pressure.

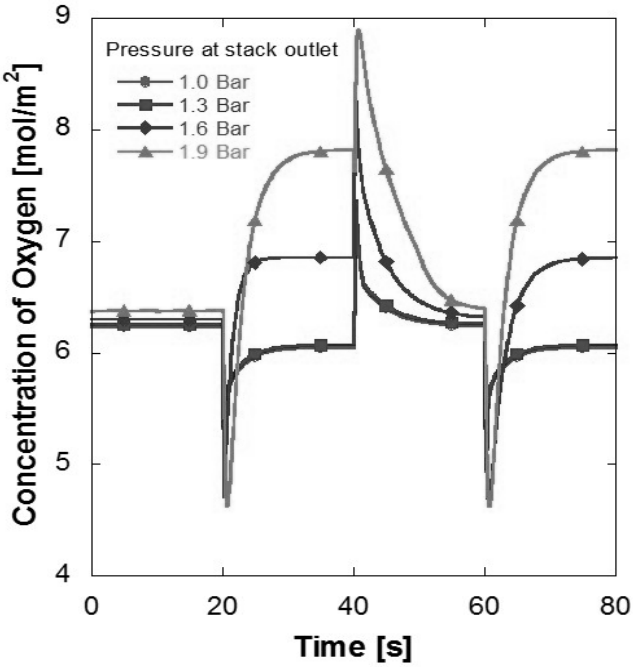

Fig. 3.6 Changes in oxygen concentration near membrane determined by model.

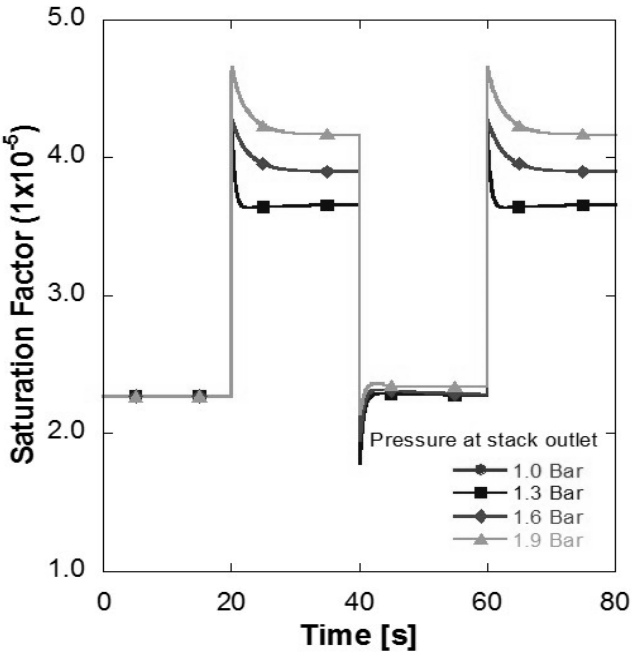

Fig. 3.7 Changes in saturation factor at different pressure determined by model.

On the other hand, the saturation factor increases with increasing pressure, primarily because of the increased partial pressure of the water vapor in the GDLs. In our calculation, by comparing the saturation pressure with the partial pressure of the vapor in the GDLs, the water condensation rate is determined. Therefore, as the pressure increases, more liquid water is generated in the GDLs, thereby increasing the saturation factor. The high saturation factor in the GDLs may lead to the increased voltage loss of the cell, mainly due to the reduced diffusivity of the reactant and product species. However, despite the trends of the saturation factor with operating pressures, the resultant output voltages, as shown in Fig. 3.6, imply that the increase in oxygen concentration plays a dominating role in the output voltage than that of the liquid water in GDLs.

3.3 Parametric study for fuel cell car

To predict the performance of PEMFC vehicle, we have to know operating conditions of the system depending on variation of blower and BCV, because these devices regulate operating pressure, stoichiometric number, and relative humidity. In this chapter, we analyze operating characteristics of PEMFC vehicle at velocity of 140km/h depending on RPM of blower, angle of BCV, and current density.

3.3.1 Operating conditions depending on blower and BCV

Fig. 3.8 shows variation of pressure and mass flow rate based on experimental data; RPM is varied from 25000 to 40000, and BCV angle is varied from 25° to 75°. Operating pressure is proportional to RPM of blower. Since large RPM of

blower supply more mass flow rate, the pressure at blower outlet also increase. The changes in pressure of blower outlet by RPM are greater when angle of BCV is small; the changes in pressure is 0.47 bar when BCV angle is 27°, but 0.28 bar when BCV angle is 66°. The results indicated that blower has a great influence on pressure with small angle of BCV. In the case of BCV, pressure is inversely proportional to angle of BCV. Since throttle area of valve is proportional to angle of BCV, operating pressure is inversely proportional to BCV angle. Though small change of pressure by BCV in all operating region, there is marked variation in large RPM region. Therefore, we need to carefully control the BCV in large RPM area. In comparison, the ratio of pressure change by the RPM is greater than that by the BCV angle. It means that RPM of blower is dominant parameter than angle of BCV to control operating pressure. On the other hand, pressure variation at anode follows the variation at cathode. Therefore, pressure at both side always similar in all operating range.

In the case of mass flow rate at cathode, it is proportional to RPM of blower and angle of BCV. It is obvious that mass flow rate increases when RPM is high, and throttle area is large; mass flow rate is maximized at 40000 RPM, and at BCV angle 67°, on the other hand, it is minimized at 25000 RPM and at BCV angle 28°. The variation of mass flow rate by RPM is large when BCV angle is angle. It means that the effect of blower is dominant when the valve open widely. Additionally, changes in mass flow rate by BCV are large at higher RPM which is the same as that of pressure. Through the results, we identified that it had better change angle of BCV at higher RPM region for controlling mass flow rate. These are unique characteristics of PEMFC vehicle.

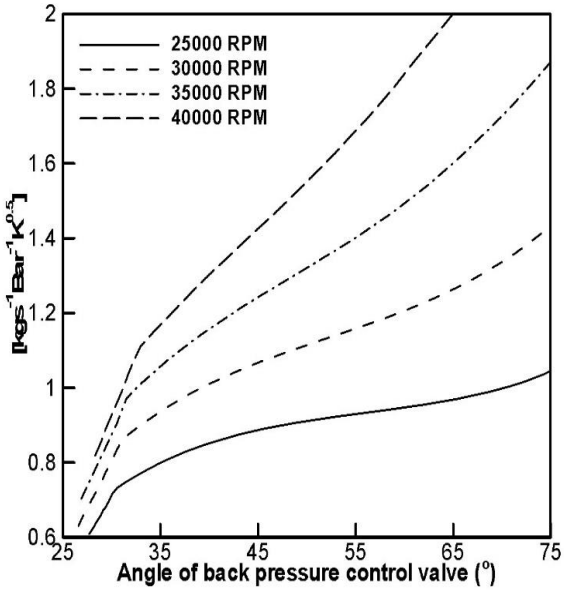

Fig. 3.8 Major parameters which are affected at variable pressure system.

The variations of stoichiometric number depending on RPM of blower and angle of BCV are expressed in Fig. 3.9 at different load conditions. We assumed that current density of 0.6 A/cm^2 stands for light load, 0.8 A/cm^2 for intermediate load, and 1.0 A/cm^2 for heavy load condition. The trend of variation of stoichiometric number is similar to that of mass flow rate. The amount of changes of stoichiometric number by BCV is small in low RPM region and large in high RPM region; it changes 0.46 at 25000 RPM and 3.2 at 40000 RPM. In addition, the amount of changes of stoichiometric number depending on RPM is small in small angle of BCV and vice versa; it changes 0.84 at 27°, and 3.62 at 68°. It is obvious because stoichiometric number is proportional to mass flow rate of blower outlet. In addition, stoichiometric number becomes lower according to increase of current density. The minimum values in all operating regions are similar, but maximum values are 5.84 at light, 4.42 at intermediate, and 3.47 at heavy load condition. This is because the difference between the amounts of supplied and required gas; although the amount of supplied mass flow rate is predetermined by blower and BCV, the amount of required mass flow rate from stack increases according to load conditions. Through this analysis, we can know that meticulous control of blower and BCV is necessary to supply proper stoichiometric number according to load conditions. Meanwhile, the stoichiometric number at anode is determined by control of pressure inlet of ejector. The value stayed around 1.5 in all operating region.

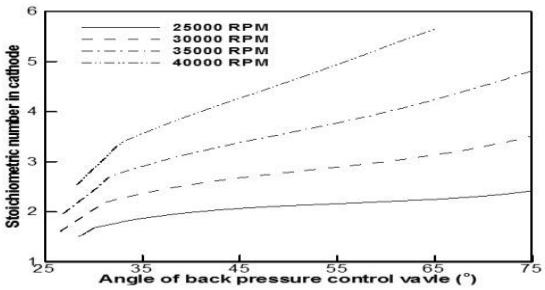

(a) Light load condition

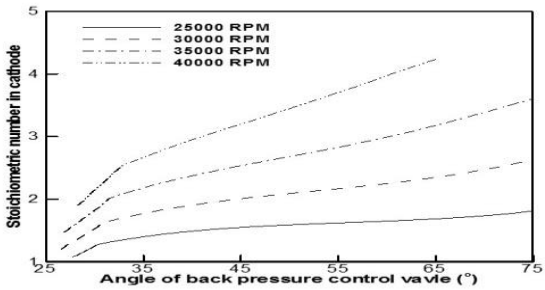

(b) Intermediate load condition

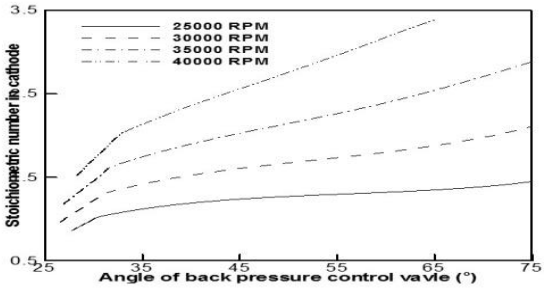

(c) Heavy load condition

Fig. 3.9 The variation of stoichiometric number depending on load conditions.

The variation of relative humidity is expressed in Fig. 3.10. Relative humidity becomes lower according to increase of angle of BCV and RPM of blower which is resulted by outlet temperature which becomes higher with pressure increase due to isentropic process inside the blower. The higher temperature at blower outlet goes into the membrane humidifier, and helps to reduce relative humidity at stack inlet. This is why relative humidity decrease according to increase of RPM. In the case of BCV, increase of angle lowers the relative due to the change of mass flow rate. As angle of BCV increases, the amount of mass flow rate of dry air increase while that of moisture is constant. It keeps the humidity down according to increase of angle of BCV. The trends of variation of relative humidity along with different load conditions are similar; relative humidity is low at higher RPM and larger angle of BCV. However, the value of relative humidity becomes higher at higher load condition because large amount of liquid water generation which can help to raise the amount of supplied liquid water in membrane humidifier. The changes of relative humidity are closely related to the performance of stack which are suggested in next section.

3.3.2 System performance

To identify the changes of the system output and power consumption according to various operating conditions, we analyze performance of stack, BOPs, and system depending on blower, BCV, and load conditions.

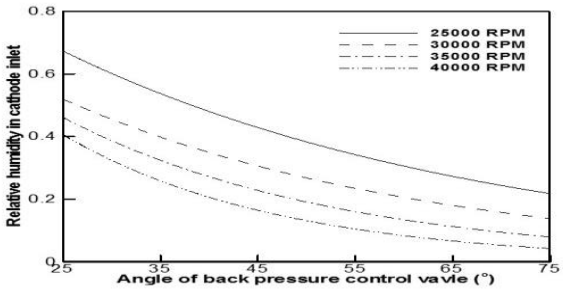

(a) Light load condition

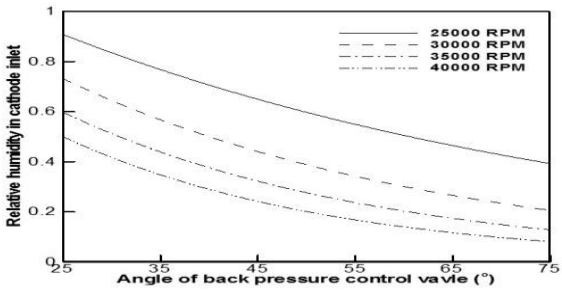

(b) Intermediate load condition

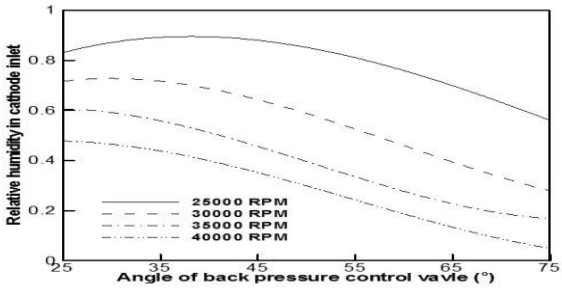

(c) Heavy load condition

Fig. 3.10 The variation of relative humidity depending on load conditions.

Through Fig. 3.11, we can know the results of power generation of stack for PEMFC vehicle. As expected, stack power increases according to increase of current density; the highest power of stack is 58.4 kW at light load, 73.6 kW at intermediate load, and 91.2 kW at heavy load condition. The maximum power can be observed at high RPM of blower, and low angle of BCV. At light load condition, distribution of stack power is similar to that of pressure, so we can find that the influence of pressure is dominant at light load condition. While increasing current density, the performance is not simply proportional to pressure change; the lowest power generation is found at low BCV, and higher RPM does not represent higher power at higher angle of BCV. This changes are mainly resulted from variation of stoichiometric number and relative humidity. At lowest angle of BCV, power generation of stack is low because relative humidity remain high, but stoichiometric number is low. As angle increase, the former one become reduced, but latter one become increased as mentioned at previous section. As a result, power generation increase at early stage, but sooner it decrease. Moreover, the performance of stack at lower RPM becomes higher than that at high RPM at region of large angle of BCV. This is resulted from complex interaction between pressure, stoichiometric number, and relative humidity; when we enlarge the throttle area, average pressure at stack decrease, so operating pressure at region of larger angle does not have greatly influence on the performance of stack. Whereas relative humidity in this region is extremely low for supplying humidity at stack which can deteriorates performance of stack in higher RPM region.

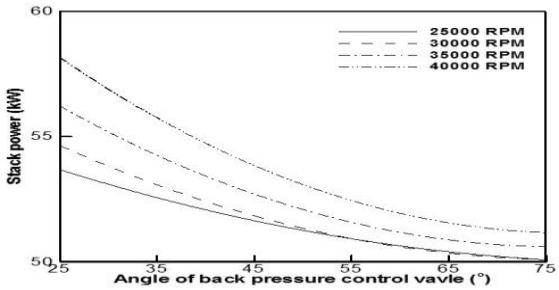

(a) Light load condition

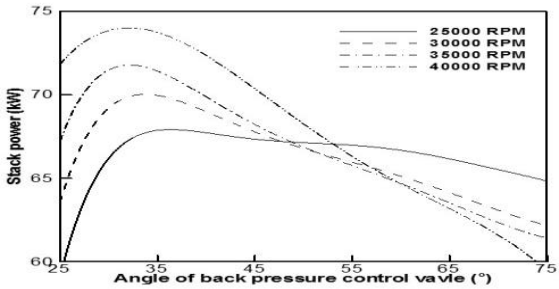

(b) Intermediate load condition

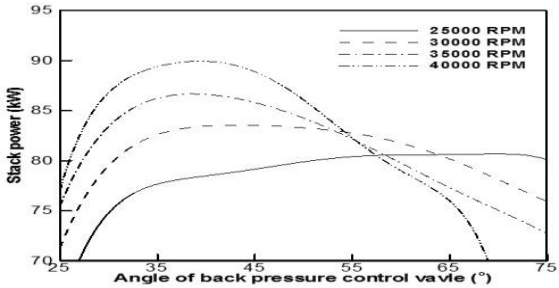

(c) Heavy load condition

Fig. 3.11 The variation of power generation from stack depending on load conditions.

At heavy load condition, performance gradually increases at 25000 RPM. In this region, pressure and stoichiometric number remain unchanged, however, relative humidity keep large in all region. As a results, higher performance can be achieved at most operating angle regions. Furthermore, the difference of performance depending on RPM is large at opposite ends of angle of BCV; about 13 kW of performance difference is observed at both ends of angle, while about 3 kW of difference is shown at middle section. In the case of effect of BCV, the difference of performance is about 10 kW at 25000 RPM, and 17 kW at 40000 RPM. Through this results, we can find that performance can be greatly influenced by RPM and BCV, both. Based on above results, we can conclude that the effect of load condition, i.e., current density, have more influence on performance than BCV and RPM.

Power consumption from BOPs is expressed in Fig. 3.12 depending on load conditions. Among the BOPs, blower consumes the most power, and then fan, and pump are followed. In the case of effect of load conditions, the differences according to loads are negligible because of induced wind from a vehicle; heat from the stack can be fully cooled down by large amount of wind induced by vehicle whose velocity is 140 km/h. Considering relationship above results, performance of PEMFC system is expressed in Fig. 3.13. The variations of the system power are similar to that of stack, however, some differences are observed according to load conditions. In light load condition, maximum power, 52.1 kW, can be obtained at 40000 RPM and 25°, and system power gradually decrease along with increase of angle of BCV.

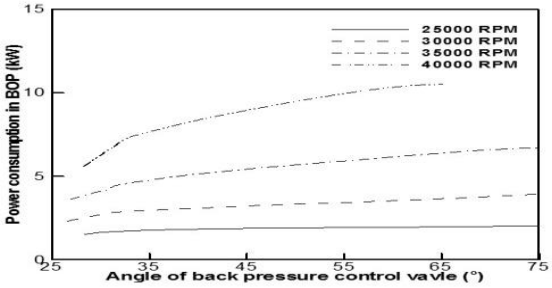

(a) Light load condition

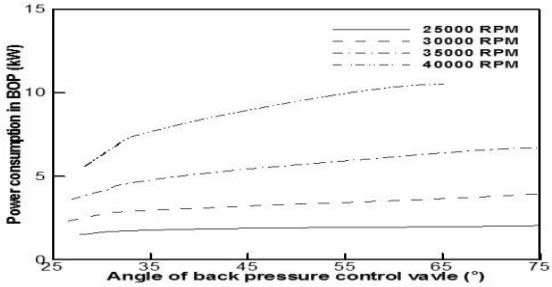

(b) Intermediate load condition

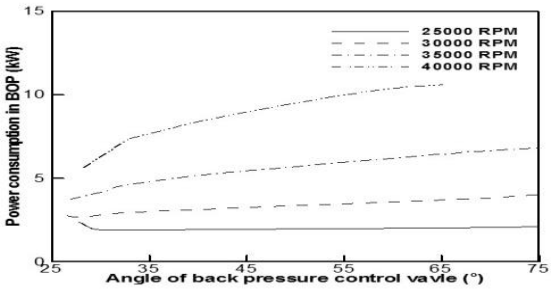

(c) Heavy load condition

Fig. 3.12 The variation of power consumption from auxiliaries depending on load conditions.

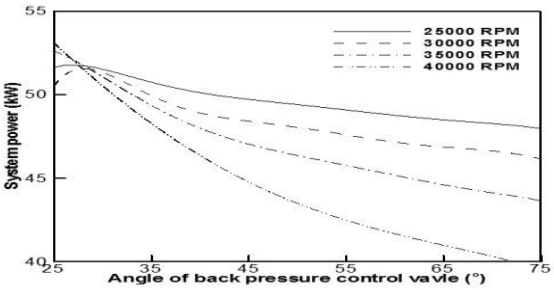

(a) Light load condition

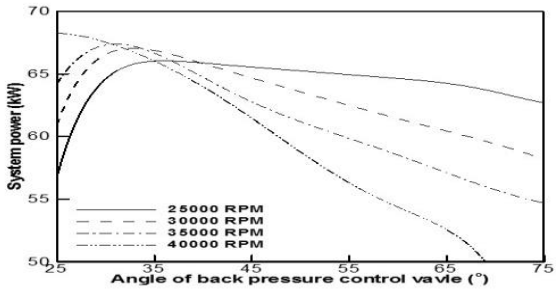

(b) Intermediate load condition

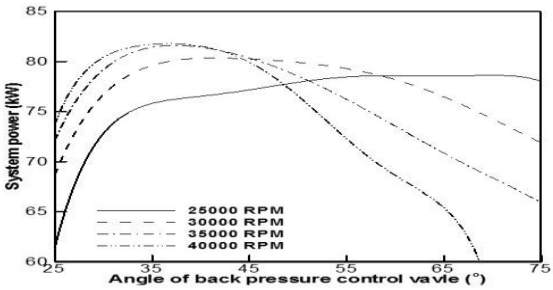

(c) Heavy load condition

Fig. 3.13 The variation of system power depending on load conditions.

Moreover, the differences of performance depending on RPM are small at region of smaller angle of BCV. Since power consumption by BOPs offset gaining of power generation. As angle of BCV increase, the difference of system performance grows, and system output at lower RPM is greater than that at higher RPM. Large amount of power consumption by BOPs degrades of performance of system though increase of power generation from stack. On the other hand, there are different results are shown at heavy load condition; system power drastically increase at first, then, decrease except the power at 25000 RPM which are similar to the variation of stack. The maximum power is about 82 kW at 40000 RPM, but minimum power is also found at 40000 RPM; it is because when the angle is small, the amount of enhanced power of stack is large, but reduced power by BOPs is small, and vice versa when the angle is large. It means that controlling angle of BCV is important at high RPM and high current density region. Furthermore, the difference of power becomes large at larger angle of BCV area, at heavy load condition. This variations are resulted from the interaction between the power generation of stack and that of consumption from BOPs at higher angle of BCV. Based on above results, we can find that we have to control blower and BCV carefully at higher current density region. In addition, higher power is obtained at lower RPM of blower in most operating area.

At last, we investigate the variation of system efficiency which is defined as ratio of net power over higher heating value of hydrogen in Fig. 3.14. As the same as that of system power, the efficiency becomes higher toward higher current density region. The amount of power consumption by BOPs is similar

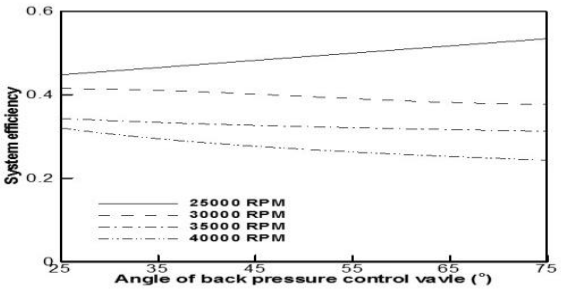

(a) Light load condition

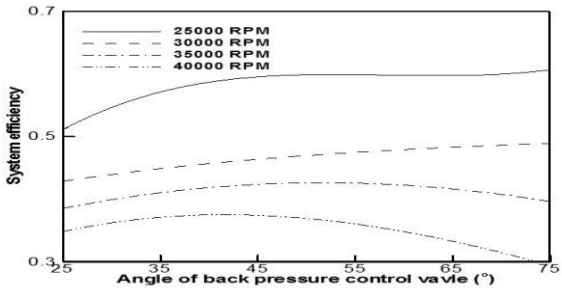

(b) Intermediate load condition

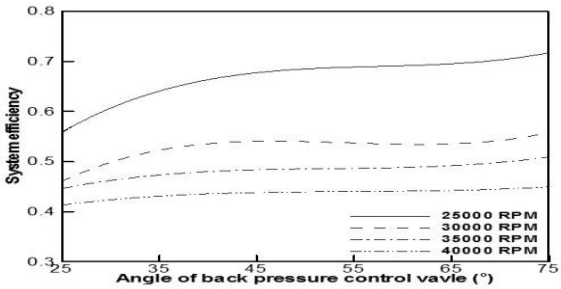

(c) Heavy load condition

Fig. 3.14 The variation of efficiency depending on load conditions.

in all load condition, whereas power generation of stack becomes larger at heavy load condition. Therefore, the higher the current density is, the higher the system efficiency is. Additionally, we can find that the effect of BCV is small, and that of blower is large; at light load condition, the difference by BCV is up to 7%, but that by blower is 27%. To sum up, the efficiency is higher toward lower RPM, and differences depending on RPM are larger toward higher current density region.

3.4 Performance curve for PEMFC vehicle

We suggest the performance curves which contain performance and efficiency of system depending on RPM of blower and angle of BCV. Through these graphs, we can predict the actual performance of PEM fuel cell vehicle.

The performance and efficiency at 60 km/h are expressed in Fig. 3.15. The lowest power output is found at higher level of RPM of blower and higher angle of BCV at every operations, however, the highest power output is found at higher RPM, but lower level of the angle of BCV as same as the former analysis. On the other hand, the effect of RPM on system performance varies depending on the current density. The RPM generating maximum system power is proportional to the current density; the maximum power is observed at 25000 RPM at 0.6 A/cm^2, 36000 RPM at 0.8 A/cm^2, and 40000 RPM at 1.0 A/cm^2, is 52.4 kW, 68.7, and 80.9 kW, respectively. It means that desirable RPM is different depending on load condition; the higher the RPM is, the higher the system power will be. The performance curves for 100 km/h and 140 km/h are illustrated in Fig. 3.16 and 3.17, respectively. Overall variations are the same

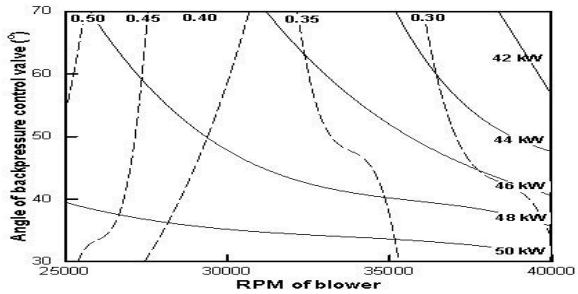

(a) Light load condition

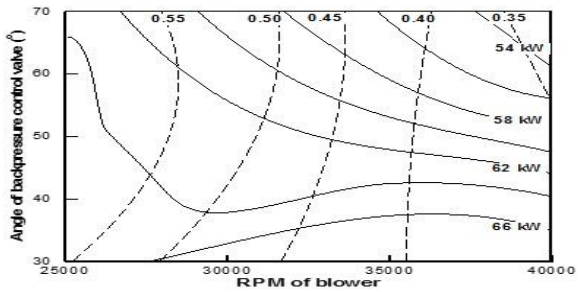

(b) Intermediate load condition

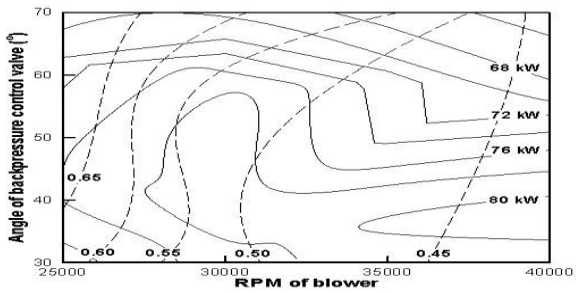

(c) Heavy load condition

Fig. 3.15 Performance curve of PEMFC vehicle at 60 km/h.

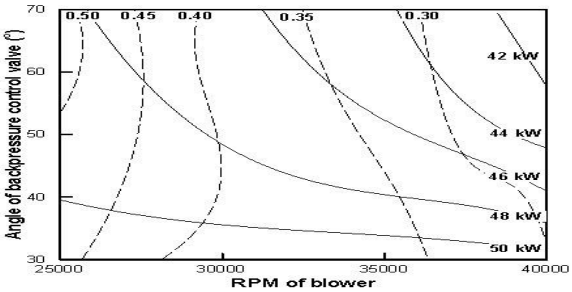

(a) Light load condition

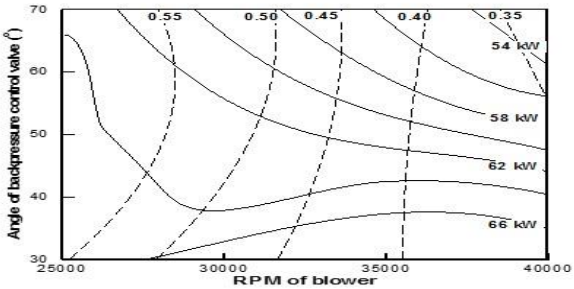

(b) Intermediate load condition

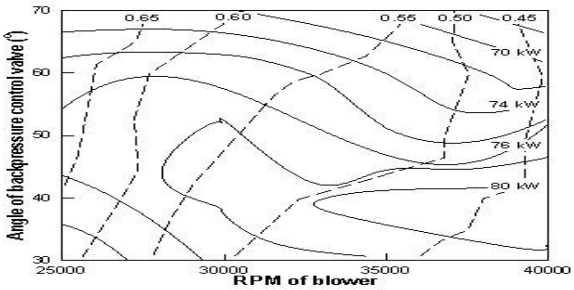

(c) Heavy load condition

Fig. 3.16 Performance curve of PEMFC vehicle at 100 km/h.

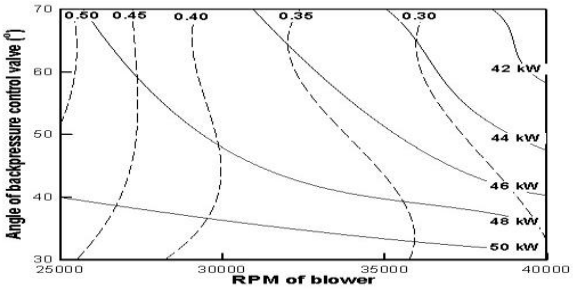

(a) Light load condition

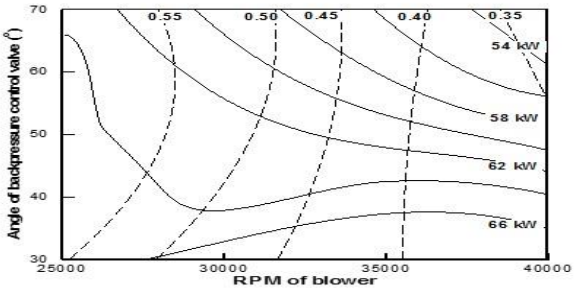

(b) Intermediate load condition

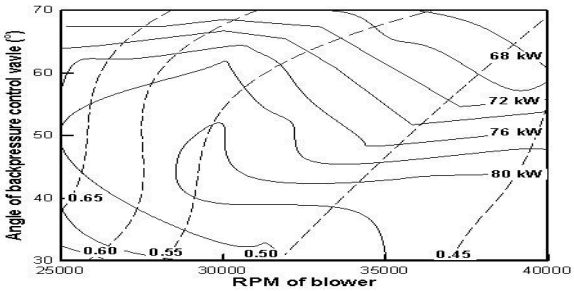

(c) Heavy load condition

Fig. 3.17 Performance curve of PEMFC vehicle at 140 km/h.

among three figures. Curves for light and intermediate load condition are similar at each velocity; system generates the highest power at small angle of BCV and large RPM of blower. However, the trends are little different at heavy load condition; there is increase of performance at low angle of BCV. In the case of system efficiency, it increases according to increase of current density. Therefore, it is better decrease RPM and maintain angle of BCV at 50° for generating maximum power due to power consumption from blower.

3.5 Summary

In this study, system model for PEM fuel cell vehicle validated with 80 kW-class actual automotive fuel cell is conducted to predict the system performance and show performance curve depending on interaction of blower and backpressure control valve. The important operation parameters in the system are pressure and mass flow rate which are affected by RPM of blower and angle of BCV. At first, operating pressure in cathode side is proportional to RPM of blower, and the effect of BCV on pressure is a little. In the case of mass flow rate in cathode, it is proportional to both RPM of blower and the angle of BCV. Blower and BCV also affect stoichiometric number and relative humidity during the operation. The stoichiometric number is proportional to mass flow rate, and it is inversely reduced as system load is increasing. The relative humidity gradually decreases as the angle of BCV increases. As a result, the power generation of stack is high at high RPM, and low at large angle region. In the case of power consumption, blower and induced wind are the main parameter among the BOPs and it has hardly influence on BCV and load

condition. Considering power generation and consumption, we can know the variation of system power and efficiency.

In the end, we suggest performance curve with various car speed to predict actual performance of PEM fuel cell vehicle. System generates maximum power at the high RPM and the low angle of BCV, as current density increases. For system efficiency, it increases as RPM of blower decreases; the effects of angle of BCV and current density are negligible. It is resulted from the power consumption of blower; it consumes most power of the system among BOPs.

Chapter 4. A study on organic Rankine cycle to recover low grade waste heat

4.1 Introduction

Parametric study of organic Rankine cycle for low-grade heat with temperature below 80°C and small-scale waste heat below 10 kW has been conducted to analyze the effect of operating conditions on the work and efficiency. R245fa was used as a working fluid, and scroll expander was selected as power-generation device. In this study, we present system power and thermal efficiency under various operating conditions, experimentally; evaporating pressure and mass flow rate are main parameters influencing system power and efficiency. Moreover, we show the variation of system performance with the changes in the temperature of heat sink which are varied from 20 to 35°C. This paper suggests performance curve for the cycle in low-temperature and small-scale waste heat environment to show the system power and thermal efficiency. System power and efficiency increase with an elevation of evaporating pressure and mass flow rate, because high pressure ratio between expander inlet and outlet raises torque generation in the expander. However, the system power and efficiency decrease with increase of temperature of heat sink due to the lower pressure ratio which is resulted from higher condensing temperature. The power and efficiency are proportional to the saturated temperature at evaporator and capacity of waste.

4.2 Methodology

The ORC is mainly composed of a pump, evaporator, expander, and condenser as shown in Fig. 4.1. A working fluid is pumped into the evaporator to absorb waste heat and then to turn into superheated gas. The gas drives the expander to generate power with enthalpy drop. Next, the working fluid with lower temperature and pressure enters condenser to discharge heat and returns to the pump to form a cycle. In this study, we selected scroll type expander to generate power for low grade heat, and R245fa as a working fluid because it is environment friendly and efficient to recover low grade waste heat. We conducted experiment to present the measured data and to validate numerical analysis.

Numerical analysis for organic Rankine cycle

In this paper, we developed our system modeling to predict performance of the system based on previous studies [18]. Organic Rankine cycle consists of four processes; compression, heat receiving, expansion, and heat rejection. The relationship between mass flow rate and pressure ratio in the pump is expressed using curve fitting method suggested by Jensen and Kristensen and its power consumption is expressed using empirical equation based on experimental data [63,82]. Since this method is able to express accurate performance map of pump, we adopt this method for pump model.

In case of heat transfer, we selected ε-NTU method to model the plate heat exchangers with counter-flow configuration. The heat exchangers are divided by 3 regions; liquid, two-phase, and gas regions. The heat transfer coefficient

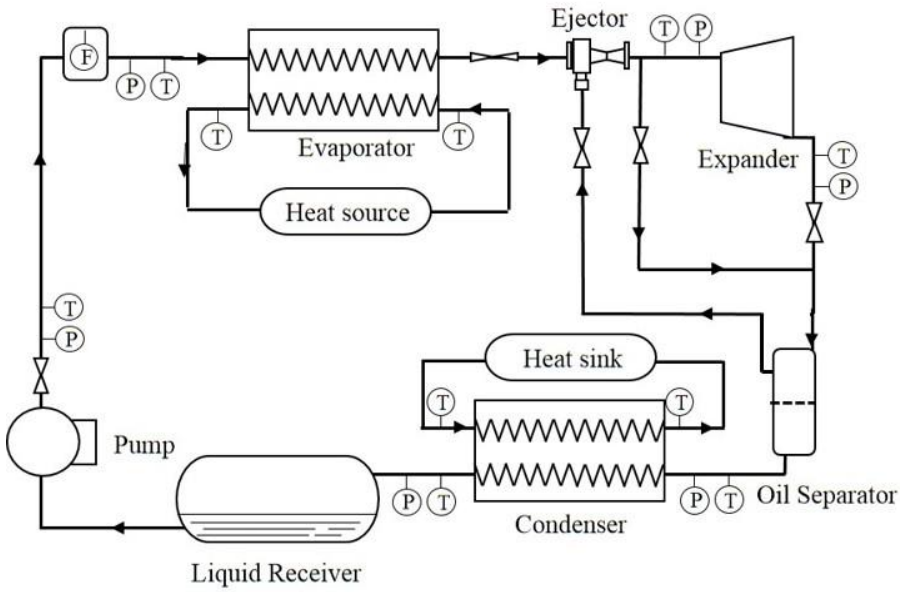

Fig. 4.1 Schematic diagram of organic Rankine cycle system.

U is expressed as follows.

$$\frac{1}{U} = \frac{1}{U_{w.f}} + \frac{1}{U_{s.f}} \tag{4.1}$$

Here, $U_{w.f}$ and $U_{s.f}$ are convective heat transfer coefficients of working fluid and secondary fluid, respectively. Heat transfer coefficients by forced convection are function of non-dimensional relationship shown in Eq. (4.2) [28-30].

$$Nu = C \cdot \mathrm{Re}^m \cdot \mathrm{Pr}^n \tag{4.2}$$

The exponent m is determined based on whether the flow is laminar or turbulent ranging from 0.5 to 0.8. That of n is 1/3, in general [83]. C is identified with experimental data and this coefficients for vapor and liquid phase are 0.82 and 0.7, respectively. To explain boiling heat transfer in the plate heat exchanger, we followed previous assumption of constant heat transfer coefficient during evaporation shown in Eq. (4.3) [84].

$$h_{2p,eva} = C \cdot h_l \cdot Bo^{0.5} \tag{4.3}$$

Here, h_l is single phase (liquid) heat transfer coefficient, and Bo is boiling number. Condensation heat transfer coefficient for plate heat exchanger is expressed as follows [85].

$$h_{2p,cond} = C \cdot (0.25 \cdot Co^{-0.45} \cdot Fr_l^{0.25} + 75 \cdot Bo^{0.75}) \tag{4.4}$$

Co is convection number and Fr_l is Froude number of saturated liquid. Operation of scroll expander is described by semi-empirical model [86]. In this model, we fictitiously express the heat transfer, the supply pressure drop, and the internal leakage occurring in actual expansion process. Supply pressure drop is associated with the geometry of suction chamber which is expressed as

an isentropic flow through a nozzle which is shown as follows [87].

$$\dot{m} = \frac{\sqrt{2C_p}}{R} \frac{P_{in}}{\sqrt{T_{in}}} A_{suc} \left(\frac{P_{suc}}{P_{in}} \right)^{\frac{1}{\gamma}} \sqrt{1 - \left(\frac{P_{suc}}{P_{in}} \right)^{\frac{\gamma-1}{\gamma}}} \tag{4.5}$$

Here, C_p is specific heat of working fluid, P_{in} and T_{in} are pressure and temperature at expander inlet, and P_{suc} is outlet pressure. γ is ratio of specific heat and A_{suc} is suction area of expander. To calculated supply heat transfer, we introduced fictitious metal body with temperature of T_w, which represent expander shell and scrolls. The heat transfer occurring in suction process is shown below.

$$\dot{Q}_{su} = \left[1 - e^{\left(\frac{-AU_{suc}}{\dot{m} \cdot C_p} \right)} \right] \cdot \dot{m} \cdot C_p \cdot (T_{suc} - T_w) \tag{4.6}$$

In Eq. (5.6), T_{suc} is temperature of working fluid after suction, and AU_{suc} is the area times heat transfer coefficient associated with suction process which is calculated from the relationship with nominal heat transfer coefficient justified by the Reynold's analogy for turbulent flow [88]. The mass flow rate due to leakage is given by

$$\dot{m}_{leak} = \frac{A_{leak}}{v_{leak}} \sqrt{2(h_{suc} - h_{leak})} \tag{4.7}$$

Here, A_{leak} is cross sectional area of fictitious leakage clearance, and v_{leak} is specific volume at leakage. h_{suc} and h_{leak} are enthalpy after suction and leakage, respectively. Shaft power of expander is expressed as follows.

$$\dot{W}_{sh} = \dot{W}_{in} - 2\pi N_{rot} T_{loss} \tag{4.8}$$

N_{rot} is rotational speed, and T_{loss} represents torque loss generated by friction. $\dot{W}_{in}$ is power obtained by expander which is expressed by mass flow rate and

enthalpy difference during suction and expansion.

$$\dot{W}_{in} = \dot{W}_{suc} + \dot{W}_{expan} + \dot{W}_{dis} = \dot{m}_{in}(h_{suc} - h_{ex}) \tag{4.9}$$

Lastly, system efficiency is defined as.

$$\eta_{sys} = \frac{(\dot{W}_{sh} - \dot{W}_{pump})}{Q_{abs}} \tag{4.10}$$

Here, $\dot{W}_{pump}$ is power consumption by pump, and Q_{abs} is the amount of heat absorbed at evaporator.

Experimental set up for organic Rankine cycle

Experimental setups were designed to investigate the performance for small-scale and low-temperature ORC system working with R245fa. We can analyze the performance of the system by controlling the mass flow rate, evaporating pressure, and temperatures of heat sink.

Using the gear-type pump (T series by Tuthill) with frequency inverter, we can circulate working fluid and adjust mass flow rate. Mass flow rate of working fluid was measured using mass flow meter (Bronkhorst, M5X CORI-FLOW). In addition, we prepared customized liquid receiver to prevent gas entering the pump. To measure accurate power consumption of the pump, we connected digital power meter (YOKOGAWA, WT130) to pump. All heat exchangers used in this study are counter-flow plate heat exchanger; capacity of evaporator and condenser were 15120 kcal/h. Heat source is prepared using thermostat having a capacity of 10 kW and heat sink using a chiller having a capacity of 22680 kcal/h. Moreover, we selected water as a secondary fluid and we controlled its temperature and mass flow rate in order to express various conditions of heat source and sink. For small-scale and low temperature ORC,

(a) Scroll type expander

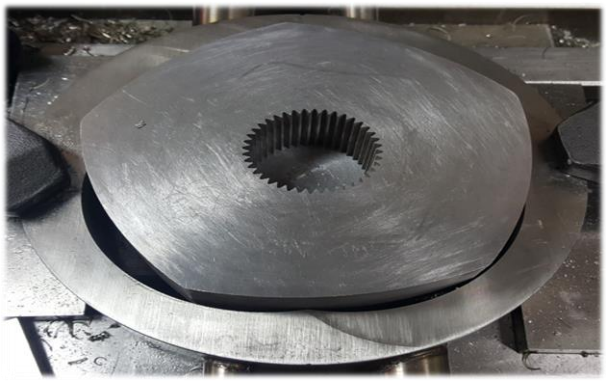

(b) Rotary engine type expander

(c) Rotary vane type expander

Fig. 4.2 Several types of expander using for small-scale organic Rankine system.

scroll expander is quite efficient to generate power due to its relatively low expansion ratio. Therefore, we manufactured scroll expander using a commercial scroll type vapor compressor (Copeland, ZF09K4E-TFD-550) which was shown in Fig. 4.2, and other types of expander that used for ORC. Moreover, we prepared dynamometer which consists of torque transducer (SETech, YDNR-1K), RPM meter (Ono Sokki, MP-981), and hysteresis brake (MAGTROL, AHB-5) to measure generated power. Lubrication of expander was achieved by supplying oil using an ejector (Heatech Korea) and oil separator (Emerson).

Validation

The validation of the model for several main components comprising the ORC system was conducted which are shown in Fig. 4.3. We validated models of pump and expander by comparing relationship between mass flow rate and pressure ratio obtained from model and experiment. In addition, the validation of heat exchanger is conducted by showing errors between the value of calculated UA and experimental data. The models of pump and expander seem nice with average error of under 6%; it is obvious because they are empirical models. However, the error of performance estimation of heat exchanger is estimated under 12%. The error of system model is defined by considering the errors of mass flow rate, work generation, outlet temperature of evaporator, and outlet temperature of condenser. The average error for above parameters is around 6% for various operating ranges. This model is used to supplement experimental data to explain the variation of results.

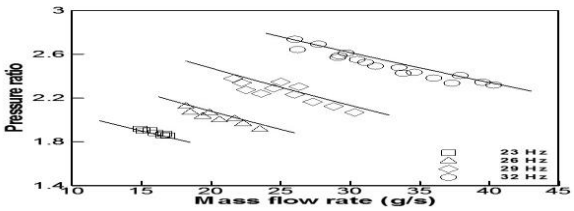

(a) Validation for pump

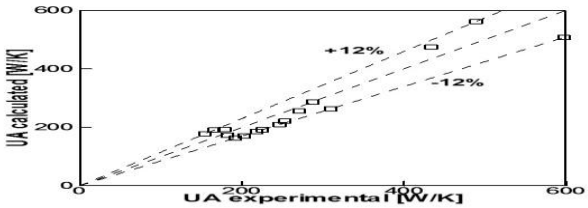

(b) Validation for evaporator

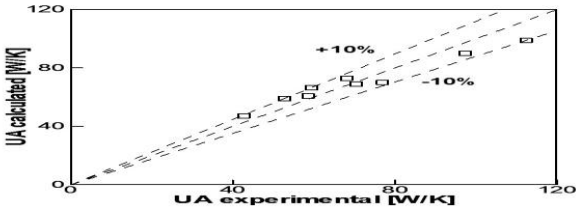

(c) Validation for condenser

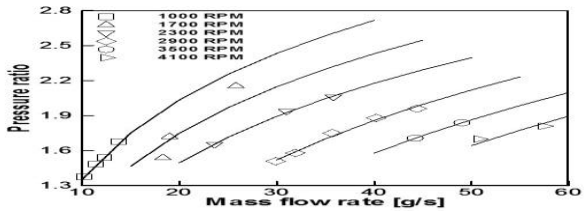

(d) Validation for expander

Fig. 4.3 Model validation.

4.3 Operating characteristics at a given temperature range

Among the parameters, evaporating pressure and mass flow rate are significant factors affecting the system performance; power generation from expander is determined by pressure ratio and power consumption from pump is mainly affected by mass flow rate. However explanation for these factors by previous studies is unsatisfactory, because former studies could not clearly explain the influence of the parameters on the system performance due to lack of experimental cases. Therefore, we conducted experiments under various conditions to understand the effect of evaporating pressure and mass flow rate in this section.

When all the other conditions remain unchanged, we varied evaporating pressure from 3 bar to 5 bar by adjusting hysteresis brake and pump speed; temperature and capacity of heat sources are 70°C and 4 kW, respectively, and temperature of heat sink is 20°C and mass flow rate of secondary fluid at condenser is 250 g/s. The speed of expander is 1500 rpm, mass flow rate of working fluid is about 20 g/s, and pressure at condenser outlet remains about 2 bar. By increasing evaporating pressure, degree of superheat which is the number of degrees by which the temperature of superheated vapor exceeds the temperature of the vapor at its saturation point is decreased; it drops from 18 to 0°C. While the temperature of evaporator outlet remains constant at 70°C, evaporating pressure becomes higher, so degree of superheat decreases. Through the result, we can also acknowledge that there is optimal operating condition for evaporating pressure to achieve maximum power generation.

Since higher evaporating pressure cannot guarantee positive superheat under constant mass flow rate, system power can be decreased over 5 bar. Moreover, pressure ratio elevates along with the evaporating pressure. Since pressure at evaporator outlet gradually increases, pressure ratio of the ORC increases which is shown in Fig. 4.4(a). The variation of evaporating pressure also affects operating condition of expander. Among parameters related with expander, the torque is the most affected factor by pressure ratio. As pressure rises, more torque is required which is shown in Fig. 4.4(b); as pressure grow from 3 to 5 bar, torque also inclined up to 1.2 N.M. In this study, the power generation by expander is obtained using function of measured speed and torque which is shown as below.

$$W_{\exp ander} = \frac{2\pi}{60} \cdot \tau \cdot RPM \tag{4.11}$$

Through the consideration, we can understand the relationship between torque and power generation by expander; under constant expander speed, the amount of power generation is linearly proportional to the torque of expander.

Power generation from expander increases with elevated evaporating pressure; the minimum amount of power generation is about 35 W, and the maximum amount of power generation is about 210 W under this condition. On the other hand, the amount of power consumption also increases depending on pressure increase; it ranges from 55 to 114 W as shown in Fig. 4.5. Therefore, net power generation can be positive or negative, both, according to pressure level. When evaporating pressure is 3 bar, the power consumption by pump

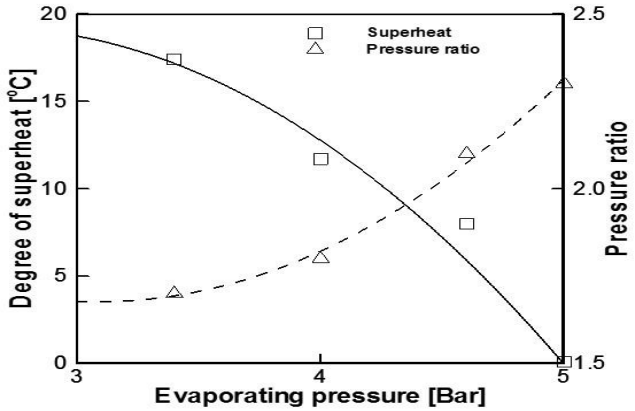

(a) Changes of operating characteristics according to different evaporating pressure

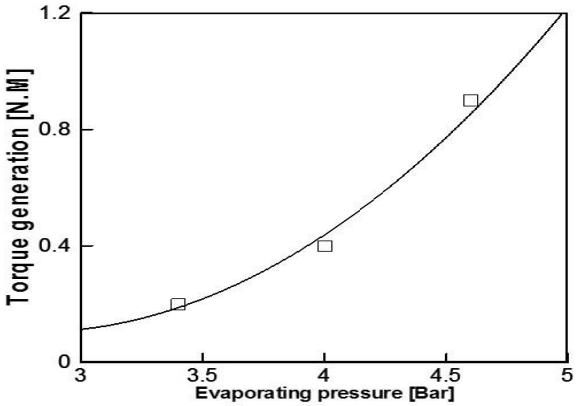

(b) Changes of torque generated from expander according to different evaporating pressure

Fig. 4.4 Changes of operating conditions according to different evaporating pressure.

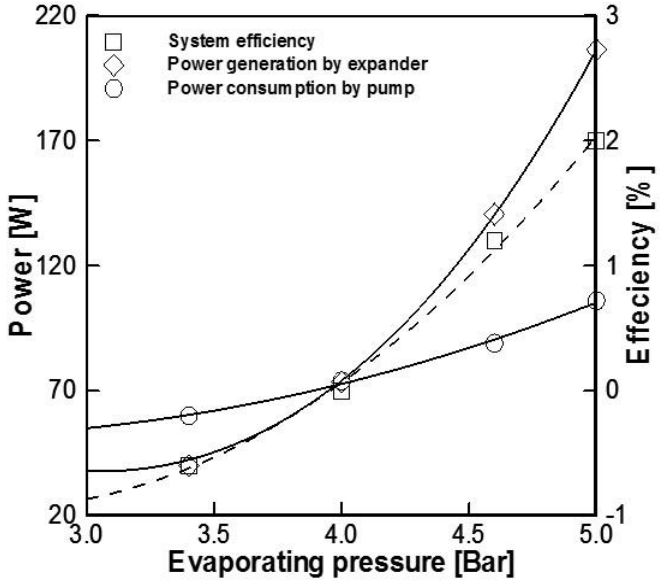

Fig. 4.5 Changes of system output according to different evaporating pressure.

required to supply target pressure and mass flow rate is greater than power generation by expander. Here, system efficiency is obtained by consideration of power consumption by pump, and power generation by expander. System efficiency turns into positive along with pressure increase due to rapid increase of power generation; while the pump power required to raise evaporating pressure is linearly proportional to evaporating pressure, power generation by expander grow rapidly compared to that by pump. If evaporating pressure exceeds 4 bar, system overall efficiency alter to positive, and maximum system power can be acquired at 5 bar. Through this analysis, we can generate positive system efficiency from low-temperature and small-scale heat source; the maximum value of net power is about 100 W, and the corresponding efficiency is 2.8%. Comparing to Carnot efficiency of about 14% under given temperature condition, we can expect to improve efficiency by optimization.

To examine the effect of mass flow rate on the performance of ORC, we varied mass flow rate from 15 to 45 g/s at a given temperature without change of pressure ratio; the conditions of heat source and sink are the same as the former case, and pressure ratio is maintained as 2. First, the amount of absorbed heat increases as mass flow rate rises, because heat capacity of working fluid increases; while mass flow rate increases from 15 to 45 g/s, the amount of heat absorption grow from 3.6 to 5.2 kW. In the case of evaporating pressure, it rises according to increase of mass flow rate, which are shown in Fig. 4.6(a). As mass flow rate increases, efficiency of heat exchanger also increases, and evaporating pressure also increases. These variations have influence on the operating conditions of expander. Increasing mass flow rate without any change

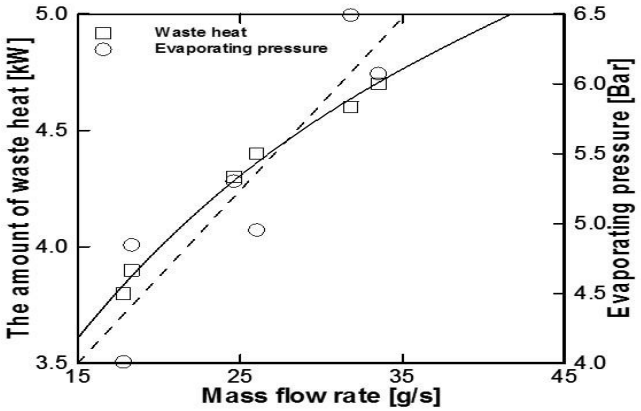

(a) Changes of operating characteristics according to mass flow rate

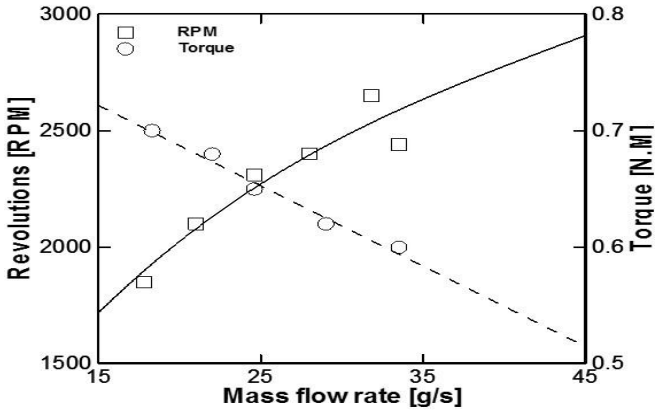

(b) Changes of torque generated from expander according to mass flow rate

Fig. 4.6 Changes of operating conditions according to mass flow rate.

of pressure ratio elevates the expander speed because it can raise velocity of working fluid; speed is raised from 1,700 rpm to 2,800 rpm. On the other hand, torque generation from expander decreases according to the increase of mass flow rate shown in Fig. 4.6(b). To understand this result, we examine the behavior related with expander. At first, loss by over-expansion remains constant; pressure ratio of expander is 3.1, and that of system is 2. However, other losses, such as supply pressure drop, internal leakage, and mechanical loss torque, become greater with increase of mass flow rate, so torque from expander becomes lower; it inversely proportional to increasing mass flow rate.

When increasing mass flow rate, the amount of power generation and consumption increases, as shown in Fig. 4.7. As same as the former analysis, growth of power generation by expander is greater than that by pump by increasing mass flow rate. In addition, the amount of generated power is always larger than that of consumption in these operating ranges, so system efficiency is always positive; the efficiency is up to 1.1%, and the maximum net power is about 108 W under given condition.

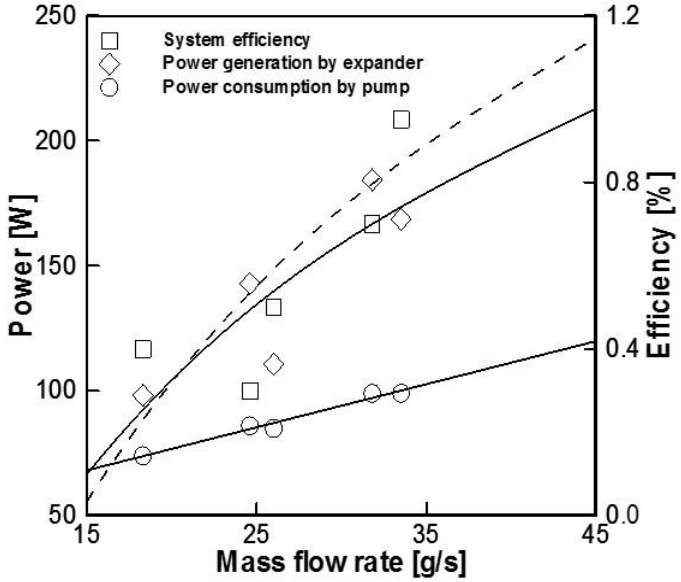

Fig. 4.7 Changes of system output according to different mass flow rate.

4.4 Effect of heat sink temperature

It is necessary to analyze the effect of heat sink temperature on the performance, because we can cover the feasibility of the waste heat recovery system with low grade heat source. Previous studies have tried to know the influences of temperature on desirable operating conditions, however, it is necessary to analyze the influence of temperature of heat sink at various operating conditions. Therefore, we solely change the temperature of heat sink to analyze the effect of external temperatures.

To analyze the effect of temperature of heat sink on the performance, we changed the temperature from 20 to 35°C, and their T-s diagrams are expressed in Fig. 4.8(a). Temperature of heat source is maintained at 70°C, evaporating pressure was about 4.3 bar, and mass flow rate was 20 g/s. The noticeable changes depending on heat sink temperature are temperature variation at condenser and pressure ratio; the former was changed from 28 to 44°C, and the latter was varied from 2.2 to 1.4. These changes reduced system power and its efficiency as shown in Fig. 4.8(b), because enthalpy difference between inlet and outlet of expander becomes small according to the increase of heat sink temperature. Therefore, system power gradually decreases and it becomes negative over about 30°C.

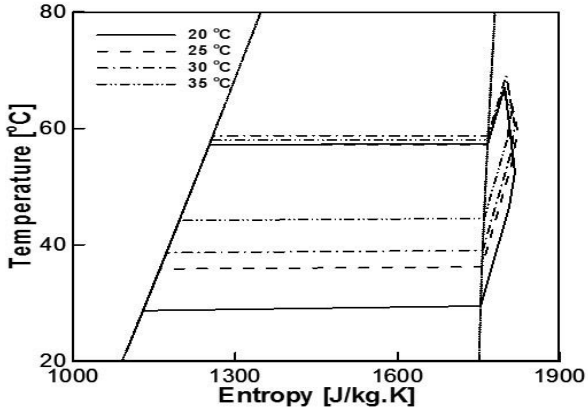

(a) Changes of T-s diagram according to heat sink temperature

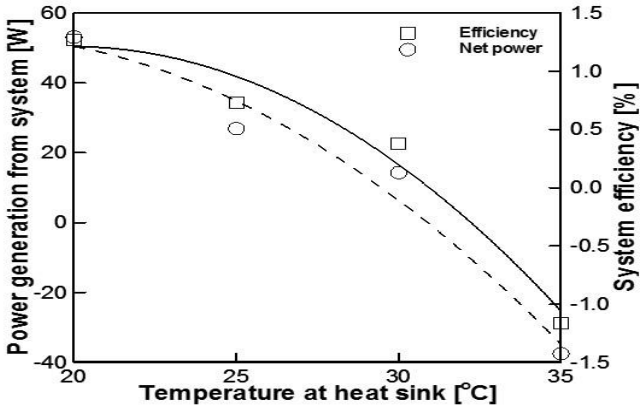

(b) Changes of system output according to temperature at heat sink

Fig. 4.8 Operating characteristics of system according to temperature at heat sink.

4.5 Performance map of organic Rankine cycle operation

Considering the effects of each parameter on the performance, we suggest performance characteristics and relevant operating conditions according to heat source temperature. The optimal operating conditions are expressed in Table 4.1, and T-s diagrams are shown in Fig. 4.9. All parameters should be adjusted depending on heat source temperature to improve system output; evaporating pressure increases from 3.1 to 5.8, mass flow rate increases from 14.1 to 38.5 g/s, and the optimal pressure ratio increases from 1.7 to 2.4 with heat source temperature increase. In addition, degree of superheat is maintained 3°C for a stable operation for every conditions. We can also observe the increase of condensing pressure, since the increase of mass flow rate; higher efficiency of heat exchanger increase of condensing temperature. As temperature of heat source increase, it is more efficient to absorb large amount of heat to improve system efficiency. Therefore, mass flow rate gradually increase to recover larger amount of waste heat. Additionally, larger amount of heat can generate more power through expander, so higher evaporation pressure is desirable for generating system power. Although the amount of absorbed heat is increased, the capacity of heat sink is constant. The heat cannot be released sufficiently at condenser, so condensing temperature gradually rise according to increase of heat source temperature.

Lastly, we developed performance map to show system output and efficiency of low-temperature and small-scale ORC which is shown in Fig. 4.10; temperature increases in the range of 50 to 80°C, and the amount of waste heat is under 10 kW. This map can suggest relationship between net power and

Table 4.1 Optimal operating conditions of ORC according to increase of heat source temperature

Heat source temperature (ºC)	Heat sink temperature (ºC)	Evaporating pressure (bar)	Condensing pressure (bar)	Mass flow rate (g/s)	Power generation (w)	Power consumption (w)	Efficiency (%)
50	20	3.1	1.5	14.1	78.8	59.3	0.78
60	20	3.7	1.7	28.9	207.2	84	1.4
70	20	4.8	1.9	33.5	228.3	103	2.2
80	20	5.8	2.1	38.5	411.3	143	3.6

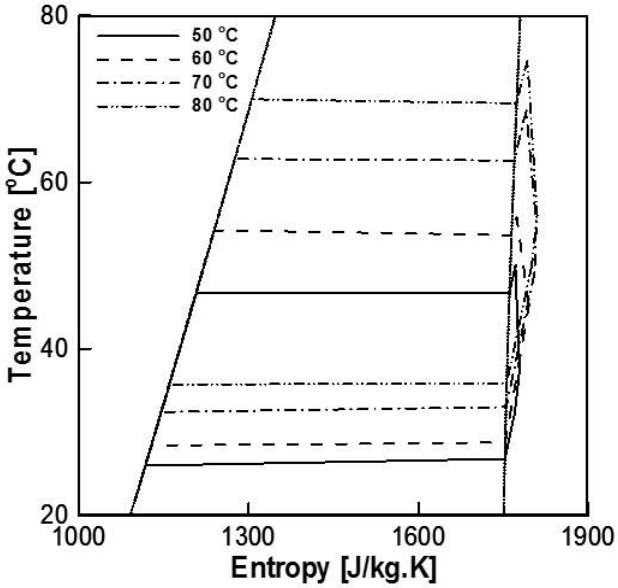

Fig. 4.9 T-s diagram of small-scale organic Rankine cycle system.

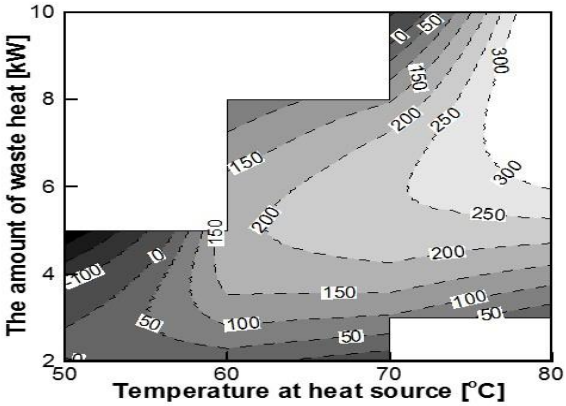

(a) Performance curve for system power

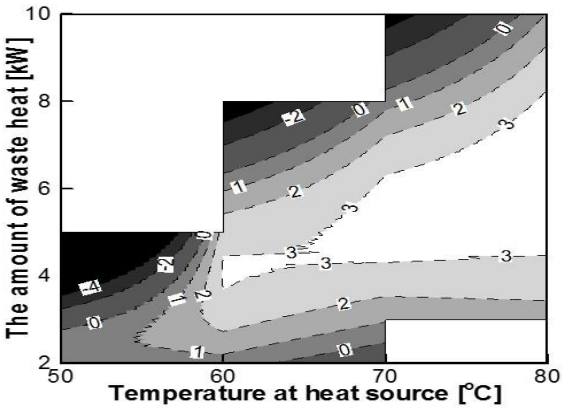

(b) Performance curve for system efficiency

Fig. 4.10 Performance curve for small-scale organic Rankine cycle system.

system efficiency in low-temperature and small-scale range, and we can recognize feasibility of the system in certain condition. System power increases along with higher temperature and higher heat capacity similar to previous predictions; the higher temperature of heat source, the higher power generation from expander [89-90]. However, net power of ORC system become negative when heat source temperature is low and heat capacity is large, e.g., the temperature is 50°C, and the amount of waste heat is 5 kW. In this range, the mass flow rate is greater in order to absorb a large amount of waste heat. However, evaporating pressure is relatively low due to low evaporating temperature. It raises power consumption by pump, but reduces power generation by expander. At a given temperature, net power increases at first but then decreases. Since power generation from expander rapidly increases at early stage, net power also increases. However, the amount of power is consumed more at last stage, so system power becomes reduced. The maximum amount of power is generated at temperature of 80 ^{o}C and heat capacity of 9 kW which is about 370 W. On the other hand, we lose system power at temperature of 50 ^{o}C and over 3 kW which is up to -280 W. White-color region at top left cannot maintain superheat due to relatively large mass flow rate, and its system power is negative. Therefore, that regions are off-design conditions. The other white-color region at bottom right is occurred due to non-operation of expander; mass flow rate of working fluid is too lower to operate expander.

The efficiency variation is similar to that of system power because system efficiency is almost proportional to net power; the highest efficiency is observed at higher temperature region, and the lowest one is found at lower

temperature region. The maximum efficiency is 3.6%, which is far lower than the ideal Carnot cycle efficiency of 17%, this experiment can demonstrate the possibility of waste heat recovery system using low grade heat source.

4.6 Summary

In this study, parametric study for in low-temperature and small-scale organic Rankine cycle (ORC) is conducted to understand the effect of parameters on the performance and to develop performance map for the system. Firstly, we examined the effect of evaporating pressure and mass flow rate on the performance. As increase of evaporating pressure from 3 bar to 5 bar, expander can generate more power of 80 W, so net power and system efficiency also increase; through the efficiency is negative at 3 bar, it goes to 2 % at given condition. Mass flow rate has positive effect on the system performance. Even though pump power consumption increases up to 100 W, the amount of power generated from expander is larger, so net power of system become increased. The difference of power generation and consumption become larger according to mass flow rate, and the system can generate over 120 W at the condition. Analyzing the effect of heat sink temperature, the system power decreases according to increase temperature of heat sink. When temperature of heat sink is over 30 ^{o}C, net power of the system become negative. By increasing heat sink temperature, pressure ratio become reduced, so net power and efficiency also decrease. Through this result, we can recognize possible range of temperature for heat sink.

In the end, we developed performance map of ORC for low-temperature source in small-scale range to show net power and relevant efficiency. As

temperature of heat source increases, net power and efficiency go higher; the system can generate over 300 W and 3 % at temperature of heat source of 80 ^{o}C. However, the performance of ORC does not simply increase according to capacity of waste heat. When temperature of heat source is 70 ^{o}C, net power increase to 250 W, at first, but then decrease. The reason for decrease of net power is immoderate growth of mass flow rate which is occurred by large absorption of waste heat. Therefore, the amount of power generation by expander is lager when the amount of waste heat is range from 2 kW to 6 kW, however, more power consumed by pump over 6 kW. Through the results, we can know the feasibility and optimized condition for ORC for low-temperature source in small-scale range.

Chapter 5. Optimization for cogeneration system

5.1 Introduction

Optimization for cogeneration system which is consisted of PEM fuel cell coupled with ORC is conducted in this chapter. By conducting genetic algorithm, this study suggest optimized operating conditions for pressure of each system depending on current density. At first, we examine the effect of pressure on the system. By changing pressure of PEM and ORC, this study shows the variation of performance of each system. Analysis for power generation and consumption in the system supports the behavior of the system. Next, performance of the system depending on current density was invested to understand effect of pressure. Variation of power from the system can explain the results of the system. Lastly, optimized operating condition is suggested using genetic algorithm. Optimized operating pressure for PEM and ORC is suggested at each current density.

5.2 Methodology

Numerical analysis

The cogeneration system is developed using system model for PEM fuel cell and ORC. We prepare ORC model instead of fan model in the TMS. The schematic diagram of hybrid system is presented in Fig. 5.1. In the system, ORC replace thermal management system in the fuel cell, and other components consisting PEM fuel cell system remain unchanged. The purpose of ORC is to recover waste heat from fuel cell delivered by coolant flowing the stack. The

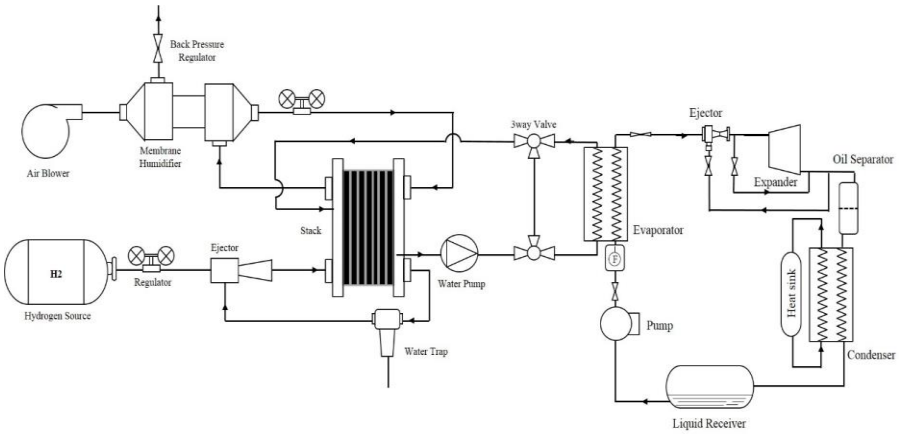

Fig. 5.1 Schematic diagram of cogeneration system which is consisted of PEM fuel cell coupled with ORC system.

logic for the system is developed by matching the operating temperature at each step. The flow chart of hybrid system is presented in Fig. 5.2. The early stage of the model is similar to PEM fuel cell, but the number of inputs is added to consider the variables for ORC. Firstly, the model calculates the parts of PEM fuel cell, and then, calculates that of ORC. By obtaining the conditions for coolant flowing through the coolant channel in the stack which is affected by operating condition of ORC, we can obtain the operating temperature of fuel cell. By comparing the operating temperatures at each steps, we can acquire the accurate operating state of cogeneration system.

Optimization

The optimization is conducted using genetic algorithm which is process using natural selection. This process uses techniques associated with natural evolution; inheritance, mutation, selection, and crossover. To understand performance of cogeneration system, we firstly conducted parametric study for operating pressure of PEM fuel cell, inlet pressure at expander, and current density. Stoichiometric number and operating temperature remain constant; 2 for stoichiometric number at cathode, 1.5 for that at anode, and 80°C for operating temperature. Then, we conducted optimization to find optimal operating condition for cogeneration system. Genetic algorithm (GA) is utilized to find optimal operating condition which is originated from natural evolution. The optimization is applied by using optimtool in MATLAB, and the flow chart for this method is expressed in Fig. 5.3.

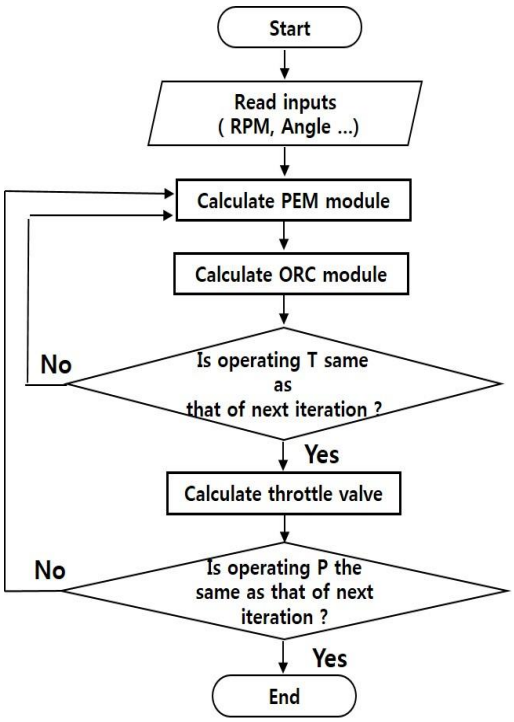

Fig. 5.2 Flow chart for the cogeneration system.

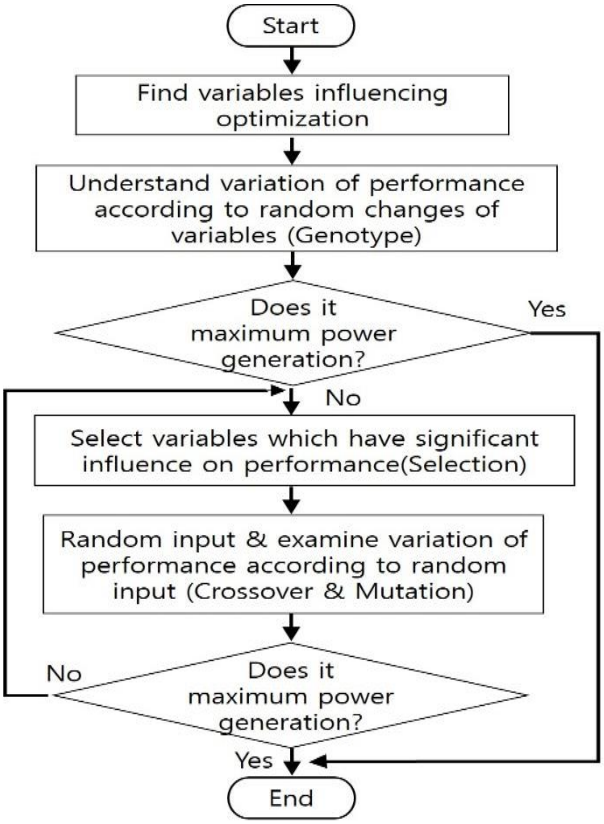

Fig. 5.3 Flow chart for genetic algorithm.

5.3 Effect of operating pressure on system performance

In this chapter, effect of pressure on cogeneration system is examined; the operating pressure of fuel cell is ranged from 1.2 to 1.8, and that of ORC is ranged from 2.5 to 3.5. In Fig. 5.4, Variation of power generation from PEM and ORC is presented. The power generation of PEM is increased according to pressure; higher pressure helps to raise concentration near the membrane, therefore, the more power is produced. However, the amount of power generation become reduced according to pressure. Larger power consumption form blower is occurred compared to power generation from stack, so system power become reduced. It means that there is optimal operating pressure level for system power generation. Inlet pressure at expander cannot affect the performance of fuel cell. On the other hand, the amount of power generation from ORC is reduced according to operating pressure of fuel cell. Reduced waste heat from fuel cell causes decrease of incoming heat of ORC, so power generation from ORC is decreased. System efficiency of system is similar to variation of power generation which is shown in Fig. 5.5. Efficiency of cogeneration system increase with increased of pressure of ORC and PEM. The amount of performance increase by change of pressure is about 3 %. The first changes occurred from applying ORC is observed from power generation. ORC can generate more power using waste heat from fuel cell, so the power generation from cogeneration system is raised. In addition, applying ORC have influence on operating condition of TMS in fuel cell system; due to ORC, temperature of TMS inlet of fuel cell system decrease, so power consumption

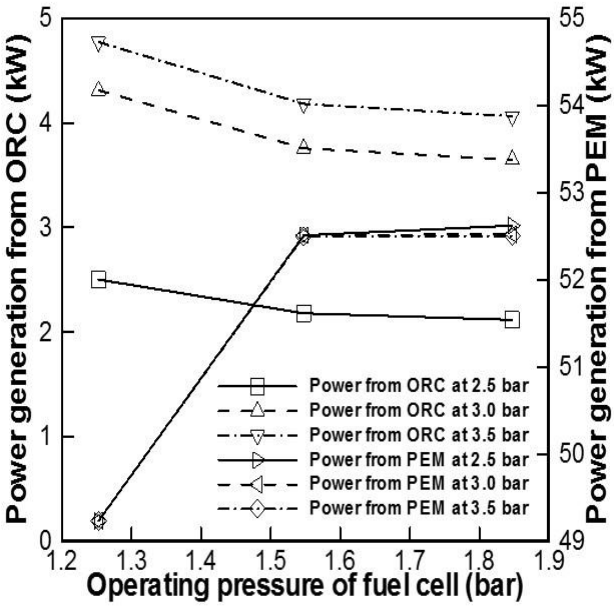

Fig. 5.4 Variation of power generation according to pressure.

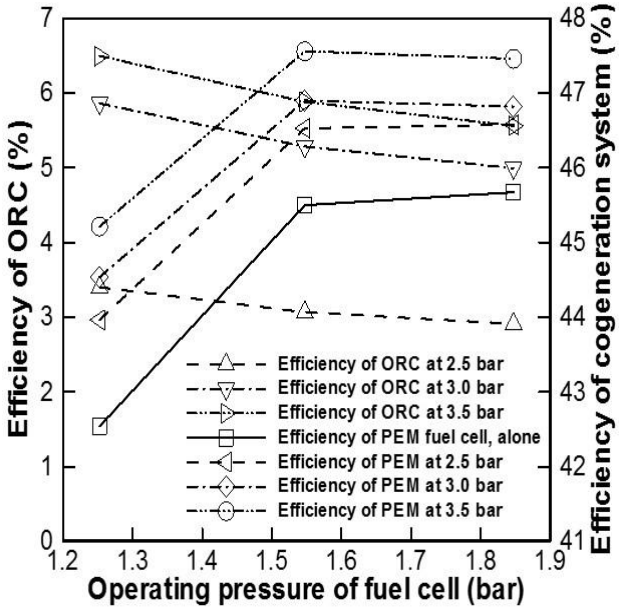

Fig. 5.5 Variation of system efficiency according to pressure.

in TMS reduced. Above changes are shown in Fig, 5.6. This changes helps to raise system efficiency of cogeneration; although the amount increased power from the cogeneration system is decreased with pressure increased, the more system power generated with increased of pressure of PEM and ORC.

5.4 Effect of current density on system performance

The effect of current density on system performance is important factor for cogeneration system, because current density is directly connected with the amount of power generation of fuel cell and it also decide the amount of waste heat that can utilized by ORC. Therefore, we have to know the operating condition at different load conditions. We examined the effect of current density at 0.6 A/cm^2, 1.0 A/cm^2, and 1.4 A/cm^2 to know the system conditions at light, intermediate, and heavy load conditions.

The variation of system of PEM and ORC is presented in Fig. 5.7; power generations in both system are increased according to current density. As pressure of PEM fuel cell increase, power from fuel cell system is also increase, however, that from ORC is reduced. Increase of power generated from fuel cell decreases the amount of waste heat from stack, and it means decrease of available energy for ORC. Therefore, the amount of power from ORC is decreased according to operating pressure of fuel cell. The variation of efficiency of cogeneration system is expressed in Fig. 5.8; Trend of efficiency of ORC is similar to variation of power of ORC, however, that of fuel cell is opposite. It is due to relationship between power generation from stack, and power consumption from blower. As current density grow, the amount of power

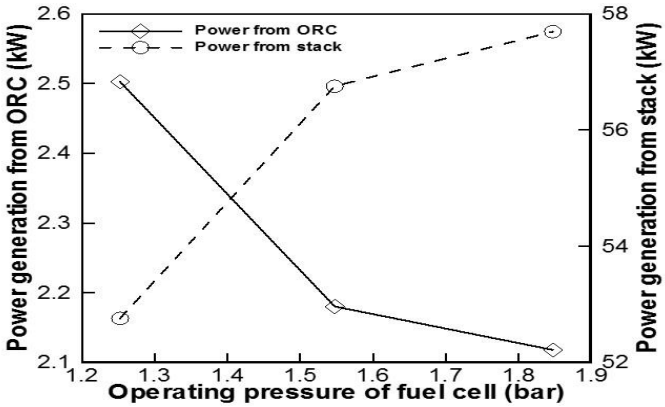

(a) Power generation from PEM and ORC

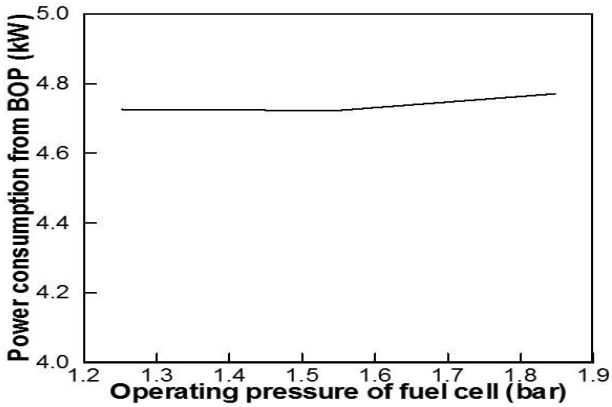

(b) Power consumption from auxiliaries

Fig. 5.6 Variation of power in the cogeneration system according to pressure.

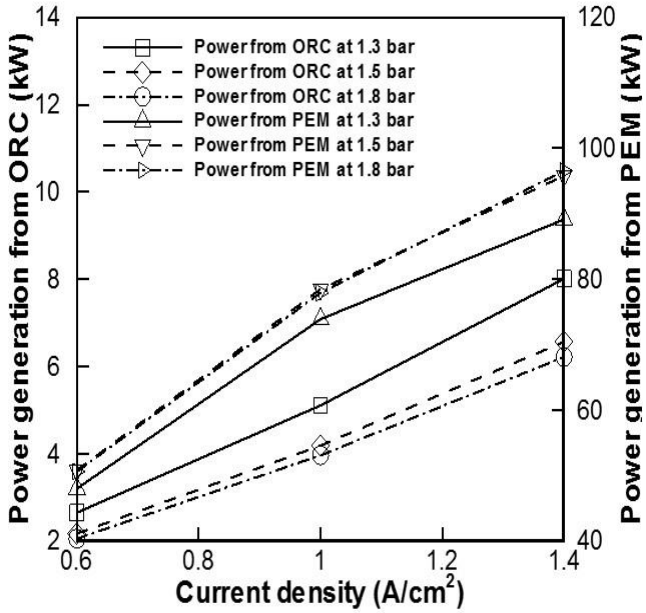

Fig. 5.7 Variation of power generation according to current density.

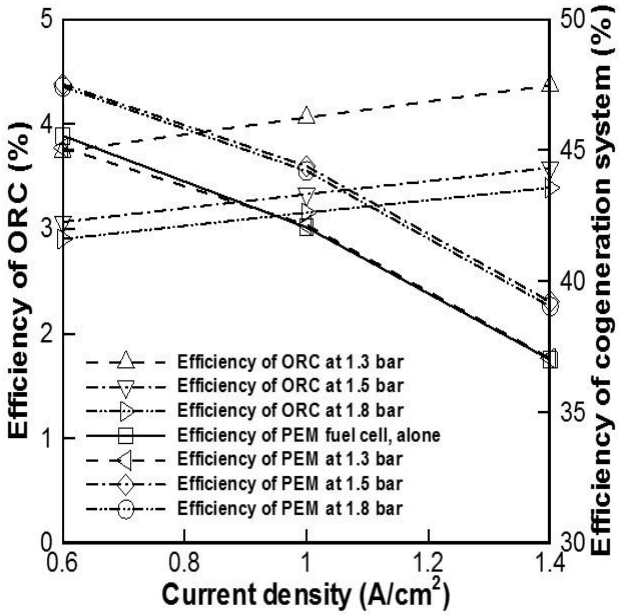

Fig. 5.8 Variation of power generation according to pressure.

generation from stack increase, however, that of blower is increased more. Therefore, higher pressure cannot help to raise system power and reduce system efficiency.

If the ORC is applied, system efficiency can be increased in all operating region. The efficiency of fuel cell system alone is about 45% at light load, and 37% at heavy load condition, however, the efficiency of cogeneration system is higher than fuel cell system of about 2%.

Power generation from stack is gradually increased according to current density; stack can generate about 60 kW, and 105 kW at 0.6 A/cm^2, and 1.4 A/cm^2. For ORC, power is increased from 2 kW to 8 kW at operating range. As current density is raised, larger amount of waste heat increase the amount of power generation from ORC. However, power generation of blower and fan also increase according to current density as shown in Fig. 5.9. This variation of power consumption from components affects the performance of system power.

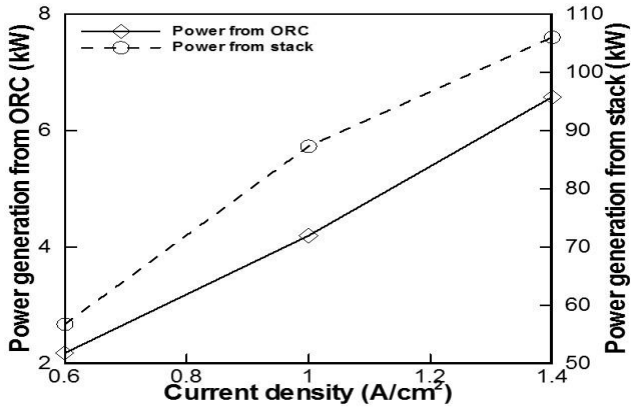

(a) Power generation from PEM and ORC

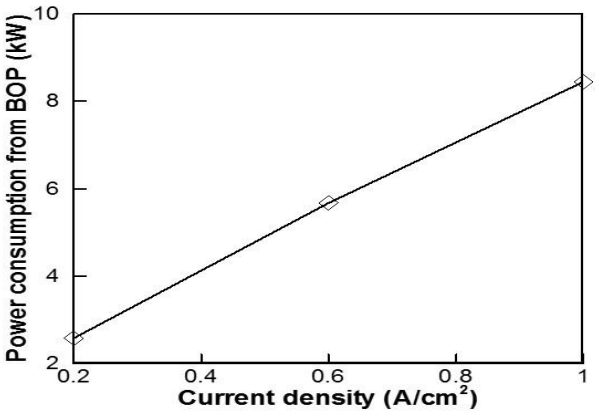

(b) Power consumption from auxiliaries

Fig. 5.9 Variation of power in the cogeneration system according to current density.

5.5 Optimization for cogeneration system

The optimal operating condition is examined by changing pressure of fuel cell and ORC at different current density. To eliminate disturbance occurred from other parameters, stoichiometric number and operating temperature remain constant, 2 for cathode, 1.5 for anode, and 80 ^{o}C for operating temperature.

The optimal operating condition according to current density is listed in table 5.1. Optimal pressure of PEM fuel cell is higher at light load condition, then decrease until 1.0 A/cm^2, and increase again. The higher pressure is calculated from the relationship between higher power generation from stack, and lower power consumption from blower at light load condition. At lower current density region, power consumption of blower is low, so it does not spend large power consumption. However, optimal pressure become decrease due to larger power consumption of blower until intermediate load condition. Recommended pressure goes up again at heavy load condition because added power from ORC can offset the disadvantage of higher power consumption from blower. On the other hand, operating pressure for ORC remain higher, about 3.6; optimized pressure become decreased according to current density, because the amount of waste heat from fuel cell affect the efficiency of ORC. Therefore, optimal pressure at expander inlet for ORC is decreased until 3.4 bar. The variation of system efficiency and power generation is shown in Fig. 5.10. Maximum power generation is about 120 kW, and lowest efficiency is 42%, and highest efficiency is about 57%.

Table 5.1 Operating condition for cogeneration system

Current density	Stoichiometric number (Ca/An)	Pressure of PEM	Pressure of ORC	Temperature of stack
0.2	(2/1.5)	1.78	3.6	80
0.6	(2/1.5)	1.63	3.53	80
1.0	(2/1.5)	1.54	3.48	80
1.4	(2/1.5)	1.68	3.44	80

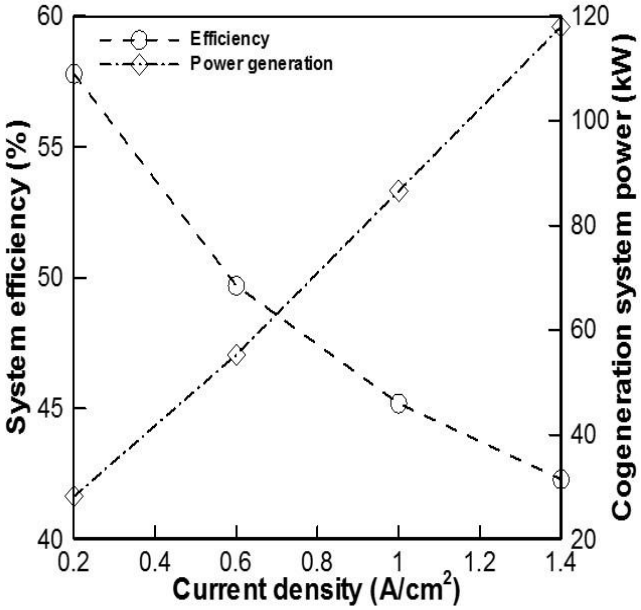

Fig. 5.10 Optimal power generation of cogeneration system at different current density.

5.6 Summary

In this chapter, the optimal operating condition for cogeneration which is consisted of PEM fuel cell coupled with ORC is investigated. As pressure of fuel cell increase, power generation of PEM fuel cell is increase from 49 kW to 53 kW, however, pressure at inlet of expander cannot affect the performance of fuel cell. Performance of ORC is decreased with increased of pressure of fuel cell, because the amount of waste heat has influence on the amount of power generation from ORC. The effect of pressure of fuel cell cannot greatly effect on the performance of ORC, however, the effect of pressure at expander inlet is significant. The change of performance caused by pressure or PEM is 0.2 kW, but that by inlet pressure of expander is 2 kW. Power generation of cogeneration is proportional to current density; power from fuel cell increase from 60 kW to 90 kW, and that from ORC increase from 3 kW to 7 kW. Power generation is increased according to current density, however, that of auxiliaries are also increased. Power consumption from BOP is increased from 5 kW to 8 kW, and this increase of power consumption reduces the system efficiency, so efficiency of cogeneration system is decreased from 46% to 37%. The efficiency of cogeneration system is 2% larger than fuel cell system alone. Therefore, we can convince the advantage of cogeneration system.

Chapter 6. Concluding remarks

In this study, performance improvement of cogeneration system which is consisted of polymer electrolyte membrane (PEM) fuel cell coupled with organic Rankine cycle (ORC) according to pressure. Here, ORC is applied to recover waste heat from PEM fuel cell whose temperature is below 80 ^{o}C. ORC system is placed in the thermal management system (TMS) to recover waste heat and reduce thermal load on the radiator in TMS. Working fluid of fuel cell flowing the coolant channel in the stack enters the evaporator in the ORC to deliver waste heat from stack, and expander generates power. To achieve optimal performance of the system, we should understand the operating characteristics of the system, and examine the optimal condition for the system.

The first step, before we examine the operating characteristics of cogeneration system, is to conduct parametric study for operating pressure, however, the explanation for effect of pressure on the mass transport through the membrane is insufficient. To understand the mechanism of mass transport through the Nafion® 117, we developed novel equation considering water sorption, diffusion, convection, and capillary pressure characteristics occurred in the membrane, and we conducted experiment to support this model. The model shown error about 2 % for dry outlet, and 8 % for wet outlet. Therefore, we can convince the model to apply for investing membrane humidifier and stack consisting PEM fuel cell system. Through the model, we can know that liquid water is dominant factor influencing water transport through the

membrane.

Using above equation, this study develop fuel cell system model which includes stack, air providing system (APS), fuel providing system (FPS), and thermal management system (TMS). The model is validated using data of actual car supported by Hyundai Motor Corporation. All models are developed using theoretical basis, but relationship of power consumption of some devices is expressed using empirical form. All models shows error under 7%, so we can convince the system model. In the system, operating pressure is controlled using RPM of blower and angle of back pressure control valve (BCV). As pressure increase, stoichiometric number, pressure, and power consumption of blower increase, but relative humidity decrease due to raising temperature at blower outlet. In the end, we develop performance curve for fuel cell car at different velocities and load conditions. Higher performance is observed at higher RPM and blower angle of BCV, however, system efficiency is low at that region; maximum fuel cell power is reached at 80 kW, but the efficiency at that point is under 50%. Maximum power is found at higher velocity and larger current density region.

In addition, a study for ORC is conducted to recover low grade waste heat from fuel cell as well. To demonstrate the performance of ORC at given temperature, we prepared experimental setup, and conducted parametric study by changing mass flow rate, pressure of expander inlet, and temperature of heat sink and source. Moreover, this study examined the types of expander that can maximize performance of ORC for low grade heat. Three types of expander, rotary vane, rotary engine, and scroll, are analyzed numerical and experimental

method, both. Among these types, scroll type expander can generate the largest power at given condition; the maximum powers that can generate from expander are 70 W for rotary vane type expander, xx W for rotary engine type expander, and 280 W for scroll type expander. Additionally, evaporating pressure and mass flow rate have positive influence on the performance, so the higher pressure and mass flow rate, the more power generate under laboratory condition.

Lastly, optimization for cogeneration system is conducted to find optimal operating condition. Higher operating pressure for fuel cell is beneficial for power generation from fuel cell, however, it has bad effect on power generation from ORC. This lower performance can be offset by raising pressure at expander inlet. At 0.6 A/cm2, the power generation from fuel cell is reached to 53 kW, and that of ORC is about 4 kW. The variation of system efficiency is similar to that of power generation except effect of pressure at expander inlet on system efficiency. In addition, power generation is proportional to current density, for both system. However, slope of efficiency of each system is different, because power consumption from BOP at fuel cell is dramatically increased, so system efficiency is decreased. For cogeneration system, maximum power is about 90 kW, and the efficiency is 45% at that condition. Through this results, we can convince advantage of cogeneration system; this system generates more power of 8 kW, and higher efficiency of 2% than the fuel cell system, alone.

References

1. http://www.thinktheearth.net/thinkdaily/report/2010/08/rpt-3.html#page-2.
2. Quoilin S., Broek M. V., Declaye S., Dewallef P., Lemort V., Renewable and sustainable Energy reviews 2013; 22:168-186.
3. Ziogou C., Voutetakis S., Papadopoulou S., Georfiadis M. M., Computers and Chemical Eng., 35 (2011) 1886-1900.
4. Jeon D. H., Greenway S., Shimpalee S., Zee J. W., Int. J. Hydrogen Energy, 33 (2008) 1052-1066.
5. Corbo P., Migliardini F., Veneri O., Int. J. Hydrogen Energy, 32 (2007) 4340-4349.
6. Bao C., Ouyang M., Yi B., Int. J. Hydrogen Energy, 31 (2006) 1879-1896.
7. Uno M., Shimada T., Tanaka K., J. Power Sources, 196 (2011) 2558-2566.
8. Badami M., Mura M., Energy Conversion and Management, 51 (2010) 553-560.
9. Wang Y., Wang C., J. Power Sources, 147-(2005) 148-161.
10. Dutta S., Shimpalee S., Zee J. W., Int. J. Heat and Mass Transfer, 44 (2001) 2029-2042.
11. Ying W., Sohn Y., Lee W., Ke J., Kim C., J. Power Sources, 145 (2005) 563-571.
12. Tchanche B. F., Papadakis G., Lambrinos G., Frangoudakis A., Applied Thermal Eng. 2009; 29:2468-2476.

13. Wang E. H., Zhang H. G., Fan B. Y., Ouyang M. G., Zhao Y., Mu Q. H., Energy 2011; 36:3406-3418.
14. Wang Z. Q., Zhou N. J., Guo J., Wang X. Y., Energy 2012; 40:107-115.
15. Wang J., Yan Z., Wang M., Ma S., Dai Y., Energy 2013; 49:356-365.
16. Zhang S., Wang H., Guo T., Applied Energy 2011; 88:2740-2754.
17. Quoilin S., Lemort V., Lebrun J., Applied Energy 2010; 87:1260-1268.
18. Lemort V., Quoilin S., Cuevas C., Lebrun J., Applied Therm. Eng. 2009; 29:3094-3102.
19. BCS Inc, Waste heat recovery: technologies and opportunities in U.S. industry, US Dept. of Energy (DOE) (2008).
20. Zhao P., Wang J., Gao L., Dai Y., Int. J. Hydrogen 2012; 37:3382-3391.
21. Gierke T.D., Munn G.E., Wilson F.C., J. Polymer. Sci. 19 (1981) 1687–1704.
22. Feng X., Huang R.Y.M., J. Memb. Sci., 118(1) (1996) 127-131.
23. Pivovar B.S., Wang Y., Cussler E.L., J. Memb. Sci., 154(2) (1999) 155-162.
24. Springer T.E., Zawodzinski T.A., Gottesfeld S., J. Electrochem. Soc. 138 (8) (1991) 2334–2342.
25. Zawodzinski T.A., Springer T.E., Davey J., Jestel R., Lopez C., Valerio J., Gottesfeld S., J. Electrochem. Soc. 140 (7) (1993) 1981–1985.
26. Zawodzinski T.A., Derouin C., Radzinski S., Sherman R.J., Smith V.T., Springer T.E., Gottesfeld S., J. Electrochem. Soc. 140 (4) (1993) 1041–1047.
27. Kreuer K.D., J. Membr. Sci. 185 (2001) 29–39.

28. Hinatsu J.T., Mizuhata M., Takenaka H., J. Electrochem. Soc. 141 (6) (1994) 1493–1498.
29. Choi P., Datta R., J. Electrochem. Soc. 150 (12) (2003) 601–607.
30. Poling B.E., Prausnitz J.M., O'Connell J.P., The Properties of Gases and Liquids, McGraw-Hill, New York, 2001.
31. Welty J., Wicks C.E., Wilson R.E., Fundamentals of Momentum, Heat, and Mass Transfer, John Wiley & Sons, New York, 1984.
32. Gregory J.K., Clary D.C., Liu K., Brown M.G., Saykally R.J., Science 275 (1997) 814–817.
33. Neuman S.P., Acta Mechanica, 25 (1977) 153–170.
34. Harding C., Chapter 24: Fundamentals of Mass Transfer. Diffusivity of Water in Air at 20 Degrees Celsius and 1 Atmosphere, chrisbharding.wordpress.com [online], 2012.
35. Cwirko E.H., Carbonell R.G., J. Memb. Sci., 67 (1992) 227-247.
36. Vishnyakov A., Neimark A.V., J. Phys. Chem., 104(2000) 4471-4478.
37. Cussler E. L., Diffusion: Mass Transfer in Fluid Systems, Cambridge University Press, New York, 1997.
38. Philip J.R., Annu. Rev. Fluid Mech., 2 (1970) 177–204.
39. Duan Q., Wang H., Benziger J., J. Membr. Sci.392-393 (2012) 88-94.
40. Kim D., Seo J., Kim S., Lee M., Nam K., Song H., Kim M., Int. J. Hydrog. Energy 39 (35) (2014) 20139–20150.
41. Deroouin C., Pafford J., Radzinski S., Springer T., Gottesfeld S., The electrochem. Soc. Extended abstract, 89-1 (1989).
42. Duan Q., Wang H., Benziger J., J. Membr. Sci.392-393 (2012) 88-94.

43. Yan X., He G., Wu X., Benziger J., J. Membr. Sci. 429 (2013) 13-22.

44. Eirkerling M., Kharkats Y.I., Kornyshev A.A., Volfkovich Y.M., J. Electrochem. Soc. 145 (8) (1998) 2684–2699.

45. Wu S., Brzozowski K.J., J. colloid and interface Sci., 37(4) (1971) 686-690.

46. Fowkes F.M., Ind. Eng. Chem., **56(**40) (1964) 40-52.

47. Wu S., Polymer Interface and Adhesion, Marcel Dekker, New York, NY, 1982, p. 142-146.

48. Guo D., Fu S., Tan W., Dai Z., J. Mater. Chem., 20 (2010) 10159-10168.

49. Battino R., Rettich T.R., Tominaga T., J. Phys. Chem, 13(2) (1984) 563-600.

50. Park S., Cho E., Oh I., Korean J. Chem. 22 (6) (2005) 577–881.

51. Pushpa K.K., Nandan D., Iyer R.M., J. Chem. Soc. 84 (6) (1988) 2047–2056.

52. Yang C., Srinivasan S., Bocarsly A.B., Tulyani S., Benziger J.B., J. Membr. Sci.237 (1-2) (2004) 145-161.

53. Huizing R., Foxler M., Merida W., Dean J., J. Power Sources 180 (1) (2008) 265–275.

54. Park S., Choe S., Choi S., Int. J. Hydrog. Energy 33 (9) (2008) 2273–2282.

55. Kang S., Min K., Yu S., Int. J. Hydrog. Energy 35 (4) (2010) 1727–1741.

56. Park S., Jung D., Int. J. Hydrog. Energy 38 (17) (2013) 7114–7125.

57. Goff J.A., Gratch S., Transact. Am. Soc. Heat. Vent. Eng. 52 (1946) 95–122.

58. Navessin T., Holdcroft S., Wang Q., Song D., Liu S., Eikerling M., Horsfall

J., Lovell K.V., J. Electroanalytical Chemistry 567 (1) (2004) 111-122.

59. Ye D., Gauthier E., Benziger J. B., Pan M., J. Power Sources, 256 (15) (2014) 449-456.
60. Real A. J., Arce A., Bordons C.. J Power Sources 2007; 173:310-324.
61. Pukrushpan JT, Modeling and control of fuel cell systems and fuel processors, Ph.D. Dissertation, Department of Mechanical Engineering the University of Michigan, Ann Arbor, Michigan, 2003.
62. Marcos V., Moreira, Gisele E., da Siva, Renewable energy 2009; 34:1734-1741.
63. Moraal P., Kolmanovsky I., Soc. Automotive Eng., (1999) 1-15.
64. Cabello R., Navarro J., Torrella E., Applied Therm. Eng., 25 (2005) 1740-1752.
65. Navarro E., Granryd E., Urchueguia J. F., Corberan J. M., Int. J. Refrigeration, 30 (2007) 1254-1265.
66. Chen D., Peng H., American Soc. Mech. Eng., 127 (2005) 424-432.
67. Cave P., Merida W., J. Power sources, 175 (2008) 408-418.
68. Park S., Oh I., J. Power sources, 188 (2009) 498-501.
69. Huang B. J., Chang J. M., Wang C. P., Petrenko V. A., Int. J. Refrigeration, 22 (1999) 354-364.
70. Hemidi A., Henry F., Leclaire S., Seynhaeve J., Bartosiewicz Y., Applied Therm. Eng., 29 (2009) 1523-1531.
71. Hemidi A., Henry F., Leclaire S., Seynhaeve J., Bartosiewicz Y., Applied Therm. Eng., 29 (2009) 2990-2998.
72. Yu S., Jung D., Renewable Energy, 35 (2010) 2525-2532.

73. Wen C., Lin Y., Lu C., Luo T. , Int. J. Hydrogen Energy, 36 (2011) 6082-6089.
74. Wang C., Chi K., Chang C., Int. J. Heat and mass transfer, 43 (2000) 2693-2700.
75. White F. M., “Fluid Mechanics”, 5th edition, Mcgrawhill Korea (2009).
76. Li X., Cao G., Zhu X., Energy conversion and management, 47 (2006) 1032-1050.
77. Li C., Zhu X., Cao G., Sui S., Hu M., J. Power sources, 175 (2008) 303-316.
78. Zhu Y., Cai W., Li Y., Wen C., J. Power Sources, 185 (2008) 1122-1130.
79. Marsano F., Magistri L., Massardo A. F., J. Power Sources, 129 (2004) 216-228.
80. Barbir F., Gorgun H., J. Applied Electrochem., 37 (2007) 359-365.
81. Badami M., Mura M., Energy Conversion and Management, 55 (2012) 20-25.
82. Kim D. K.. Koh J. S., Kim M. S., Song H. H., Int. J. Hydrogen 2015; 40:12370-12381.
83. Quoilin S., Doctor thesis, Dept. applied science, Liege University, Belgium 2011.
84. Hsieh Y. Y., Lin T. F., Int. J. Heat and Mass transfer 2002; 45:1033-1044.
85. Kuo W. S., Lie Y. M., Hsieh Y. Y., Lin T. F., Int. J. Heat and Mass transfer 2005; 48:5205-5220.
86. Lemort V., Quoilin S., Cuevas C., Lebrun J., Applied Therm. Eng. 2009; 29:3094-3102.

87. Ro O. H., 2009. Compressible fluid flow, first ed. Parkyoungsa, Seoul.
88. Incropera F.P., DeWitt D.P., Fundamentals of Heat and Mass Transfer, John Wiley & Sons, 2002.
89. Wang J., Yan Z., Wang M., Ma S., Dai Y., Energy 2013; 49:356-365..
90. Srinivasan K. K., Mago P. J., Krishnan S. R., Energy 2010; 35:2387-2399.

국 문 초 록

효율이 높고, 친환경적이며 작동 온도가 낮은 고분자 전해질막 연료전지에 대한 관심이 증가하고 있다. 이에 따라 연료전지 성능 향상에 관한 연구도 활발하게 진행되고 있다. 본 연구에서는 가변압 시스템이 적용된 고분자 전해질막 연료전지 시스템의 성능에 대한 연구와 연료전지에서 발생되는 미활용 열을 이용하기 위한 폐열 회수 시스템의 제안 및 효율 향상에 관한 연구를 수행하였다.

먼저 압력에 따른 연료전지의 영향을 정확하게 분석하기 위해, 압력이 고분자막을 통한 물질 이동에 미치는 영향에 대해 알아보았다. 고분자 막을 통한 물의 이동을 크게 수증기와 물로 구분한 뒤 확산, 대류, 모세관으로 구동력을 나누어 넘어가는 양을 계산하였다. 습도가 높고, 온도가 높으며, 압력이 낮은 경우 더욱 많은 양의 물이 넘어가는 것을 확인할 수 있었다. 해당 식을 통하여 스택에 대한 모델링을 수행한 경우, 물이 많이 발생하는 조건에서도 비교적 정확하게 성능을 예측할 수 있었다. 이를 이용하여, 가변압 연료전지 시스템에 대한 해석적 연구를 수행하였다. 해당 시스템에서 압력은 블로어의 속도와 배압밸브의 각도로 제어되는데, 이들 관계에 의해서 당량비와 스택 입구 습도도 영향을 받는다. 압력이 높을수록 시스템의 성능이 높아지지만, 입구 측 습도의 저하와 증가하는 소모동력 때문에, 1.6 bar 정도에서 최고의 출력을 낼 수 있다. 속도에 따른 연료전지 시스템의 성능 맵을 분석하면,

전구간에서 고출력은 블로어의 속도가 빠르고, 배압밸브의 각도가 작은 곳에서 얻을 수 있고, 높은 효율은 속도가 느리고, 각도가 큰 곳에서 얻을 수 있다.

연료전지의 저온 폐열을 회수하기 위한 유기냉매 랭킨 사이클의 경우, 냉매는 R245fa 가 사용되었다. 시스템은 80 도에서 최대 4% 정도의 효율을 낼 수 있었으며, 이 때 생성 전력은 270 W 정도이다. 주어진 온도에서 효율을 높이기 위해 다양한 타입의 팽창기에 대한 연구도 수행하였다. 로터리베인, 로터리 엔진, 스크롤 타입의 팽창기에 대해 연구를 수행하였는데, 로터리 베인의 경우, 낮은 엔탈피차이에서도 작동이 가능하다는 장점이 있었다. 스크롤 팽창기의 경우, 가장 큰 출력을 낼 수 있었고, 로터리 엔진 타입의 경우 앞선 두 팽창기의 중간 정도의 특징을 지녔다. 마지막으로, 연료전지 시스템과 유기냉매 랭킨사이클을 결합한 복합 시스템을 구성하여 작동조건의 최적화를 통해 복합 시스템의 효율을 높이기 위한 연구를 수행하였다. 전류밀도가 증가함에 따라서 연료전지 시스템의 작동 압력은 낮아지고, 유기냉매 랭킨 사이클의 압력은 높게 유지하는 것이 복합 시스템의 성능 향상을 위해 유리하다는 것을 확인할 수 있었다. 향후 저온 폐열을 활용할 수 있는 복합 시스템에 대한 연구가 더욱 진전된다면, 에너지를 더욱 효율적으로 사용할 수 있을 뿐 아니라, 환경적으로도 도움을 주어, 지속 가능한 개발을 가능하게 할 수 있다.

주요어: 고분자 전해질막 연료전지, 유기냉매 랭킨사이클, 복합시스템,
나피온(Nafion)117, 팽창기
학 번: 2011-20687